ABSTRACT

Title of dissertation: THE INTERACTION OF SPRINKLER SPRAYS AND FIRE PLUMES

Eric D. Link, Doctor of Philosophy, 2017

Dissertation directed by: Associate Professor André Marshall, Department of Mechanical Engineering

The critical factor for successful suppression using fire sprinklers is the delivery of water to burning surfaces. Water delivery is dependent on initial spray characteristics and subsequent spray interactions with the opposing fire plume, which can deflect or reverse the sprinkler spray away from the targeted fire source. Measurements provide a comprehensive validation data set for computational fluid dynamics (CFD) spray models, as well as insight and engineering guidance to the spray-plume interaction important in fire sprinkler applications. An experimental facility consisting of an array of four sprinklers, similar to that of typical suppression system installations, is used to evaluate both quiescent spray dispersion and spray-plume interaction conditions. A 0.2 m×0.2 m centrally located forced air jet, with velocities ranging up to 4 m/s is used (in place of a fire) to provide a well-characterized, repeatable kinematic challenge to the spray. Measurements include quiescent case spray dispersion and local volume flux delivery to the plume source to evaluate spray penetration through the plume. Additional measurements include air jet centerline

drop velocity and drop size at variable source injection velocities to evaluate plume penetration behavior. These spray dispersion experiments capture the dominant transport physics and kinematic behavior of the spray plume interaction. Scaling analysis of the spray plume interaction is explored for two regimes of spray penetration; individual drop action and group spray action. In the individual drop action regime the droplets have a negligible effect on the plume and penetration scales with the ratio of drop terminal velocity to plume velocity. In the group action regime, a spray work criterion is proposed, accounting for drag interactions with the plume. The complete set of spray dispersion and plume penetration measurements comprise a data set of high resolution and well-characterized boundary conditions (including detailed initial spray measurements for each sprinkler in the array) useful for CFD validation.

THE INTERACTION OF SPRINKLER SPRAYS AND FIRE PLUMES

by

Eric D. Link

Dissertation submitted to the Faculty of the Graduate School of the
University of Maryland, College Park in partial fulfillment
of the requirements for the degree of
Doctor of Philosophy
2017

Advisory Committee:

Associate Professor André Marshall, Chair/Advisor
Associate Professor Christopher Cadou
Professor Marino diMarzo
Associate Professor Peter Sunderland
Professor Arnaud Trouvé

© Copyright by
Eric D. Link
2017

Acknowledgments

First I would like to thank my advisor, Dr. Marshall, for his support throughout my studies at UMD, starting all the way back when I began working in the lab with FireTEC. His endless ideas, insight, and feedback have made me a better researcher, scientist, and writer. In addition to my advisor, I would like to thank the project co-PI's, Drs. Trouvé and Sunderland, for their continual support during my student career and contributions to this research, as well as Dr. Howard Baum and the other members of my committee for their help. I would also like to acknowledge the Department of Fire Protection Engineering and the faculty and staff who helped me in my student career. Thanks to Olga for all of her help in the lab, and to Sharon, Mary Lou, and Nicole for their instrumental roles in the department.

A special thanks goes to the suppression research group, including Taylor Myers, Stephen Jordan, James White, and Sebastien Vilfayeu. Their feedback and help along the way is greatly appreciated. Additional help is appreciated from Rodney Bentley eased some of the tedious and wet measurements. Several interns came through FPE each providing valuable help in the lab—thank you to Jan Felix, Tim, and Juraj.

I would like to acknowledge and thank FM Global, particularly Drs. Yi Wang and Bert Yu, for supporting this project, along with the U.S. National Science Foundation (GOALI Award #1236788). This project would not have been possible without their support.

And finally, I thank my family for their constant support in everything I do.

Table of Contents

List of Tables

List of Figures

Chapter 1: Introduction

1.1 Research Objectives

The use of automatic sprinklers to provide suppression in the event of a fire continues to be a popular and effective strategy for reductions of loss of life and property. The overall success and performance of such protection systems depends heavily on the interaction and competition that exists between the water spray from ceiling mounted sprinklers and the upward motion of the fire plume. While these systems have been effective, particularly through the development of application specific sprinkler head designs, there is limited understanding of the interactions between the spray and the fire plume governing spray penetration and the resulting surface wetting. For the fire sprinkler, it is the spray penetration through the fire plume that will produce the greatest contribution toward fire suppression [1, 2]. Better performance and efficiency may be achieved through understanding of spray-plume interactions dominating sprinkler spray penetration and suppression.

There is a large gap in protection system design and specification. In general, design methods include the codified density/area method [3], or the use of more complex computational fluid dynamics (CFD) models to justify deviations from the

code. In either case, system design is done independently from knowledge about the specific sprinkler spray characteristics and the interaction with the fire environment and ultimate delivery of water to the surface. An intermediate complexity engineering-level tool for evaluation of sprinkler spray penetration may provide additional guidance to system design without adding the complexity of full scale fire modeling. However, performance-based design is becoming a widespread alternative protection strategy over prescriptive codes. To support engineering decision making, CFD models are being used extensively to design and justify fire protection system designs, including sprinkler suppression performance. The fidelity of sprinkler submodels in current CFD codes lags behind the desired predictive performance, in part due to the lack of accurate spray representation and sufficient validation data.

With these motivations in mind, the primary objectives of this research were to:

- provide a comprehensive experimental data set useful for CFD spray model validation, from initial spray to plume interactions to surface delivery
- refine methods for measurement of spray dispersion and spray-plume interaction
- establish a framework identifying potential plume penetration performance based on quiescent spray characteristics for engineering application

In support of these objectives, a medium-scale laboratory experimental facility was developed giving extra attention to precise experimental conditions and config-

uration alignment so that model inputs can be made consistent with experimental data. These details are crucial model inputs that are often absent in previous data sets. This experimental study was divided into four parts: characterization and measurement of initial spray properties, a study of spray dispersion from a sprinkler array in a quiescent environment, measurements of the spray-plume interaction in the presence of an upward momentum source, and an analysis of spray penetration to identify and evaluate governing scaling parameters. The experimental configurations yield detailed measurements for the purpose of model validation and an additional analysis of the measurements highlights improvements to dispersion measurement methods, provides deeper understanding to the physics of the spray-plume interaction, and suggests scaling laws for prediction of spray penetration performance.

1.2 Background

Fire continues to pose a challenge to life and property around the world, contributing to an estimated loss of more than $11 billion and more than 3000 deaths in the United States in the year 2014 [4]. While the total number of fires has been steadily declining over the past several decades, the death rate per 1000 fires and the estimated dollar loss per fire has remained constant [4]. These losses come despite updated building codes and technological improvements, attesting that fire suppression remains essential to the safety of occupants and the preservation of property. Water-based fire suppression methods are widely used for their effectiveness, sim-

plicity, and availability. Water-based methods include the suppression hose-streams typically applied by firefighting personnel, as well as automatically activated fixed position suppression systems utilizing water-mist nozzles or fire sprinklers. In particular, automatic fire sprinkler installations represent a predominant fire suppression strategy that has been established as a reliable and effective method to reduce property and life safety losses since their introduction in the late 1800s, and are widely used in all building occupancy types. An example of their success is presented in statistics by the National Fire Protection Association (NFPA) for residential fires (occurring between 2007 and 2011), where an 82% reduction in the fire death rate per 1000 homes and a 68% reduction in property damage was observed when sprinklers were installed [5]. Applications for commercial property protection are also important, as evidenced by the development of the early suppression, fast response (ESFR) sprinkler, ongoing research into special hazards protection, and the significant attention given to storage protection in the design codes [3].

The automatic fire sprinkler has become a ubiquitous fire safety system around the world, protecting property and occupants. Installations protect a range of design hazards from relatively straightforward cases like office buildings and residential property, to more challenging warehouse storage applications. Since the first automatic sprinkler in 1874, hundreds of different sprinklers have been designed attempting to improve performance in different applications, and dozens of sprinkler designs are commercially available today. Each sprinkler produces a unique spray dispersion pattern depending on the deflector shape, orifice diameter, and water pressure. Per-

formance is often characterized through evaluation of the spray pattern in terms of a water volume flux distribution on wetted surfaces; these spray patterns govern fire suppression efficacy. In fact, sprinklers may be designed to produce a specific spray pattern depending on the application. For example, ESFR type sprinklers with a downward biased spray pattern for plume penetration are used in warehouse storage applications [3,6] while residential type sprinklers with a wide spray pattern for wall protection are used in residential occupancies. These sprinklers are approved for fire protection use according to their performance in various standard tests, including spray pattern evaluation [7–9].

Development of model codes (e.g. NFPA 13 [3]) and legislation such as mandatory sprinkler protection provide guidance for best practices and instruction for proper system design and installation. As buildings are becoming more architecturally complex and the fire hazards being protected by sprinklers have evolved, cases that do not fall under the scope of the prescriptive codes are more common. The performance-based design concept uses engineering judgment and justification for fire protection designs that deviate from the codes. Often, CFD programs are employed to establish alternate designs to evaluate the expected performance of a given protection system, including suppression systems. Therefore, it is necessary for these calculations to produce accurate predictions of fire suppression behavior to justify design decisions. Reliable modeling could enhance safety and design code development and improve performance-based design techniques. Various challenges arise when predicting suppression performance, and this research aims to provide

a comprehensive data set for model validation, including measurements of initial spray characteristics, spray dispersion/propagation, and the interaction with a fire plume.

While it is acknowledged that water-mist and the evaporation of small drops (with nominal diameters less than 0.2 mm) to remove heat from the gas-phase flame region are used for suppression, in many applications, surface cooling of the burning fuel via delivery of water to the burning fuel surface is the most effective way to suppress a fire [1, 2]. To deliver the water spray to the burning surface, the spray must penetrate through the fire plume, overcoming the buoyant upward momentum. The level of penetration depends on the individual sprinkler spray patterns, plume strength, and relative location of the plume and spray sources. While these factors are of engineering interest, spray penetration is ultimately determined by clearly defined local spray-plume interactions. Without analytical methods to evaluate or predict performance, protection designs often depend on past experiences or empirical data from costly, specific large-scale fire suppression testing. Development of this experimental study included the goal of identifying critical scaling and engineering analyses that may predict suppression performance of fire sprinkler sprays through quiescent spray measurement and plume characterization, bypassing expensive empirical testing in fire situations.

1.3 Suppression Spray Research

Suppression spray research generally falls into several categories including dispersed spray volume flux measurement (spray patternation), initial spray measurement and characterization, spray-plume interaction, and numerical modeling. Additional research topics focus on water mists, gas-phase cooling, as well as identification of critical water application rates to achieve suppression. However, the current study is limited to fire sprinkler sprays and the penetration of such sprays to the surface. While these additional topics are important to water-based suppression including the use of fire sprinklers, these additional effects on the fire are beyond the scope of the analysis presented in this research.

Early measurements of sprinkler dispersion were conducted by Beyler [10] to investigate the influence of several variables on the volume flux distribution, including sprinkler installation orientation, flow rate, and frame arm position. Water was collected in 0.3 m square bins arranged on the floor in either radial or rectangular gridded patterns. For measurement of multiple sprinklers, the rectangular grid provided a simpler coordinate system and more complete floor coverage than the radial grid configuration. This early study introduced a spatial volume flux measurement method, but since that time only limited improvements have been implemented in subsequent studies. Results of these measurements show the significant influence that pressure, orientation, and water supply have on the resulting spray pattern. Due to experimental uncertainties, large collection bins, and lack of sprinkler char-

acterization, the data set is limited and inappropriate for model validation.

FM Global has provided many of the large-scale spray dispersion studies available in the literature. These studies focused on quantifying spray patterns through measurement of volume flux distribution, also termed local delivered density, both under quiescent conditions and in the presence of a fire, aiding in the development of the ESFR type sprinkler [6, 11, 12]. Local density measurements were reported by Yao [11], also using a series of 0.3 m square bins, arranged in a radial line and swept around the centerline to provide an azimuthal average measurement of the spray distribution area at various heights below the sprinkler. Other measurements using a radial sampling technique similar to Yao were performed by Prahl and Wendt [13] using 0.25 m square bins, although with an idealized axisymmetric sprinkler. In the large-scale testing by Factory Mutual (FM Global today), density measurements were taken in the presence of a fire in rack storage applications, where water was collected in a grid of 16 square pans approximately 0.5 m in width [12]. A more spatially-resolved measurement technique was used by Chow and Wong [14], who implemented a rectangular grid of 120, 0.25 m square collection bins to measure the spray penetration ratio in the presence of a wood crib fire. Their findings focused on the penetration ratio and the influence of the fire on spray dispersion rather than on spray measurement details. Overall, the technique for measuring spray dispersion has not changed significantly, and still relies on collection of water in large containers. Even in industries such as agricultural irrigation, where large-scale dispersion of sprays is critical, spray uniformity and distribution is measured using an array of

rain-measurement gauges [15].

As use cases for computational modeling in fire protection design become increasingly ambitious, validation of spray dispersion simulations has emerged as a critical research activity for the development of methods and models to predict water-based fire suppression performance. Missing from previous spray dispersion efforts is a complete data set resolving the details of spray dispersion (from initialization to delivery) for comparison with simulations. Several questions remain regarding sprinkler spray dispersion, such as the extent of spray pattern non-uniformity and best practices for accurate measurement of spatial variations in the spray, particularly for the purpose of model validation. The current industry standard for sprinkler tests is reflected in a number of standards by both Underwriters Laboratories and FM Approvals [7–9], using large 0.3 m (1 ft) collection pans and evaluating spray dispersion with pass/fail criteria based on a maximum allowable number of pans having a volume flux below a critical threshold value.

Additional studies have focused on measurement of spray properties, such as drop size and velocity distributions [16–18], developing ways to characterize and describe the spray as it is dispersed. Advancements in measurement technology have allowed expansion of the early data sets, yielding in-depth comprehensive descriptions of the spray [19–21]. One aspect of fire sprinkler sprays and the accompanying modeling efforts receiving detailed attention is the spatial variation of the spray characteristics. Unlike many other spray nozzles, fire sprinklers do not produce spatially uniform sprays. Even from visual observation of an operating sprinkler,

initial spray non-uniformities and their impact on far-field propagation are apparent, motivating the need for detailed spray measurements. More recent studies have quantified spatial variations in spray characteristics, such as volume flux distribution and drop size distribution, to support detailed analysis of fire suppression performance [19–25]. These measurements reveal elevation and azimuthal angle variations in near-field volume flux and other important spray characteristics, such as drop size and velocity, which appear to correspond to geometric features of the fire sprinkler head. These near-field spatial variations impact far-field volume flux and, in turn, may affect sprinkler performance. Implementation of these detailed initial-spray measurements can have a significant influence on the outcome of the model solution, providing more realistic results [25, 26]. Given the variations in volume flux variations in the near- and far-field, the variations in near-field measurement of drop sizes suggest that there are also variations in drop size at spatial resolutions comparable to the variations in volume flux (in addition to the natural drag filtering caused by the range of drop sizes within the spray). While volume flux might not be sub-critical for suppression, in these locations there may be differences in drop size that would influence the penetration ability on similar length scales to those identified as important for resolving the spatial volume flux.

Few experiments detailing water spray penetration through a fire plume have been conducted, presumably due to the high cost and complexity of large scale fire tests. Early measurements identify the effect of drop size on penetration [16], confirming that smaller drops, while effective at cooling the hot gases within a ceiling

jet or through entrainment, are ineffective at penetrating to the surface; larger drops (nominal diameter >0.5 mm) are needed for more efficient suppression. Much of the experimental data is from FM Global and the large-scale actual delivered density (ADD) apparatus which collects water on the floor in large collection pans below a heptane spray burner [12, 14, 18, 27, 28]. More recent experiments by Schwille [29, 30] explore penetration and the reaction of a fire plume to the momentum and drag imparted by a suppression spray and measure the velocity of drops in the plume region, showing substantial penetration reduction with increasing fire size. Additionally, the concept of a characteristic drag effect, rather than momentum competition between the spray and plume, was introduced. Redirection, velocity reduction, and reversal of drops was observed using PIV measurement techniques. Improved characterization of the plume boundary condition, as well as increased spray volume flux resolution, including at the location of the fire plume, would advance the comparisons to CFD models and provide a more complete validation data set. Schwille also looked at the effect of the interaction of the spray on the plume, identifying modified plume equations describing the effect a spray may have on the plume characteristics through drag forces [30, 31] as well as how the plume may affect drop motion [29] in the direct competition of aligned sprays and real fire from burners. Other small-scale experiments such as those by Zhou [24] investigate the directly opposed configuration with water mist and small plume configurations.

Due to the complexities of fire plume and spray interaction experiments, several studies using CFD simulations of sprinklers have been performed. Early sprin-

kler models used relatively low fidelity sprinkler injection and transport models simulating only a few trajectories with uniform drop sizes [32–34]. While insight to the penetration phenomena can be gained from these numerical experiments, results could be improved with increased spray fidelity and complete and appropriate measurements for validation of the models. More recently, higher fidelity models have been developed based on near-field initial spray characterization [22, 23]; these models have been successfully used to simulate complex dispersion [35] and suppression [36] scenarios. The complexity of these simulation scenarios provides a realistic challenge for model capabilities, but limits insights into spray physics and utility for validation of the models.

The experiments conducted in this study seek to address gaps regarding CFD model validation and engineering insight of spray-plume interactions using a medium scale laboratory experiment with well-documented spray conditions in both quiescent and spray-plume interaction studies, using an array configuration with the plume located away from the sprinklers rather than the common centerline configuration used in the detailed studies to date. Measurements of initial spray characterization, delivered volume flux, local spray-field characteristics, and penetration measurements with both strong plume and strong spray conditions will contribute a comprehensive data set for model validation and physical insight to the spray-plume penetration.

1.4 Current Work

Multiple measurements and diagnostics were implemented to explore the physical phenomena involved in the spray-plume interaction and to obtain experimental data suitable for CFD model validation. The measurements consist of four different sets, including

1. Initial spray characterization
2. Quiescent spray dispersion
3. Spray-plume interaction
4. Spray-plume penetration

These measurements were accomplished using two experimental facilities in a wet lab designed to contain water spray experiments. Initial spray characterization was performed using the spatially-resolved spray scanning system (4S) [25], detailed in Ch. 2. The dispersed spray and spray-plume interaction measurements were conducted in the sprinkler array facility (SAF), and are detailed in Ch. 4 and Ch. 5, respectively.

The SAF consisted of a square grid of 4 sprinklers, typical of sprinkler suppression system installations, allowing the use of multiple sprinklers and a configuration where the suppression target was located in-between sprinklers representative of a potential worst case scenario where the fire is not directly below a given sprinkler. Measurements in the SAF required two configurations of the facility, sketched in

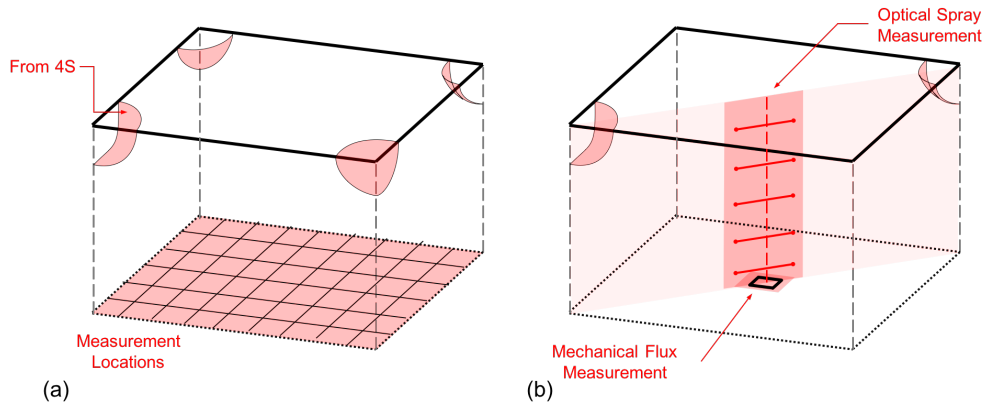

Figure 1.1: The sprinkler array facility was configured in two ways for (a) spray dispersion and (b) spray-plume interaction measurements. Active measurement areas in each configuration are highlighted.

Fig. 1.1. Quiescent spray dispersion measurements were taken from the full array of sprinklers, indicated in Fig. 1.1a by the highlighted measurement areas of initial spray locations and the full floor coverage. For measurement of spray-plume interaction, the modified configuration shown in Fig. 1.1b was utilized with two sprinklers and a central vertical plane region for measurement of spray characteristics and behavior using optical methods.

The detailed spatial measurements of the spray, both at initial formation and during interactions with the plume, with careful attention given to alignment, resolution, and operating conditions, provide a comprehensive data set useful for CFD spray transport model validation. Along with the validation data sets from detailed measurements of spray dispersion and spray-plume interaction, additional insight and understanding can be derived from the results. The analytical approach includes a resolution analysis of the spray dispersion measurements providing insight

into sprinkler spray length scales and guidance for accurate measurement of sprinkler sprays. A scaling analysis framework for evaluating spray-plume interactions to predict spray penetration to the target surface is also presented. Specifically, the penetration scaling analysis is based on a sprinkler's unique spray pattern quantified through quiescent dispersed local spray characteristics (obtained from either far-field measurements or from predictions informed by initial spray measurements). The goal of this analysis was to provide a foundational suppression engineering framework based on recent sprinkler measurement and analysis innovations to support design analysis and to reduce reliance on large scale fire testing.

Chapter 2: Initial Spray

Various sprinkler designs are available for different hazard protection applications, and each produces a unique, non-uniform spray depending on deflector geometry and operating pressure. Because the formation of the spray is dependent on a solid jet impinging on a shaped deflector, the geometry of the deflector plate is a significant factor in the spray pattern each sprinkler generates. These variables determine the spray pattern and characteristics of the spray, including the volume flow rate, the spatial distribution of the volume flux, the drop size distribution, and the initial velocity of the drops. These three main parameters, volume flux, drop size, and drop velocity, influence how the spray will interact with the plume.

A critical factor for successful modeling of spray dispersion is the fidelity of the boundary conditions. Due to the complexities in deflector design, it is beyond the scope of current analytical approaches for a direct calculation of the initial spray. Work by Myers [37] pushes the boundaries of such calculations, predicting sheet formation and velocities from a simple deflector geometry, which could be used for further calculation of spray distributions. Nevertheless, current implementation of sprinkler sprays in computer modeling is dependent on the specification of general spray characteristics, including drop size distribution, initial velocity, and volume

flux [26, 38, 39]. Given that each sprinkler is unique, the precision of a spray model is highly dependent on the initialization characteristics. Therefore, measurement of the initial spray characteristics is essential to providing high fidelity CFD boundary conditions as well as inputs to more general engineering analyses to predict sprinkler performance.

2.1 Experimental Facility

Detailed near-field initial spray measurements were obtained using the 4S. This facility, first conceived by Ren et al. [20, 40], and further developed by Jordan et al. [25], measures the total volume flux of the spray along with the diameter, velocity, and number density of drops after their initial atomization. Because these spray characteristics vary spatially with respect to the sprinkler, measurements are taken along a continuous spherical surface surrounding the sprinkler, known as an initialization sphere [19,21]. A significant feature of the 4S is its ability to rotate the sprinkler while keeping the measurement devices fixed in place, providing spatially continuous measurement around the sprinkler. A schematic diagram of the 4S shows the configuration of the facility in Fig. 2.1. The centrally located sprinkler is situated between two measurement devices; an array of water collection funnels are positioned on one side, while a LaVision laser/camera optical system is positioned on the opposite side.

Water is supplied to the system by a pump from an underground storage tank. The water flow rate is controlled by an electronic valve monitored by a proportional-

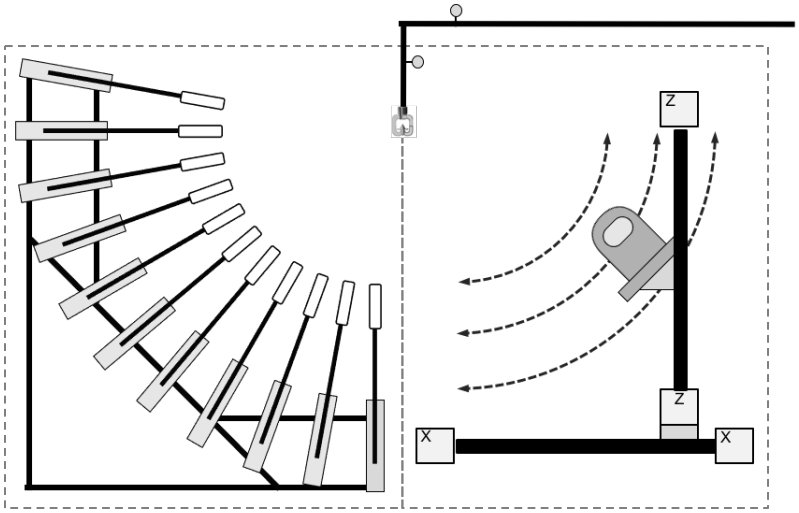

Figure 2.1: Schematic diagram of the 4S initial spray facility. Mechanical collection of volume flux is achieved with the funnel caps and collection cylinders, while optical measurement of drop size, velocity, and volume flux is achieved with a LaVision laser system.

integral-derivative controller (PID controller) to maintain a constant flow condition.

2.2 Sprinkler Details

For accurate spray initialization in CFD models, future model validation, and compilation of a comprehensive data set in the current research study, measurements must pay significant attention to consistent and repeatable spray conditions. Particularly important are sprinkler details and alignment. A set of four Tyco D3 spray nozzles was used throughout this study, each numbered for identification. The Tyco D3 spray nozzle used for this study produces widely-dispersed sparse sprays consistent with standard pendant sprinklers. This particular nozzle has a horizontal deflector consisting of 12 rotationally symmetric slot/tine pairs with no geometric abstractions, shown in Fig. 2.2. Also shown in Fig. 2.2 is a reference datum identified by the frame arm to maintain a known angular orientation. This position identification is important to maintain consistency between sprinklers and in the initial spray measurements for accurate model input values. Position around the sprinkler is identified by an azimuthal angle, ϕ, and an elevation angle, θ, also identified in Fig,2.2. The elevation angle is measured from the upward vertical direction at $\theta = 0^\circ$ to $\theta = 180^\circ$ directly below the sprinkler. The azimuthal angle is set such that the frame arms are positioned at $\phi = 90^\circ$ and 180°. Azimuthal angle is positive in the counter-clockwise direction, following a right-hand rule convention with the sprinkler in its operational orientation (e.g., pendant) and the vertical axis in the upward direction.

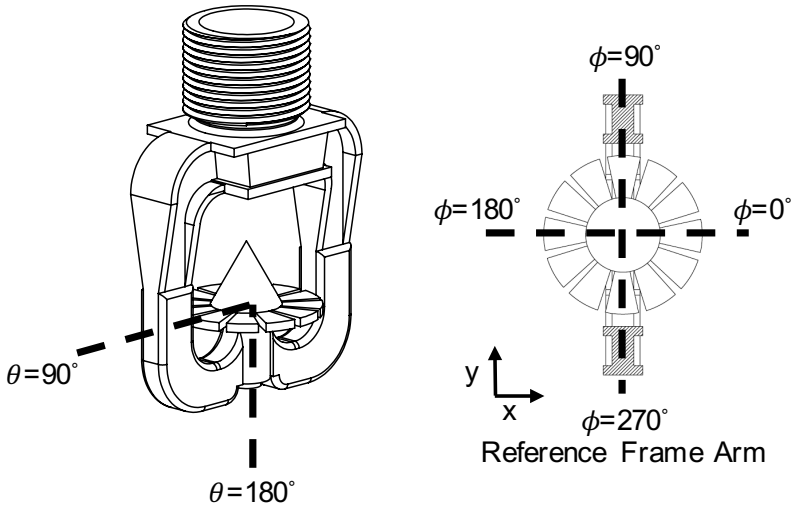

Figure 2.2: The Tyco D3 spray nozzle with k-factor 33 LPM/bar$^{1/2}$ was used throughout this research. The deflector consists of 12 slot/tine pairs, and sprinkler were aligned according to the labeled reference frame arm.

2.3 Measurements and Diagnostics

Characteristics of the initial spray, including volume flux, drop size, and drop velocity, are measured along the initialization sphere, a location where the initial water jet has atomized and broken into a spray, using the physical collection tubes and optical imaging equipment shown in Fig. 2.1. For the Tyco D3 sprinklers used in this study, the initialization sphere radius was 0.4 m from the sprinkler.

The primary measurement of volume flux is achieved by collecting water as it passes through the initialization sphere. An arc of 11 collection funnels is located at a radius of 0.4 m from the sprinkler, covering elevation angles centered from $\theta = 80°$–$180°$, measured from the upward vertical axis, shown in Fig. 2.1. Water is collected

in each of the 11 elevation angle collectors continuously as the sprinkler makes a full 360° azimuthal rotation. The rate of water accumulation is measured in each collection tube to determine the volume flux. Simultaneous water collection in each of the elevation angle tubes allows the volume flux to be completely characterized in one revolution. The azimuthal angle of the sprinkler is recorded as the sprinkler rotates, allowing for the volume flux measurement to be mapped to a precise location on the initialization sphere.

Located 180° across from the flux collectors is a traversing LaVision laser shadowgraphy system used to capture images of the spray used to optically measure the diameter, velocity, and number density of the drops. The optical equipment is positioned at the initialization radius at discrete elevation angles. As the sprinkler rotates, images are captured at a rate of 6 Hz. Rotation times extend as long as 50 minutes to acquire a sufficient number of images at each azimuthal location to ensure the motion does not influence the results and blur the spatial gradients. Accumulated over the 11 elevation angles, raw image data for an entire sprinkler characterization consists of over 150,000 image pairs and approximately 600 GB of data. This massive amount of data is processed using the DaVis LaVision software package to identify and measure millions of individual drops, reducing the dataset to a nominal 500 MB size listing all of the drops identified. Similar to the mechanical measurement, the azimuthal and elevation angle location relative to the sprinkler is known for each image that is captured, and the drop size distribution and drop velocity can be extracted from the images and mapped onto the initialization sphere.

Additionally, volume flux can be calculated from the optically measured quantities, providing a validation of the mechanical collection method. Due to the rigorous alignment procedure of the sprinkler datum and the automated control of sprinkler rotation and flow rate, repeatability of the measurement is very good. Errors associated with position and local flux error are less than $\pm 1\%$ and $\pm 2\%$, respectively [25].

2.4 Measurement Results

Each individual sprinkler used in this study was measured with the 4S, providing detailed quantification of the spatial variations in drop size, velocity, and volume flux. The result is a complete description of the initial spray that comes from each sprinkler which can be used for high-fidelity model initial conditions for spray dispersion modeling and engineering analysis. The initialization sphere is shown in Fig. 2.3, where the shaded region indicates an example of the quarter of the hemisphere directed into the array. Results of the 4S characterization measurements are plotted using this template.

Volume flux measurement results are presented in Fig. 2.4 for the four sprinklers used throughout this research, the Tyco D3 sprinkler with k-factor $33.1\,\mathrm{LPM/bar^{1/2}}$ operating at $1.38\,\mathrm{bar}$, labeled with their corresponding identification number. Multiple characteristics of the particular deflector geometry can be seen in the spatial distribution of volume flux. The slot-tine pattern can be identified by the repeating areas of high flux near the equator caused by flow off the

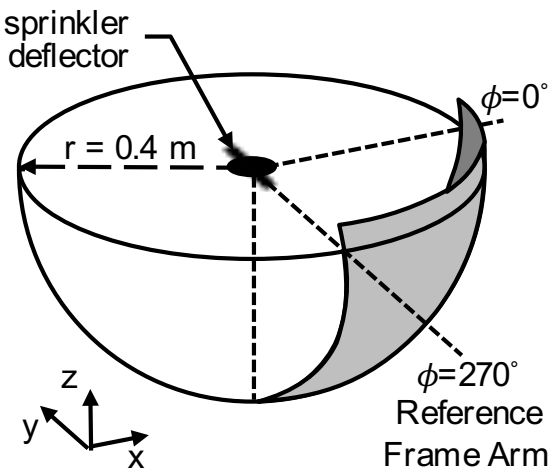

Figure 2.3: The initialization sphere is located around the sprinkler, with the azimuthal angle reference positions $\phi = 0°$ and 270° identified with the short dashed lines. Sphere measurement results are plotted as a quarter hemisphere shown by the shaded region.

tine, alternating with vertical streaks corresponding to spray flowing from the slots following a more vertical initial trajectory. Frame arms of the sprinkler are also seen to have an effect, situated at azimuthal angles of 90° and 270°. The effect is particularly pronounced in sprinkler #2, where a significant spray shadow is cast in the $\phi = 270°$ direction. Additionally, due to the geometry of the sprinkler deflector, a significant flow of water is observed coming from a deflection off the frame arm. These non-uniformities will propagate as the spray is dispersed, and may have a significant influence on plume interactions and suppression. Each quarter hemisphere represents the quadrant of the spray that was directed into the square array area, with measurements spanning from directly below the sprinkler to 10° above horizontal (elevation angles $\theta = 80$–$180°$), as highlighted in Fig. 2.3. The circled numbers

correspond to the sprinkler identification number, consistent throughout this study. While Fig. 2.4 shows measurement results of volume flux, similar non-uniform patterns are observed in the other quantities measured from the 4S shadowgraphy. Complete initial spray characterization results of volume flux, volume median drop size, drop distribution parameter, initial drop velocity, and drop break-up radius are presented in Appendix A for each sprinkler.

Although there are similarities between sprinklers, as shown in Fig. 2.4, it is apparent from these measurements that even sprinklers of the same model produce different spray patterns despite the same deflector design and operating conditions. In the interest of providing experimental data for model validation, it is important to measure the exact variations between sprinklers so that the accuracy of the model can be validated. By measuring each sprinkler independently, sprinkler-to-sprinkler variations are accurately documented and the relation of spray patterns in the near-field can be linked to subsequent spray dispersion. While there are similarities between the general patterns, the differences of the initial spray will propagate, leading to unique spray patterns on the floor, discussed in Ch. 4.

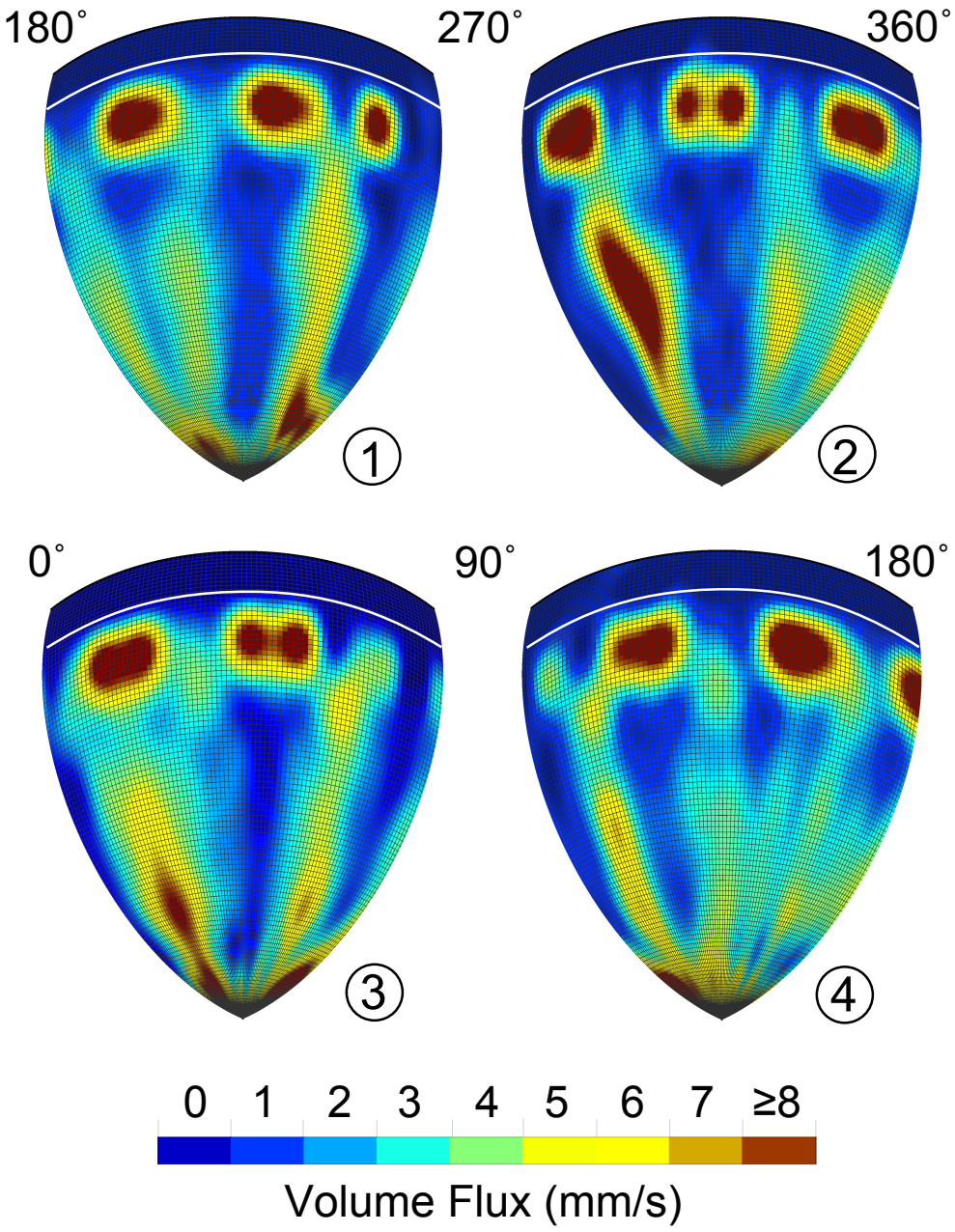

Figure 2.4: Spatial volume flux measurements of the initial spray plotted on quarter hemispheres for the four Tyco D3 sprinklers, k=33.1 LPM/bar$^{1/2}$ operating pressure was 1.38 bar, directed into the sprinkler array configuration. See Fig. 2.3 for definition of the quarter hemisphere.

2.5 Summary

Detailed measurements of the initial spray were taken for each of the four Tyco D3 sprinklers used throughout this research. The particular sprinklers had a k-factor of 33.1 LPM/bar$^{1/2}$ and were operated at a pressure of 1.38 bar, flowing 38.9 LPM. Measured quantities include spatially-resolved volume flux, drop size, and drop velocity. From these measurements, the drop size distribution parameter, γ can be determined, as well as the sheet break-up radius. The collection of these important spray parameters completely describe the initial spray from the sprinkler.

Accompanied by the installation orientation and identification of the individual sprinklers, the measurements provide a complete set of injection parameters that can be used for modeling of sprinkler sprays, including relatively simple drop tracking models, or more comprehensive CFD models such as FireFOAM. The data set provided will allow for more accurate sprinkler spray initialization and allow for increased confidence in CFD spray modeling validation.

Chapter 3: Sprinkler Array Facility Design

Measurements of spray dispersion and spray-plume interactions were taken using the sprinkler array facility, seen in the schematic of Fig. 1.1. Several variables have an influence on spray-plume interactions and ultimately spray penetration, including sprinkler height, spacing, flow rate, operating pressure, drop size distribution, fire plume size, and fire momentum. While all of these parameters have an influence on the penetration effectiveness, when considered all together they define the localized interactions that govern the spray-plume interaction. The sprinkler array facility was designed with the goal to provide a medium-scale experimental facility which maintained similarity to real-world sprinkler applications while providing two general localized spray-plume interaction regimes, supporting experimental conditions where penetration was achieved through individual drops in the spray (Sec. 6.3), or where the accumulated drag forces of the spray contributed to the penetration (Sec. 6.4). The sprinkler arrangement, sprinkler operating condition, and plume strength were all considered together to develop the SAF.

3.1 Plume and Sprinkler Arrangement

The square array configuration allowed the exploration of different plume locations within a typical arrangement of sprinkler protection systems, with different possibilities shown in Fig. 3.1. Much of the previous research with detailed measurements has been conducted with a single sprinkler located directly above the fire source [24, 29–34, 41]. While such a configuration is simple and allows for the direct study of the interaction of the spray and plume, it is not a general representation of the suppression problem. A fire may be located anywhere in relation to the sprinkler locations, including a potential worst-case scenario in-between the sprinkler spacing. The grid configuration allowed for this variable location arrangement, and has been explored on a large scale with limited local diagnostics [11, 12, 16, 18, 28]. Spray characteristics from the given sprinklers vary depending on location, and through different spacing of the sprinklers from the central plume, different interaction regimes could be achieved. The facility design accommodates a maximum sprinkler spacing of 2.65 m, on the same order of magnitude with typical sprinkler installations which range from 2.4 m–6 m spacing depending on the sprinkler type.

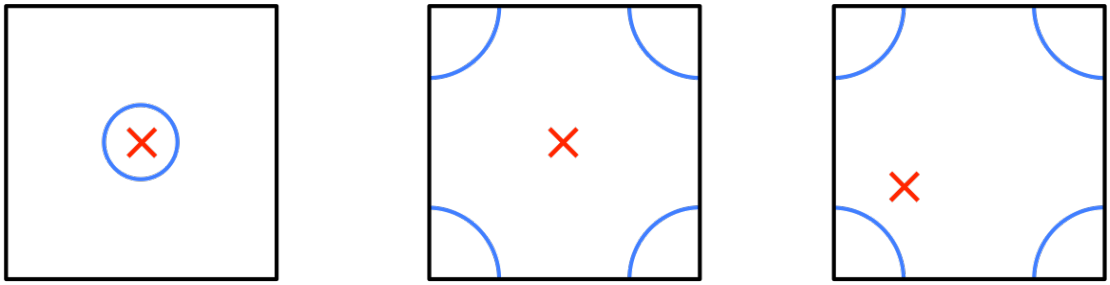

Figure 3.1: Possible plume locations (×) included direct alignment (left), centered alignment (center), or a random alignment (right) closer to one sprinkler.

3.2 Sprinkler Selection

The Tyco D3 spray nozzle, previously introduced in Sec. 2.2, was selected for its simple repeating geometry while maintaining consistent geometric features of typical pendant fire sprinklers, such as the tine/slot deflector design and the inclusion of frame arms, depicted in Fig. 2.2. The Tyco D3 nozzle is available in a variety of orifice diameters to provide a range of flow rates and drop size distributions. Drop sizes from the Tyco D3 are nominally 0.7 mm, within the range of typical sprinkler drop sizes, predicted between 0.4 mm and 2.4 mm based on a median volume diameter drop size.

Limitations of the lab space water flow rate and minimum operating pressure requirements constrained the size of sprinklers for selection. To ensure good spray formation, a constraint for minimum operating pressure at the orifice of 0.5 bar was imposed, also consistent with minimum operating pressures of fire sprinkler

installations [3]. Based on lab water flow capability, a maximum of approximately 224 L/min was available, leaving a maximum of 56 L/min from each of the four sprinklers in the SAF. This maximum flow rate can also be viewed in terms of an operating pressure, P, through the relation $Q = k\sqrt{P}$, where Q is the flow rate, and k is the sprinkler k-factor. The limiting case where the flow rate and minimum pressure constraints meet occurred at a nominal k-factor of 80 LPM/bar$^{1/2}$. Therefore, any sprinkler larger than this orifice size is unsuitable for the current facility.

Along with the operating pressure considerations, drop velocity and spray momentum were considered to further determine the specific sprinkler selection.

3.2.1 Drop Velocity Considerations

Penetration of individual drops in the spray through the plume is dependent on the velocity of the drops. To reach the target surface, drops must maintain a downward velocity. Because drop size is directly related to the drop terminal velocity, the drop size distribution was estimated for various operating pressures to help determine an appropriate pressure and sprinkler size. Details about the drop velocity calculations and considerations are presented in Appendix B. The goal was to use a sprinkler that generated a sprinkler spray within the general operating conditions found in fire sprinkler applications, while also providing drops with terminal velocities in a range that could be challenged by the competing plume velocity.

3.2.2 Spray Momentum Considerations

The relationship of momentum of the spray and plume have also been identified as important parameters in the spray-plume interactions [6, 11, 12, 24, 30, 34]. Initial design of the facility considered this momentum competition. From previous suppression testing, the spray was observed to to penetrate to the fuel source if the ratio of spray momentum to plume momentum was greater than 1 [41]. In order to provide a range of possible conditions where the spray momentum was in a typical range for penetration, a range of spray/plume momentum ratios was considered, from $0.2 < \dot{M}_s/\dot{M}_p < 2$.

What was not clear from the outset was the appropriate characteristic momentum. Previous work has identified characteristic spray momentum as the injection momentum, or the initial momentum measured on a strike plate near the injection location. Others consider the momentum of the spray distributed over the entire reach of the spray. A general first order estimate of the spray momentum can be calculated by the product of the volume flux, $\dot{V}''$, and spray velocity, v, $\dot{M}_s = \dot{V}''v$. In the current analysis, a local momentum is considered based on the location and coverage area of the spray and plume. Rather than use a strict momentum ratio where the spray momentum is considered as a characteristic injection value, it may instead be considered as a local area based value,

$$\frac{\dot{M}_s(A_s)/A_s}{\dot{M}_p/A_p} \tag{3.1}$$

where the momentum is considered as a localized area modified momentum ratio.

The selected area of influence determines the relevant spray momentum. This area could be the total area of the spray at a characteristic height, or it could correspond to the area of the plume that it is competing against. Multiple estimates of spray momentum based on different characteristic areas were considered, and details of the calculations are presented in Table B.1 in Appendix B. Additional discussion about spray momentum, and the applicability to the spray-plume interaction phenomena is discussed in Sec. 6.4. While the spray pattern and distribution of volume flux has a significant influence on the downward spray momentum, based on the typical volume fluxes and drop velocities produced by the spray, it is assumed that the spray momentum is also typical of a typical standard spray or residential sprinkler.

3.3 Plume Design Considerations

One of the important parameters governing the spray-plume interaction and eventual penetration of the spray to the surface of the burning fuel is the relative velocity of the drops within the spray and the competing fire plume. Two characteristic velocities were considered for the plume, determined through ratios to relevant spray velocities. Penetration based on individual drop behavior has been shown to depend on drop size and corresponding drop terminal velocity. The ratio of drop terminal velocity to the plume velocity (discussed in more detail in Sec. 6.3) is the more important factor governing drop penetration, while the kinetic energy of the plume, determined by $\rho_a u^2/2$, is important when considering the influence of accumulated drag forces from the spray (discussed in Sec. 6.4).

For repeatable, well-characterized experimental conditions, a forced-air jet at ambient temperature was used throughout the experimental testing. In the forced-air method of plume generation, the plume design considered two main variables, diameter and flow velocity, with the objective of providing a range of velocity conditions to compete with the spray. As the plume diameter increases, the volume flow rate required increases for the same plume velocity. However for smaller plume sizes, the pressure drop due to duct sizing is increased, restricting the amount of airflow available. The plume design converged on the $0.2\,\mathrm{m} \times 0.2\,\mathrm{m}$ size based on preliminary testing of pressure drop and flow rate from air ducting to deliver the plume to the center of the array. The maximum sustained velocity was $3.7\,\mathrm{m/s}$. More details of the plume velocity profile and construction are presented in Sec. 5.1.

While the current plume region is defined by an ambient temperature air jet, the characteristic velocity still maintains reasonable similarity to velocities within real-world medium scale incipient fires. For example, using fire plume centerline correlations developed by Heskestad [42], the centerline plume velocity for a $300\,\mathrm{kW}$ fire is approximately $6\,\mathrm{m/s}$. While the $3.7\,\mathrm{m/s}$ velocity is slightly lower than this fire plume velocity, the important velocity relationship with the plume is ultimately not the absolute velocity, rather the velocity and kinetic energy ratios presented in Sections 6.3 and 6.4.

3.4 Summary

Design of the sprinkler array facility considered the arrangement of sprinklers and the relative velocity and momentum competition between the spray and the plume. The array configuration allowed for a more general and potentially worst-case location of the fire plume suppression target in relation to the sprinkler locations. Selection of the sprinkler operating condition considered the influence of orifice diameter and operating pressure on the drop size distribution that would be produced, and the resulting ratio of drop terminal velocity to plume velocity. While it was unclear from the beginning of the research what the critical spray and plume momentum comparison was, previous research indicated a range of spray/plume momentum ratios.

The design parameters of the sprinkler array facility are summarized in Table 3.1. A sprinkler k-factor 33.1 $\mathrm{LPM/bar^{1/2}}$ was selected at an operating pressure of 1.38 bar. At this operating condition, the characteristic drop velocity and momentum criteria were met and drop characteristics and plumes compared favorably on the same order of magnitude with length and velocity scales present in sprinkler applications.

Table 3.1: Predicted test capabilities of the sprinkler array facility for design decisions.

Parameter	Design Value	Typical Range
k-factor	33.1 LPM/bar$^{1/2}$	43–360 LPM/bar$^{1/2}$
Operating pressure	1.38 bar	0.5–12 bar
Spacing	2.65 m	1.8–6 m
Height	1.5 m	2–15 m
Predicted d_{v50}	0.72 mm	0.4–2.4 mm
Max. u_{plume}	3.7 m/s	5–10 m/s

Chapter 4: Dispersed Spray

Because sprinklers are a reactive means of protection and cover a general area without adjustable aiming direction, dispersion of the spray is critical for fire suppression and surface cooling. Prior to the additional complication of a competing fire plume, initial measurements were taken of quiescent spray dispersion within a square array configuration, previously presented in Fig. 1.1. Volume flux delivery to the floor 1.5 m below the level of the sprinklers was measured for a quadrant of a single sprinkler, as well as for the simultaneous operation of a full array of four sprinklers. Important outcomes of the quiescent spray dispersion case include a dataset for model validation of spray dispersion which partners with the initial spray measurements from Ch. 2 to form a complete dataset describing the distribution of the spray, as well as an analysis of the spatial-resolution of such measurements. The spray dispersion measurement and analysis presents validation data and physical insight for a basic quiescent environment.

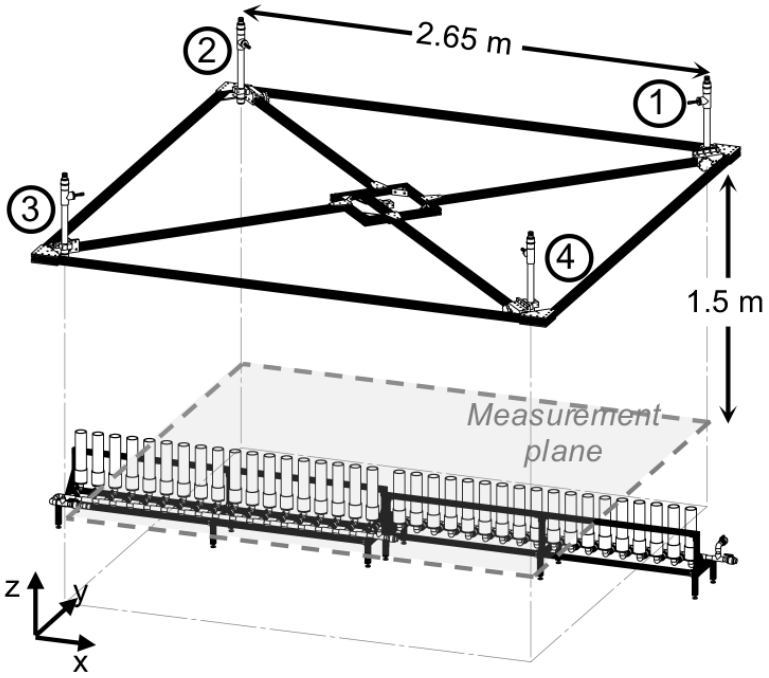

Figure 4.1: Drawing of the experimental facility showing the arrangement of the sprinklers and the water collection tubes. The circled numbers identify each sprinkler.

4.1 Experimental Facility

The sprinkler array facility (SAF) was developed for far-field dispersed spray measurements. The SAF incorporates the common grid building block found in typical sprinkler installations, with unique sprinklers located at each corner identified by the numbers in Fig. 4.1. Sprinklers were located in a square configuration spaced by 2.65 m on each side of the array.

All four sprinklers are the Tyco D3 spray nozzles shown in Fig. 2.2. The four sprinklers were operated simultaneously at 1.38 bar. With a k-factor 33.1 LPM/bar$^{1/2}$,

the total flow rate was 38.9 LPM from each sprinkler. As was shown in Fig. 2.4 the measured spray pattern is unique for each individual sprinkler, so all sprinklers were given identifying numbers and the angular position of each was carefully aligned, with the reference directions and angles consistent with those shown in Figs. 2.2 and 4.1. Sprinkler frame arms were parallel to the y-axis in Fig. 4.1 and the 0° azimuthal angle directed to the positive x-axis.

Water was supplied to the system by an underground storage tank and pump. Flow rate was regulated with a valve coupled to an electronic controller monitoring the total pressure just upstream of each sprinkler. Pressure measurements were acquired with an Omega PX302 pressure transducer, with range 0–13.8 bar and accuracy 0.25% BFSL. Timed bucket-filling tests were performed to verify the flow rate and to confirm equal flow rates from each sprinkler.

4.2 Measurements and Diagnostics

Dispersed spray volume flux measurements over the floor area, $\dot{V}''$, were obtained with a linear array of collection cylinders as seen in Fig. 4.1, with openings located 1.5 m below the sprinkler deflectors. The inner diameter of each collection cylinder measured 52 mm, with an outer diameter of 60 mm. The measurement area of the cylinders covers 85% of the total measurement area. The linear array was manually positioned parallel to the x-axis at y-position increments of 0.05 m such that the entire floor area within the sprinkler array was measured over a series of tests. The test procedure began with the collection tubes covered while the water

flow-rate stabilized at a steady-state operating pressure. At this point the tubes were uncovered and water was collected for 10 minutes before the tubes were covered once again. After the water flow was terminated, the water pressure head in each tube was measured.

Consideration was given to flux collection in a radial coordinate system similar to previous researchers [10, 13, 14] due to the two-dimensional radial motion of the spray from the sprinkler. However, this convenience breaks down in two ways. First, the use of multiple sprinklers are implemented in a square, guiding measurements to a grid configuration. Additionally, the radial configuration also leads to insufficient measurement resolution as the radius from the sprinkler increases. Details about the spatial resolution of the flux measurement are discussed in Sec. 4.4.1.

Volume flux is calculated by determining the volume of water collected in the collection tubes during the specified test duration. A Setra 209 pressure transducer, range 0-0.07 bar and accuracy $\pm 0.25\%$ FS, measured the pressure head of water accumulated in each tube. Using the cross-sectional area of the collection tube, A_t, the area of the tube opening, A_o, the measured pressure head, Δh, and the collection time duration, t, the volume flux was determined by

$$\dot{V}'' = (A_t \Delta h)/(A_o t) \tag{4.1}$$

An in-place calibration of the pressure transducer was performed to establish the accuracy and repeatability of the water column height measurement by adding a known volume of water to the collection array. The calibration incorporated possible sources of error in the water height measurement, including the leveling of

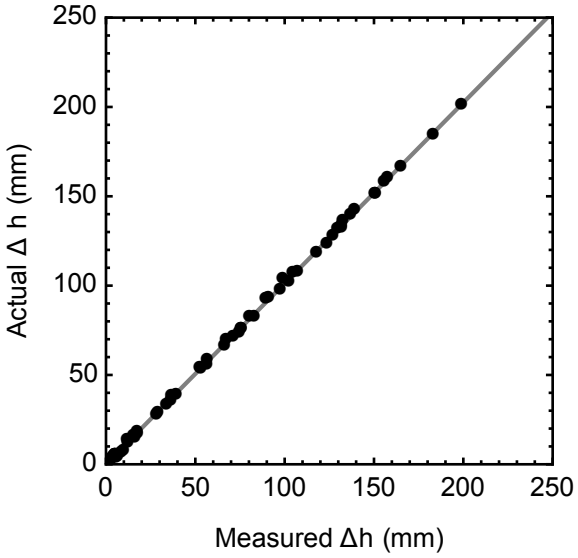

Figure 4.2: Calibration of the volume flux pressure transducer shows the actual height of the water column is 1±0.26% higher than the measured value, contributing minimal error to the measurement. Best fit line is $y = 1.01x$.

the collection array, manufacturing differences in tube diameters, and the fraction of water drops that remained on the side or edge of the tube. Calibration of the pressure transducer measurement determined the measured height to be linear within 0.26% of the actual height at a 95% confidence level, with calibration results shown in Fig. 4.2. This component of the measurement contributes very little to the overall measurement uncertainty due to the high accuracy of the pressure transducer. The larger sources of uncertainty are presented by other variables including positioning of the collection tubes, water pressure variations, temperature, room airflow, or other variations in spray pattern from day to day. The repeatability of measurements including all of these factors is detailed in Sec. 4.4.1.

Due to the stochastic nature of a spray, a given volume flux measurement may not provide a statistically resolved value of spray flux. To ensure statistical resolution, a minimum number of drops must be collected in each sample. It is accepted that a large sample size of 10,000 collected drops provides a well resolved measurement. A minimum volume flux may then be established by using the volume of that number of drops.

For the current experimental configuration, the minimum measurable flux was limited by the statistical volume requirement rather than the ability to measure small changes in height. One complication with this method requires the knowledge of the droplet sizes to determine the volume of the sample collected. The spray in the current experiment has a measured volume median diameter, d_{v50}, of 0.55 mm using the 4S. By using a drop diameter of 1 mm for the calculations, the statistically determined volume will provide a conservative value for the minimum flux by overestimating the volume of each drop. Using the 1 mm drop diameter, the collection area of 0.002 m^2, and test duration of 10 minutes, the minimum statistically significant flux is 0.25 mm/min. Any data measured lower than this threshold are not considered to be reliable in terms of a time average measurement.

Based on the fluxes expected in a given measurement, the experimental parameters in Eq. (4.1) can be controlled by the experimenter to fine tune the configuration. For example, given a statistically large number of drops, the minimum measurable flux can be lowered to a more precise value by increasing the test duration or decreasing the cross sectional area of the tube. By placing a funnel on top

of a smaller cylinder, the collection area can remain the same while improving the response of the pressure transducer by increasing the accumulated height within the cylinder.

4.3 Floor Volume Flux Measurement Results

4.3.1 Single Sprinkler

Volume flux measurements at the floor were taken for a single sprinkler (sprinkler #1) located in the corner of the array facility, with results plotted in Fig. 4.3. In this case, the data set consists of 1296 measurements on a uniform 0.1 m×0.1 m grid with the sprinkler located at (x, y) location $(0, 0)$ as indicated by the identifier in Fig. 4.3. Funnel caps with diameter 0.1 m were placed on the collection tubes to reduce the resolution and the number of measurement sets to complete the full spatial map. Figure 4.3 depicts the measured dispersion volume flux of D3 sprinkler #1 at 1.35 bar from a height of 1.5 m. Placing the sprinkler in the corner allowed for the total throw radius of the spray to be measured with a mean of 3 m, indicated by the white contour line at a measured flux of 0.2 mm/min. Additionally, because the total throw was captured, a mass conservation check was possible. The integrated flow to the quadrant totaled 26.6% of the total flow rate. While a 25% fraction would be expected based on the 1/4 coverage area collected, this slightly increased value agrees well with the 25.9% measured in the corresponding section of the initial spray measured with the 4S. This indicates that the initial spray itself is not equally

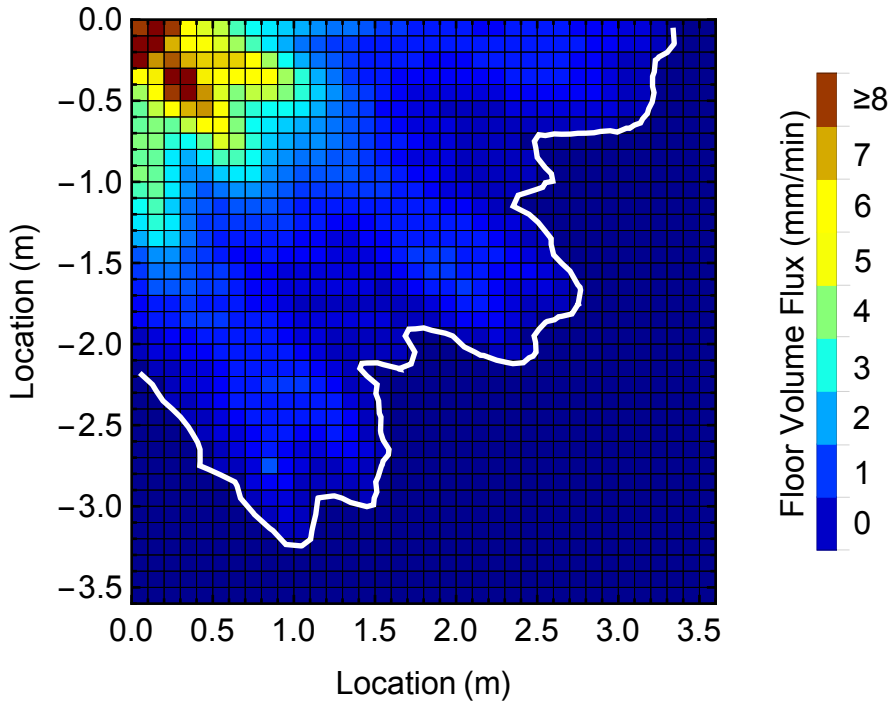

Figure 4.3: Volume flux of a single sprinkler (#1) was measured on a 0.1 m grid at 1296 locations on the floor 1.5 m below the sprinkler. The edge of the spray is indicated by the white outline.

distributed around the sphere, agreeing with the spatial variations seen in the initial spray measurements. The combined measurement of the initial spray (Ch. 2) and the volume flux at the floor capturing the full extent of the spray provides a useful validation data set for quiescent spray modeling before introducing the increased complexity and computational expense of multiple sprinklers.

4.3.2 Sprinkler Array

Volume flux measurements on the floor from the simultaneous full array of four fire spray nozzles is shown in Fig. 4.4, consisting of 2970 measurement locations. The individual sprinklers are also identified in the figure, along with the orientation of the frame arms along the y-axis. Non-uniformities in the dispersion are evident by the radial finger-like structures from the centerline of each sprinkler that appear to correlate with the specific deflector geometry and frame arms. Note the same features exist in the initial spray volume flux measurements in Fig. 2.4 due to the slots and tines of the deflector geometry. Another notable non-uniformity is the spray shadow caused by the frame arms along the vertical borders of the domain, indicated by the blue areas with low volume flux.

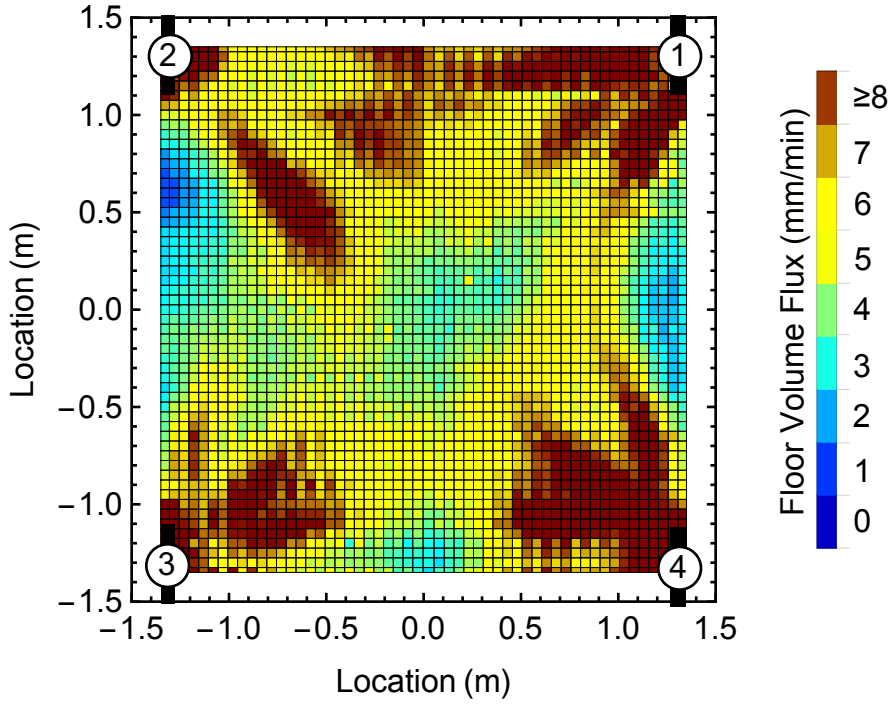

Figure 4.4: Volume flux of the four-sprinkler array was measured on a 0.05 m grid at 2970 locations on the floor, 1.5 m below the deflectors at a pressure of 1.35 bar. Sprinkler locations and orientations are identified in each corner.

4.3.3 Nonuniformity

Measurements of the quiescent spray dispersion identify the non-uniformity of the sprinkler spray. Radial patterns in the spray distribution can be identified and are similar to the geometry of the sprinkler deflector. Histograms of the volume flux distribution are shown in Fig. 4.5, showing a wide range of water distribution amounts. In the array configuration, the average density of 5.9 mm/min compares favorably with the overall value determined from the flow rate divided

by the protected area of 5.6 mm/min, or approximately 0.14 gpm/ft^2. This value also compares well to the design density for Ordinary Hazard (Group 1) occupancy conditions stipulated in the NFPA 13 density/area curve [3].

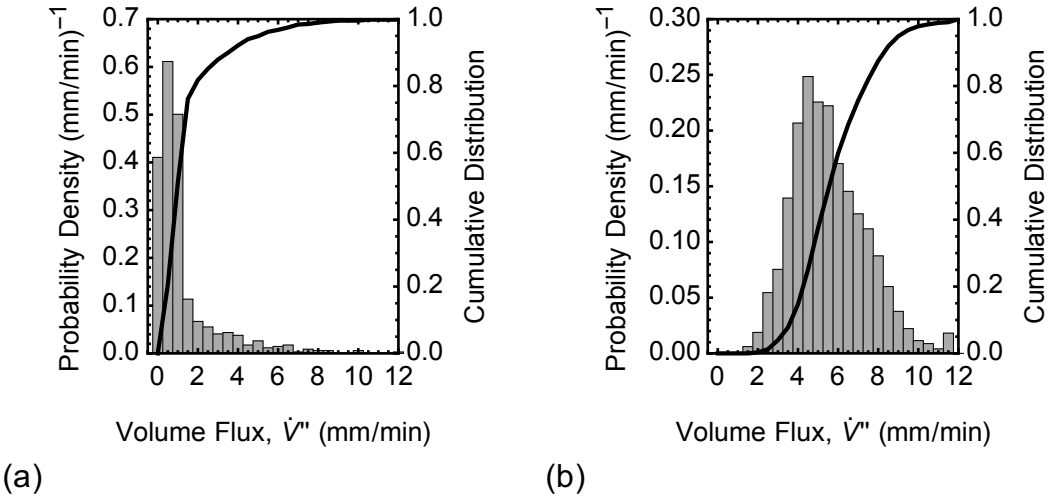

Figure 4.5: Histograms of the spray dispersion volume flux at a height of 1.5 m for (a) single sprinkler, and (b) sprinkler array configurations over the entire measurement area.

4.4 Resolution Analysis

4.4.1 Analysis Method

The slot/tine geometry of the typical fire sprinkler deflector is used on many of the sprinklers manufactured today. Both visual observation and detailed measurements of the initial spray with the 4S reveal a strong dependence on the deflector geometry in the spray pattern produced. Figure 4.6 shows a photograph of the D3 sprinkler deflector and the influence of deflector geometry on the initial sheet

Figure 4.6: The initial spray of the D3 sprinkler shows dependence on the deflector geometry. Sheet formation from the slots and tines of the deflector can be clearly seen.

formation; distinct sheets can be seen corresponding to the slots and tines. Measurements of the sprinkler array show strong spatial variations in far-field volume flux as well, corresponding to the variations seen in the initial spray. While the spatial distribution of volume flux is an important measurement for model validation, additional insight can be found from the results. Quantification of the spatial variations, as well as the spatial resolution required in measurements, is established with the following analysis.

Current industry standard approval tests, such as those published by Underwriters Laboratories and FM Approvals [7–9], recognize that non-uniformities exist within the spray and may negatively impact suppression performance. These tests are similar to the current procedure, however large 0.3 m (1 ft) sided square col-

lection bins cover the floor. For approval, a limited number of collection bins are permitted below a certain critical flux. However, these tests do not account for the resolution with which the flux measurements are evaluated. Error relative to the true spray pattern will be introduced if the measurement resolution is inadequate; as collection devices increase in area, the true variations in the spray pattern will be averaged out and the measurement may suggest that the spray is more uniform than it really is.

Resolution error was quantified by evaluating local differences in volume flux between the measured high-resolution data set and several low-resolution data sets constructed by averaging neighboring data points. These constructed data sets represent the spatial averaging that would occur if the collection cylinders were of a larger area. Figure 4.7 illustrates the procedure used for the development of low-resolution data sets. First the neighboring data points are binned together and averaged. This new reduced data set is interpolated to get a continuous function over the entire domain. Finally, the interpolated data set is evaluated at all of the original measurement locations to provide a data set with the same number of points as if the spatially averaged data set were collected with larger devices and interpolated between points.

The characteristic grid cell size, dx, describes the coarseness of the spatial grid. The error associated with the spatial averaging was determined by comparing the interpolated low-resolution data sets to the high-resolution reference case. The

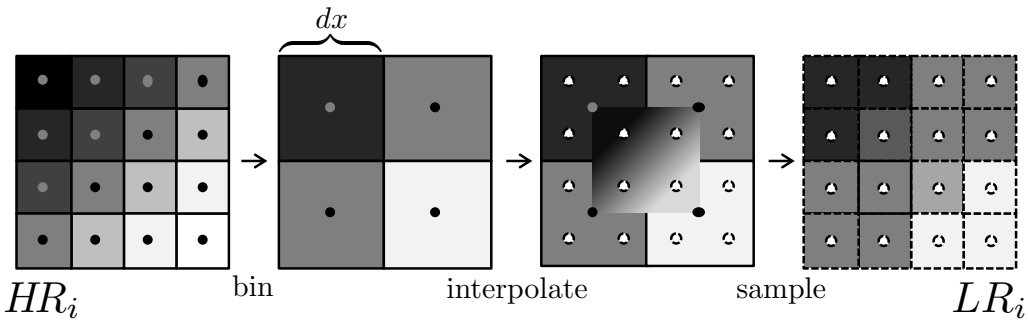

Figure 4.7: Neighboring grid points were averaged together to construct low-resolution data sets of the volume flux measurement. The low-resolution data was interpolated and then sampled at the original measurement locations to evaluate the errors introduced by insufficient spatial resolution.

error, ϵ, was calculated with a normalized standard deviation by

$$\epsilon = \left[\frac{\sum_{i=1}^{N} (HR_i - LR_i)^2}{\sum_{i=1}^{N} HR_i^2} \right]^{1/2} \tag{4.2}$$

where HR_i is the individual high-resolution measurement at each location i, and LR_i is the value of the low-resolution data at each measurement location, and N is the total number of measurement locations.

It is also recognized that a measurement repeatability error is present due to variables including positioning of the collection tubes, water supply pressure variations, temperature, room airflow, or other variations in spray pattern from day-to-day. Rigorous alignment and flow control procedures were implemented to reduce the effects of such variables. Alignment of the sprinklers was achieved by attaching a long metal rod to the sprinkler to check that the frame arms were installed according to Fig. 2.2 and Fig 4.4. The linear collection array was aligned with measured markings on the floor and walls, and verified using the line emitted

from a laser level directed along the length of the array.

Resolution is determined by the number of measured points in a length scale of interest, not explicitly by the spacing of the points. Therefore, resolution must be discussed relative to a characteristic length rather than in terms of absolute length. For a sprinkler spray, one characteristic length scale is the spray reach, R, or radial distance from the sprinkler head that encompasses all of the wetted area. The simplest estimation of spray reach, R, assumes the drops follow projectile behavior with no drag [13, 43],

$$R = (v_0)_r \left(\frac{2h}{g}\right)^{1/2} \tag{4.3}$$

where $(v_0)_r$ is the initial radial velocity, h is the height of the sprinkler from the floor, and g is gravitational acceleration. This model, while simple, may significantly over predict the spray reach by omitting drag and viscous influences. The initial radial velocity of drops is measured at velocities above 12 m/s, leading to reach predictions of more than 6 m. A more accurate calculation of the spray reach would be a numerical solution of the differential equation for droplet momentum, incorporating the effects of drag. The most accurate method, used in the current analysis, is the direct measurement of spray reach by measurement of the spray pattern and determination of the wetted area.

Of more specific concern to regulatory testing bodies is the accurate identification of the low-flux areas of the far-field spray [7]. These low-flux areas are associated with insufficient wetting, the primary suppression mode used in sprinkler protection. These 'dry' regions are identified through a threshold criterion applied

to the volume flux measurement, and can be quantified by simply counting the number of discrete bins with insufficient volume flux. However, if the collection bin area is too large, errors caused by the discretization will contaminate the evaluation of the low flux regions, suggesting that the sprinkler provides better coverage than it does. These errors can be reduced with better bin resolution or through a simple interpolation scheme.

4.4.2 Resolution Results

Resolution of the spatial dispersion measurements was evaluated using the method described in Sec. 4.4.1. Two metrics of resolution were explored, one looking at the total error associated with decreased resolution, and one looking at the error associated with resolving low flux areas as related to standard acceptance tests in the sprinkler industry.

Results of the binning method for simulating the spatial averaging effect of larger collection cylinders is shown in Fig. 4.8, showing how the decrease in resolution removes spatial variation compared to the true spray pattern measured at a 0.05 m grid resolution (Fig.4.8a and previously in Fig. 4.4). Each successive plot in Fig. 4.8 corresponds to a nominal doubling of the spatial averaging size. Through this binning, spray details are smoothed out, gradients are obscured, and the extremes of flux measurement are lost. This effect is evident in the 0.20 m bins in Fig. 4.8c, where only the large scale trends are resolved. At this resolution the extent of the low flux regions, identified as locations with volume flux less than one

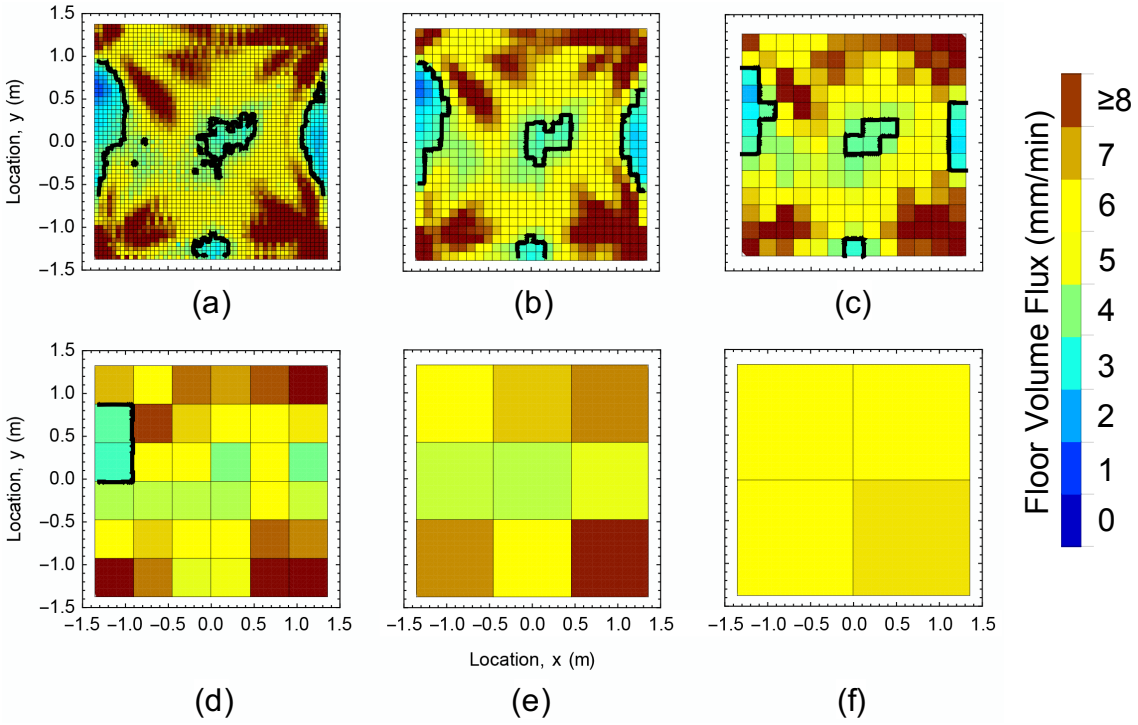

Figure 4.8: Spatial averaging of the data indicates the effect of collection tube size and resolution to capture the variations in the spray distribution. The contour lines outline the areas identified as dry spots for each of the collection bin sizes. Grid sizes shown are (a) 0.05 m, (b) 0.10 m, (c) 0.20 m, (d) 0.45 m, (e) 0.90 m, (f) 1.35 m.

standard deviation below the mean volume flux, are misrepresented. Minimal information about spatial gradients is present after bin size exceeds 0.20 m, and the results in Fig. 4.4f essentially only reports the overall mean flux with no spatial information.

Analysis of the binned and spatially averaged data provides insight to an adequate resolution for an accurate depiction of the spray dispersion. The solid line in Fig. 4.9 illustrates how the spatial averaging caused by increased collection cylinder size produces an error compared to the highest resolution measurement

at dx=0.05 m, defined by Eq. (4.2). Typical of many measurements, as the resolution increases repeatability is sacrificed. Several sources of repeatability error are present in the current measurement, including test-to-test variations in pressure control, water temperature, and collection tube positioning and leveling. As the resolution increases toward the high resolution measurement (left on the x-axis), the repeatability error increases, shown by the dashed line in Fig. 4.9. Repeatability error improves from 7.5% at the highest resolution to 1.5% for the lowest resolution. As the spatial detail of the measurement is reduced, local mean flux may be more accurately measured. A comparison between the two errors highlights the compromise between spatial resolution and measurement repeatability. Assuming the two error types are non-additive, the lowest total error occurs at the near-intersection of the lines at $dx/R = 0.04$, where the error from both resolution and repeatability are low and of comparable magnitude. To the left of this intersection point the measurement is of a high resolution but introduces increased repeatability error. To the right, at low resolutions, the improved repeatability comes at a significant increase in resolution errors, providing a good measurement of spatially filtered flux, which has limited utility. Further discussion of repeatability and resolution error on local volume flux measurements is provided after the following discussion of resolution errors on the integral measurement of low flux area.

Resolution errors in the integral measurement of the low flux areas become apparent from simply totaling the number of low flux bins. Areas outlined in Fig. 4.8 indicate low flux areas, in this case defined as areas with flux below 3.9 mm/min, cor-

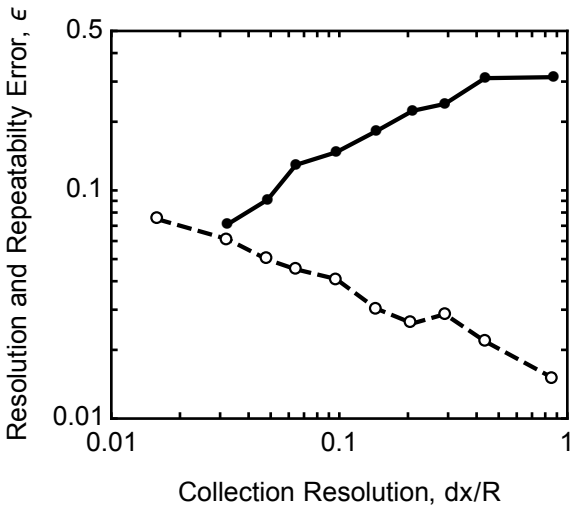

Figure 4.9: Two descriptions of error, ϵ, are plotted to show relative importance of resolution and repeatability at different grid sizes. The solid curve plots error due to resolution of the flux measurements comparing the coarse spatially averaged data to the high resolution base case measured at $dx/R = 0.016$. The dashed line indicates the repeatability of the measurement at each resolution.

responding to one standard deviation below the mean. Errors are introduced as the resolution decreases, and the accurate representation of these areas is diminished. The identification of low flux regions is less accurate at low resolutions because the bins are too large to resolve the variations in the spray pattern. This type of resolution is important in applications such as acceptance testing, where determination of the area supplied with a low flux is important for a passing mark. For each grid resolution, the corresponding fraction of the measurement area with volume flux below a set threshold was calculated, with the results plotted in Fig. 4.10. The solid symbols correspond to a low flux threshold 25% below the mean volume flux, while the open symbols correspond to a threshold one standard deviation (31%) below

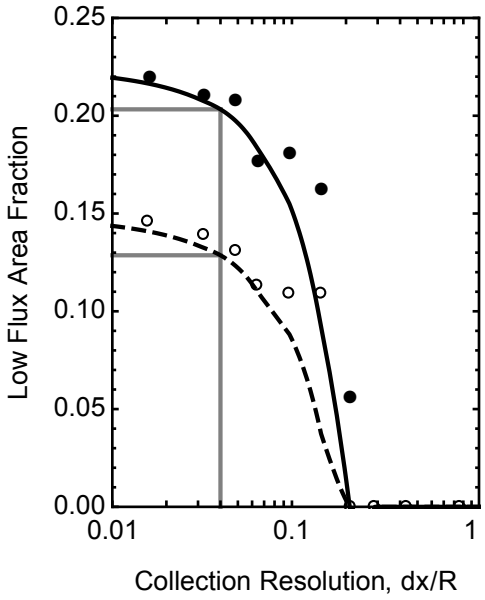

Figure 4.10: Low flux area calculation also suggests a resolution of dx/R=0.04 to resolve 90% of the low flux area.

the mean volume flux. Scatter in the trends indicates errors associated with the bin discretization, and contributes to additional error in resolving the low flux area. The smooth lines in Fig. 6 show how an interpolation of the binned volume flux alleviates discretization errors and improves the resolution of the low flux area. Figure 4.10 shows the resulting areas for two different thresholds, 25% of mean flux (solid) and 31% of mean flux (dashed). The gray lines indicate the measurement resolution resolving 90% of the low flux area determined using the high resolution measurement. In both cases, the critical resolution again lies at approximately $dx/R = 0.04$.

The results in Fig. 4.9 show that the resolution errors are comparable to the repeatability error and less than 10% at a resolution of $dx/R = 0.04$, or at least 25

measurements across the spray reach. At $dx/R = 0.04$, the repeatability is slightly improved from the best resolution ($dx/R = 0.015$), and the resolution error has not increased beyond 10%, indicating a tolerable increase in error with reduction in measurement resolution to this level. The corresponding binned volume flux measurements for $dx/R = 0.04$ are highlighted in Fig. 4.8b along with the outlined low flux area allowing visualization of spray pattern structures at this minimum suggested resolution. Additionally, Fig. 4.10 reveals that the low flux area can be resolved to within 90% of the best-resolved area at a resolution of $dx/R = 0.04$ indicated by the gray lines. The qualitative visual agreement, coupled with quantitative estimates of minimal error in local flux and integral low flux area measurement, suggest that the measurement resolution criterion of $dx/R < 0.04$ is suitable to accurately resolve volume flux variations. While the spray reach, R, is used here to provide a general framework for discussion of resolution, additional length scales such as deflector geometry may influence the gradients present in the dispersed spray. While these other length scales may be present, R provides a readily accessible engineering length scale a priori, and providing a reasonably general resolution criterion that does not require an iterative measurement of the dispersed spray to refine the spatial resolution.

4.5 Summary

A set of highly resolved volume flux measurements, from both a single sprinkler and from the four sprinkler array, were collected under quiescent conditions

to provide insight into the measurement of sprinkler spray pattern non-uniformities and to support CFD model validation. The measured volume flux variations of the initial spray (previously shown in Fig. 2.4) and the far-field dispersed spray near the floor correlate with sprinkler geometry details (e.g., frame arm positioning and slot/tine patterns). While measuring volume flux with large area collection bins reduces the time required to characterize the spray, such a method hides the gradients in far-field spray volume flux and obscures low-flux areas (i.e., dry regions) that may influence suppression efficacy. Analysis of the ultra-fine grid measurement data provides guidance for the measurement resolution required to resolve spray pattern details. Both qualitative visual inspection of the volume flux and a quantitative error assessment suggest that a resolution of $dx/R = 0.04$ is required, corresponding to at least 25 data points across the spray reach. At this resolution, local error in spray pattern is not dramatically influenced by the measurement grid size, comparisons of the integral low flux areas are favorable, and the resolution is compatible with current CFD capabilities.

Chapter 5: Spray/Plume Interactions

While dispersion of the spray under quiescent conditions is interesting and can provide insight to the potential of a sprinkler to deliver water to a given design area, the ultimate goal for suppression is delivery of water in fire conditions. Under these circumstances, the spray must compete with a buoyant upward plume generated by the fire and still be able to deliver water to the burning fuel surface. It is this interaction between the spray and the plume that is of interest for application to fire suppression with fire sprinklers. Modifications were made to the SAF to investigate these interactions including the addition of a forced-air jet providing a well-controlled momentum source to challenge the spray. Detailed measurements of the spray within the jet region were taken using a non-obtrusive optical shadowgraphy method.

Measurements of local spray-plume interactions within the plume region were taken in four flow conditions with the intent of providing model validation data, characteristics of the local spray field for further analysis, and physical insight into the spray-plume interactions. The flow conditions included cases with close and far sprinkler spacing, each with quiescent air and strong jet conditions. This chapter describes the experiments conducted related to spray-plume interactions, as well as the results and observations from spray measurements within the plume region.

5.1 Experimental Facility

5.1.1 Sprinkler Array

The existing sprinkler array facility, described in Sec. 4.1, was enhanced for the spray-plume interaction study. A forced-air jet was added to the facility, a substitute for a real fire plume, along with optical shadowgraph diagnostics to measure spray characteristics within the plume region. Additionally, multiple sprinkler spacing conditions were investigated to achieve different interaction conditions. Sprinkler spacing is defined as the distance from the sprinkler to the plume centerline, indicated by the distance Δr. The modified facility is shown in Fig. 5.1.

The plume generator, with orientation and ducting visible in Fig. 5.1, was located in the center of the array. This surrogate plume provided an upward jet of forced air to challenge the spray, simulating the upward flow from a fire source while providing repeatable boundary conditions for CFD input. The plume generator provides ambient temperature airflow at a velocity up to 4 m/s from a 1.1 kW, 240 V three-phase centrifugal blower controlled with a variable-frequency drive. Air was delivered from the blower via a 0.2 m diameter round flexible duct to the plume exit through a 90° elbow with 0.2 m×0.2 m square cross-section. Due to lab space restrictions, there was limited vertical space available to provide a lengthy flow conditioning section after the elbow. Care was taken to ensure the flow from the duct was uniform and did not show significant flow effects caused by the duct geometry. To provide a uniform exit profile, the airflow was conditioned by passing through six

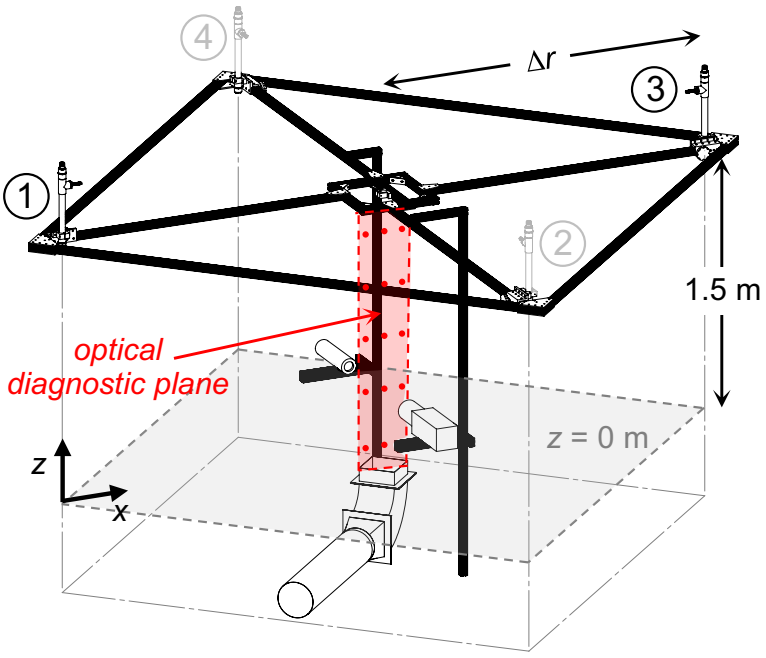

Figure 5.1: Drawing of the experimental facility showing the arrangement of the sprinklers, the plume, the shadowgraphy system, and the measurement region.

layers of 12 mm thick open-cell polyurethane foam with 20 pores per inch, supported by a perforated rigid aluminum plate (40% open area). Additional pressure drop was provided by a layer of stainless steel mesh (50×250 Mesh size) sandwiched between the foam. The duct exit was positioned 1.5 m below the sprinklers. A wire-screen cap prevented the foam from blowing out.

Due to the implementation of the shadowgraphy measurement, only two sprinklers could be operated at a time (#1 and #3), indicated by the darkened sprinkler numbers in Fig. 5.1 and previously highlighted in Fig. 1.1b. The reason for the two sprinkler approach is so that the drops pass perpendicularly through the camera

field-of-view, and also to prevent the LaVision system from physically blocking the spray along the path to the measurement location. For the experiments using the optical measurement, diagonal sprinklers #1 and #3 were operational, with the same conditions as the quiescent dispersion measurements operating at 1.38 bar.

5.1.2 Plume Velocity Characteristics

Care was taken to ensure the plume characteristics were well-controlled and repeatable for experiments and for model boundary conditions. A layer of fine mesh screening and several layers of open-cell foam were used to provide a pressure drop sufficient enough to remove major flow structures and imbalances due to the duct geometry near the exit. The plume exit velocity was characterized using a hot-wire anemometer positioned 2.5 cm above the opening of the plume. Figure 5.2 indicates the limited spatial variation in plume velocity measured at 16 locations on a 5 cm grid for two different fan speeds. For each flow velocity, the local maximum and minimum measured velocities were within 15% of the mean velocity.

An additional velocity profile measured across the center of the duct exit is shown in Fig. 5.3 with a mean of 3.7 m/s. Local velocity measurements fall within 12% of the mean velocity in this case, and show uniform top-hat characterization across the width of the plume.

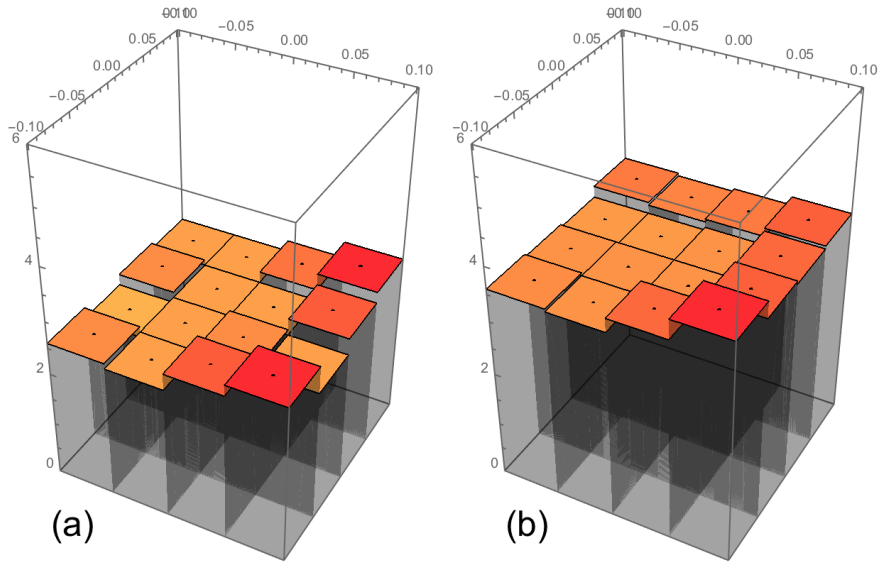

Figure 5.2: Air velocity was measured 2.5 cm above the outlet of the ducting at locations on a 5 cm grid to evaluate the spatial uniformity of the velocity profile. Shown are examples of the spatial velocity distribution at (a) 2.6 m/s (b) 3.7 m/s.

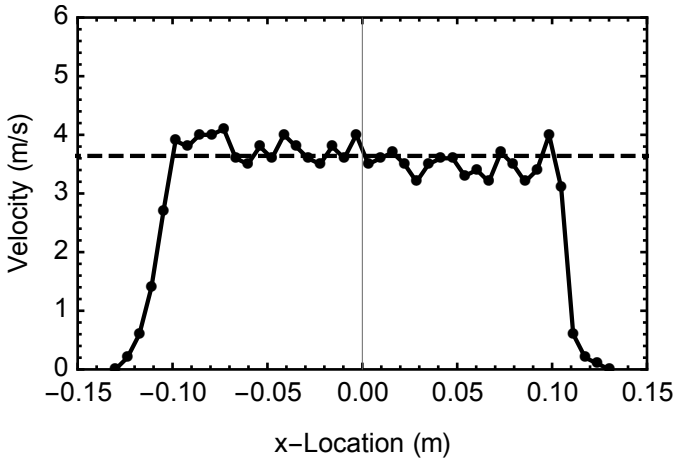

Figure 5.3: Measured uniform velocity profile across center of plume ($y = 0$ m) at 2.5 cm above opening exhibits variations within 12% of the mean velocity.

5.2 Measurements and Diagnostics

Characterization of the spray-plume interaction was done using two measurements, including mechanical measurement of volume flux to the plume surface and optical shadowgraph measurements within the plume region. Physical collection of water provided volume flux measurement at the surface of the plume for various plume velocity conditions, while the optical measurements provided drop sizes and velocities at locations throughout the plume region to map the interaction of the spray and plume. Further analysis of the shadowgraph measurements provides an additional measurement of volume flux that can be applied unobtrusively to locations within the spray. These measurements and diagnostics are discussed below.

5.2.1 Local Volume Flux

The successful suppression of a fire will depend largely on the volume flux delivered to the fuel surface, requiring penetration through the upward plume motion. Local volume flux delivered to the plume surface was directly measured by physical collection similar to the previous method in the quiescent case (Sec. 4.2). However, rather than the collection tube array, a small collection device was used to avoid disturbing the plume flow. A 42 mm diameter glass beaker was placed centrally on the surface of the plume generator, obstructing less than 5% of the plume area. Prior to exposure of the beaker to the spray, the plume air flow was set along with the sprinkler flow rate. After the water flow from the sprinklers reached a steady

state at 1.38 bar, the plume and collection beaker were uncovered and exposed to the spray for a period of time ranging from 1 to 5 minutes, adjusted according so the cup did not overflow. The water collected in the beaker was measured with an electronic mass balance, accurate to ±0.05 g. In this case, the volume flux is determined by

$$\dot{V}'' = m/(\rho_w A_o t) \tag{5.1}$$

where m is the mass of collected water, ρ_w is the density of water, A_o is the collection opening area, and t is the collection time.

5.2.2 Shadowgraphy

A LaVision shadowgraphy system, including a synchronized laser and camera, was used to conduct two-dimensional particle tracking velocimetry (PTV) measurements within the plume region, highlighted in Fig. 5.1. The system consists of a CCD camera aligned with a diffuser to provide a bright backlighting produced by a diffused laser pulse. The laser/camera system was mounted on a vertical traverse shown in Fig. 5.1, and could be positioned at different heights above the plume. Measurements were taken at 5 elevations (z = 0.10, 0.42, 0.74, 1.06, and 1.38 m) along the plume centerline as well as two additional profiles 0.1 m to the left and right of the centerline.

Shadowgraphy PTV measurements use a quick diffuse laser backlight flash, approximately 1 μs long, to freeze particles in an image. Two images are taken in rapid succession separated by a known time delay, 100 μs for these measurements. Indi-

vidual drops are located and matched between the two images using the LaVision's commercial software package, DaVis. Using a calibration from a scaling image, each drops diameter is determined, and a velocity vector is calculated from the change in position of the drop between the two images. Over a sufficiently large number of image pairs, statistics for drop size and velocity distributions can be calculated for any given location.

A LaVision Imager *pro X* CCD camera was used, fitted with a Nikon AF DC-Nikkor 105 mm $f/2$D lens. A Nikon PK-13 27.5 mm extension ring was necessary to obtain the proper focal distance to the plume centerline while filling the image frame with the diffuse laser backlight. The camera lens and 56 mm diameter laser diffuser were separated by 0.85 m, each located outside the plume influence. The resulting circular field of view was approximately 26 mm in diameter and the depth of field was approximately 25 mm, yielding a cylindrical measurement volume. With the current lens configuration and separation distance, the 4-megapixel camera provided resolution sufficient to measure drops as small as 0.08 mm in diameter.

The DaVis software package from LaVision was used to process the raw images and to calculate drop size and drop velocity. The software identifies drops by searching for light intensity gradients produced by the shadows of drops. Settings previously used for sprinkler drop measurements were used as a starting point for the drop identification algorithm thresholds [44]. The software searches for each identified drop in the second image of the pair to determine the velocity. A search window around each drop is used to bound the matching area to avoid incorrect

matches. Due to the velocity differences between small and large drops, as well as the multi-directional velocity field, multiple processing steps were required to optimize particle matching between the two images. Significant measurement noise was observed caused by incorrect particle matching and non-uniform light intensity near the edge of the images. To reduce measurement noise, processing was performed using three overlapping drop size ranges. Each image was processed three times, identifying drops with diameters, d, within the ranges $d < 0.4\,\text{mm}$, $d > 0.4\,\text{mm}$ and $0.25 < d < 0.55\,\text{mm}$. Any drops measured by multiple processing settings were identified and the duplicates removed from the combined dataset. Appendix C shows the reduction in measurement scatter achieved by the multiple processing ranges.

A sample image pair is shown in Fig. 5.4; the first image is on the left, while the second image is on the right. The yellow overlay on the second image shows the result of the three-pass processing, with the identified drops and displacement vectors. Additional filtering was required to ignore drops that were found outside a 20 mm diameter reduced field of view. These drops on the edge of the image introduced errors due to slight distortion or light intensity variations. The combination of field of view reduction and multiple processing ranges successfully reduced the scatter that was present in the initial measurements, and will be shown along with the measurement results in Sec. 5.3.

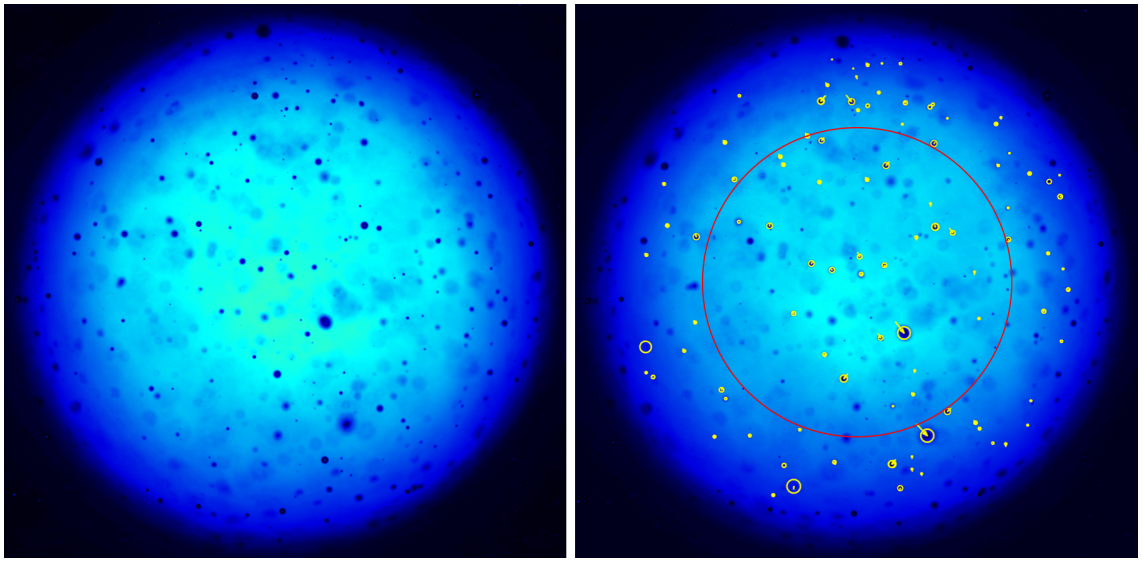

Figure 5.4: Sample image pair shows identified drops and their velocity vectors overlaid in yellow. The 20 mm diameter red circle indicates the reduced field-of-view implemented for noise reduction.

5.2.3 Optical Volume Flux

In addition to the physical collection of water to measure volume flux, a volume flux was also determined using the optical measurements. Optically measured volume flux, $\dot{V}_o''$, is derived from the direct measurements of drop size and velocity from the shadowgraphy results with the summation

$$\dot{V}_o'' = C\frac{\sum_{i=1}^{N_d}\left(\frac{\pi d_i^3}{6}v_{y,i}\right)}{V_O N_{im}} \tag{5.2}$$

where d is drop diameter, v_y is the downward velocity magnitude, V_O is the optical measurement volume, determined by the image depth-of-field and field-of-view, and N_{im} is the number of image frames recorded. The summation is performed over all drops moving in the downward direction. Upward moving drops are not included

in the calculation for downward volume flux. The shadowgraph technique does not successfully identify all drops within an image, but instead only captures some fraction of the overall spray. To calculate actual volume flux, a calibration factor, C, was determined from equating mechanical measurements of the volume flux delivered to the plume in each test configuration.

The uncalibrated optical flux ($C = 1$) can be corrected to provide a direct comparison to the mechanically measured flux using physical collection devices by accounting for the direction and location of drops within the image field of view. Drops from the shadowgraph images that have a velocity vector such that they would not land inside a physical collection cup were discarded, as they would artificially increase the measured flux. This correction has limited influence at the low elevations in the plume because of the more vertical drop velocity vectors, however at higher elevations, more drops are seen in the image that would not be collected within a physical cup. While the overall optical flux using all drops is a valid calculation, it is not a direct comparison to the mechanical measurements. Therefore, the correction was used for direct experimental comparison and calibration of the optically measured volume flux. Figure 5.5 shows the measured optical flux compared to the mechanical measurement of volume flux at the same location. Using the drop filtering based on trajectory to an imaginary collection cup, the two flux measurements yield a linear relationship, and the correction factor, $C = 1.18$ for the current configuration.

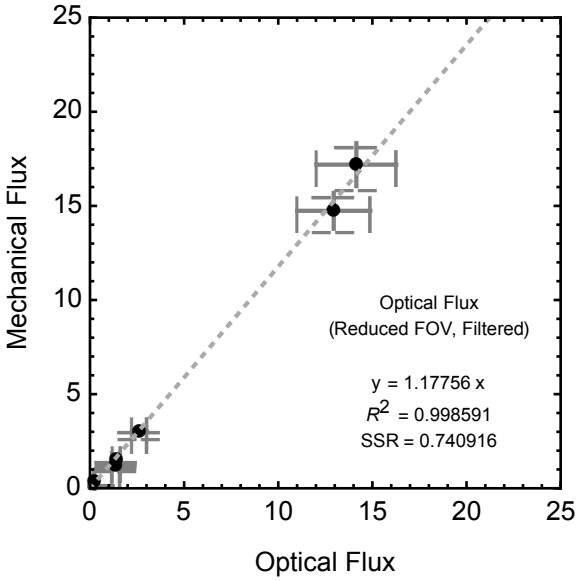

Figure 5.5: Optical flux calculated from the reduced field of view calibrated to physical flux measurements.

5.3 Shadowgraphy Results

Four spray conditions were measured for this study by combination of two sprinkler spacings and two air jet velocities. The sprinklers were positioned at one of two separation distances, Δr, measured from the sprinkler to the jet centerline—a close spacing case where $\Delta r = 0.65\,\mathrm{m}$, and a far spacing case where $\Delta r = 1.87\,\mathrm{m}$. For each spacing configuration, measurements were taken with a quiescent condition ($v_p = 0\,\mathrm{m/s}$) and with a strong air jet ($v_p = 3.7\,\mathrm{m/s}$).

The shadowgraph measurement directly determines drop sizes and velocity vectors. The scatter plots of measured drop velocity vector components shown in Fig. 5.6 provide an overview of the spray dynamics and spray-plume interactions

at 5 elevations along the jet centerline for the close spacing condition (sprinklers positioned a spacing of $\Delta r = 0.65\,\mathrm{m}$ from the jet centerline). The quiescent and $v_p = 3.7\,\mathrm{m/s}$ jet conditions are provided in Fig. 5.6a and Fig. 5.6b, respectively. The positive x-direction is along the diagonal towards sprinkler #3 and the negative x-direction towards sprinkler #1. Each data point represents the velocity of each individual drop measurement realization from the thousands at each location.

At all optical measurement locations the drop velocity scatter plot forms an inverted "V" shape. Each arm of the "V" corresponds to drops moving in distinct x-velocity directions, with approximately half of the drops moving to the left and half moving to the right due to the two different injection locations. In Fig. 5.6a, both arms can be seen to extend radially from the origin of the plot. Drops along these lines are all moving in the same direction, but with different velocity magnitudes according to their initially stochastic drop size characteristics. The influence of the location within the jet region is observed by the varying angles seen in the scatter plots. At higher elevations within the jet, drops are traveling mostly in the x-direction as gravity has not significantly altered the initial trajectory of the drops; lower down in the jet region, drops have traveled on a different trajectory with a significant vertical velocity component. In the quiescent case, all drops are moving downward, however this is not the case when the spray is opposed with the air jet. Figure 5.6b shows the case where the drops are driven by a strong plume with velocity $v_p = 3.7\,\mathrm{m/s}$. The drops in these cases show a shift in z-velocity for all drops, with the larger and faster drops being slowed only slightly but still falling

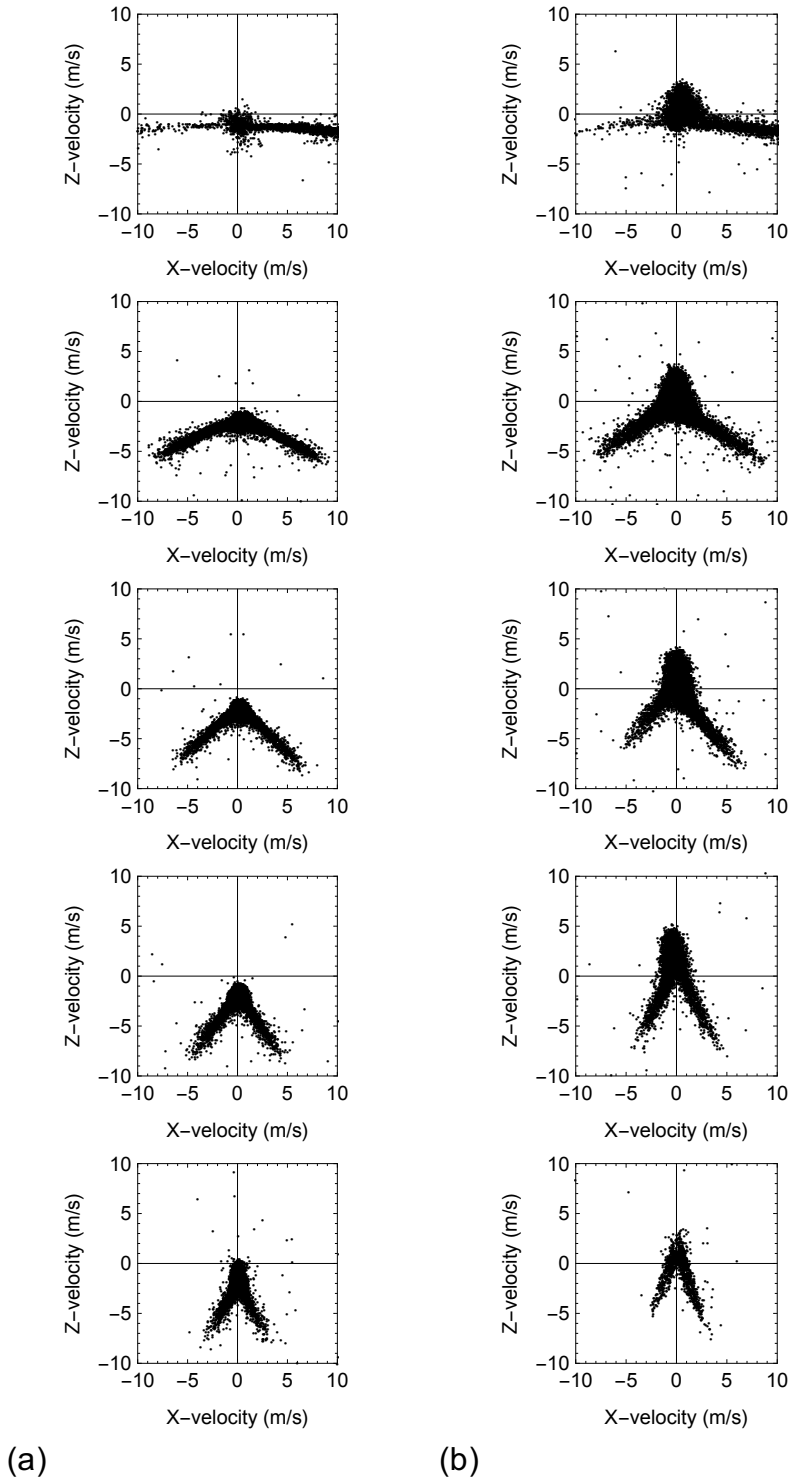

Figure 5.6: Plume-centerline drop velocity measurement results from the close spacing case ($\Delta r = 0.65\,\mathrm{m}$) at 5 elevations in the plume (0.10 m, 0.42 m, 0.74 m, 1.06 m, 1.38 m, bottom to top). (a) quiescent, (b) $v_p = 3.7\,\mathrm{m/s}$ plume.

downward, while the smaller drops are reversed and blown upwards by the plume as indicated by the data points above the x-axis. While the scatter is mostly symmetric over the y-axis, slight asymmetry is observed, and is caused by local spray variations that exist between the two sprinklers as observed in the initial spray measurements discussed in Ch. 2.

At injection, all drops are moving at an approximately uniform velocity, radially away from the sprinkler [26]. After injection and initial drop formation, differences in velocity magnitude can be attributed to varying drop size, where small drops are preferentially slowed by air drag to approach their terminal velocity. The length of the arms in Fig. 5.6 indicate differences in velocity, but does not explicitly highlight the relationship of drop size and velocity. Figure 5.7 illustrates the influence drag has on small drops, causing the spread of velocity magnitude correlation, in the quiescent condition, for the two spacing configurations. The red line indicates the calculated terminal velocity, v_t, for a given drop diameter determined by iteratively solving the steady-state force balance on a drop, resulting in the relation

$$v_t = \left(\frac{4\rho_d dg}{3\rho_a C_D} \right)^{1/2} \tag{5.3}$$

where ρ_d is the drop density, ρ_a is the air density, d is the drop diameter, g is the gravitational acceleration, and C_D is the Re dependent drag coefficient defined with the correlation

$$C_D = \begin{cases} \frac{24}{Re}\left(1 + \frac{Re^{2/3}}{6}\right), & Re < 1000 \\ 0.424, & Re \geq 1000 \end{cases} \tag{5.4}$$

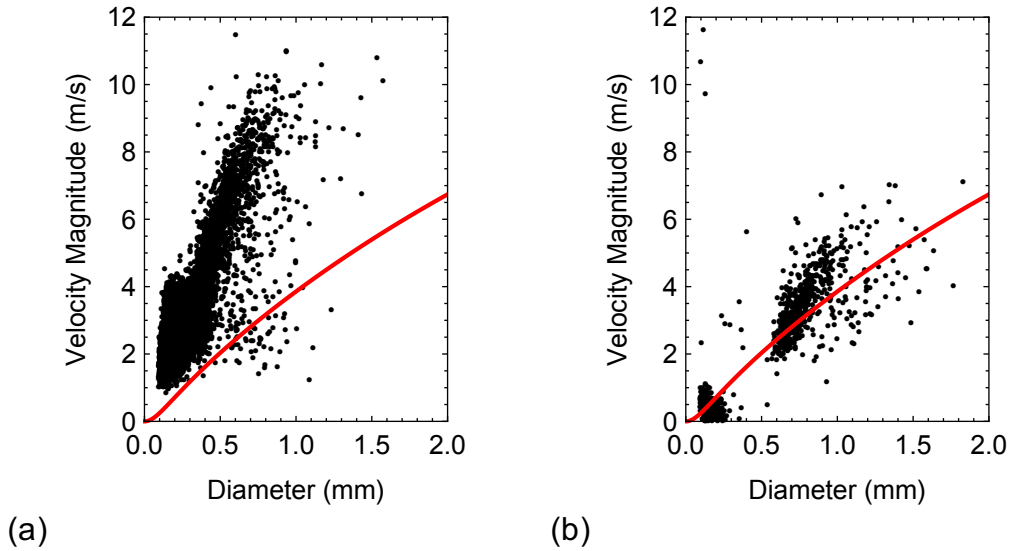

Figure 5.7: Drop diameter vs. velocity magnitude correlation in the quiescent case at $z = 0.74\,\mathrm{m}$. (a) close spacing ($\Delta r = 0.65\,\mathrm{m}$), (b) far spacing ($\Delta r = 1.87\,\mathrm{m}$).

In the far spacing case, drops have had sufficient travel time and distance to slow to near their terminal velocity (Fig. 5.7b) compared to the close spacing case where drops are traveling significantly faster (Fig. 5.7a).

In addition to drop velocity correlations, an additional observation in Fig. 5.7 suggests a difference in drop size distributions measured in the different spacing conditions. The near spacing condition results in a more complete range of drop sizes, while the close spacing shows fewer overall drop measurements, and very few drops with diameters less than 0.5 mm. In the far spacing, smaller drops influenced by drag have already slowed in the radial direction of travel and do not reach the plume centerline measurement location. Figure 5.8 shows the drop size distribution cumulative volume fractions (CVF) at each measurement location on the plume

centerline for the quiescent no plume condition (left) and the plume condition with $v_p = 3.7\,\mathrm{m/s}$ (right). Each plot contains the CVF for the close spacing (blue) and far spacing (orange) configurations. The most noticeable result of the CVF comparison is the rightward shift of drop distribution in the far spacing case compared to the close spacing. Comparing the curves in the left column to the right (with the plume), a less noticeable shift is observed where all of the smaller drops are driven higher in the plume region. Each figure also highlights the number of drops measured in each location.

The resulting changes in drop distribution can be compared using a normalized volume fraction to show the shift in drop size and the re-distribution of the spray volume within the plume region. A modified volume fraction is used to describe drop size weighting of the local spray with respect to that at the base under quiescent conditions for each spacing configuration. The normalized volume fraction, VF^*, is described by the equation

$$VF^*(z,d) = \frac{\dot{V}''_{CL}(z,d)}{\int \left(\dot{V}''_{CL}(z_0,d)\right)_Q dd} \tag{5.5}$$

where $\dot{V}''_{CL}(z,d)$ is the volume flux distribution as a function of drop size with diameter d at a specific elevation z in the plume region. The denominator $\int \left(\dot{V}''_{CL}(z_0,d)\right)_Q dd$ is the total volume flux measured in the quiescent condition at the base of the plume at $z_0 = 0\,\mathrm{m}$ integrated over all drop sizes. This normalization reveals how the spray's local drop size distribution and overall volume flux may change (reflected in a non-unity $\int VF^*(z,d)dd$) when challenged by a plume.

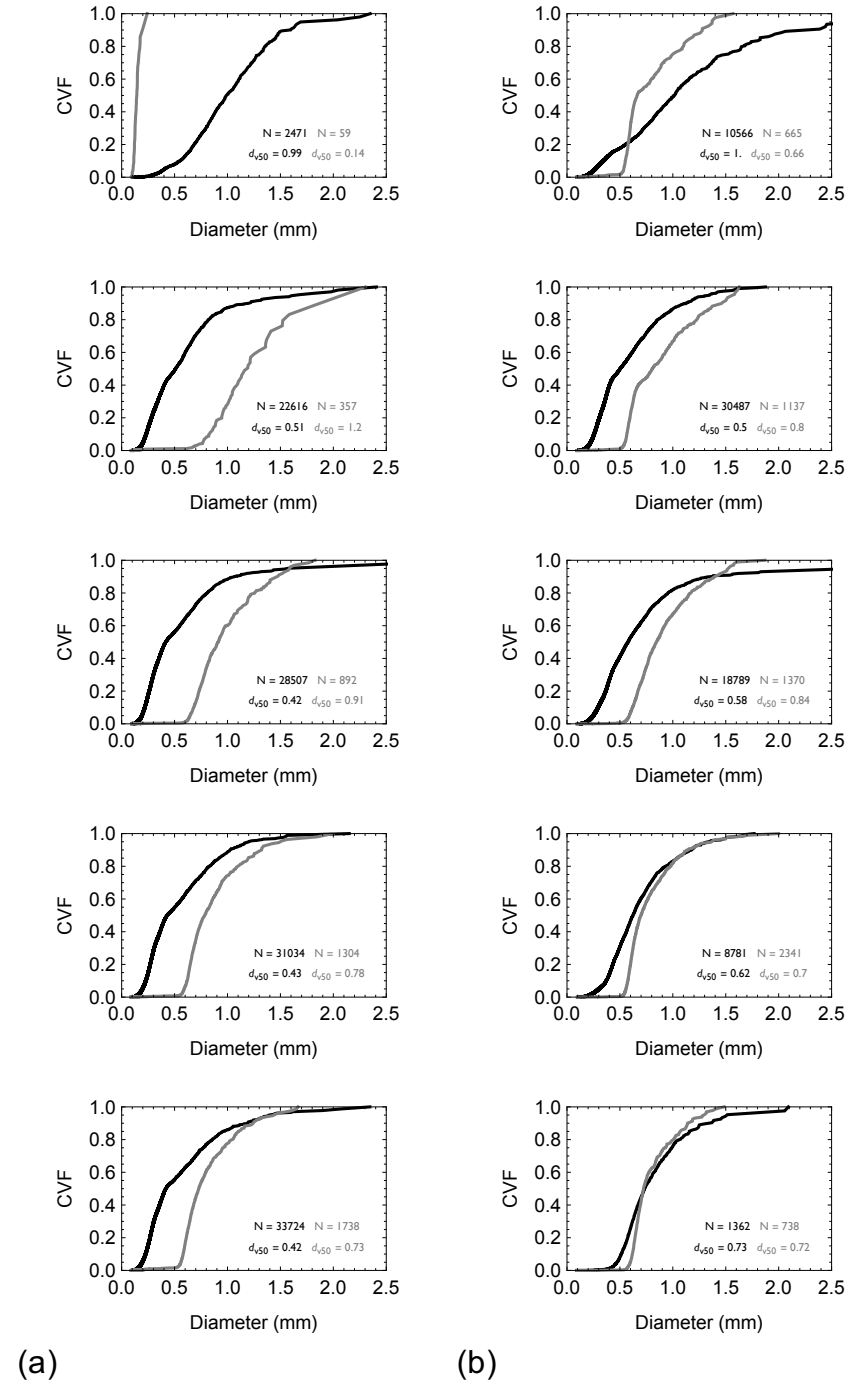

Figure 5.8: Drop size distribution at 5 elevations within the plume at 5 elevations (0.10 m, 0.42 m, 0.74 m, 1.06 m, 1.38 m, bottom to top). (a) quiescent, (b) 3.7 m/s plume. (black: near, gray: far).

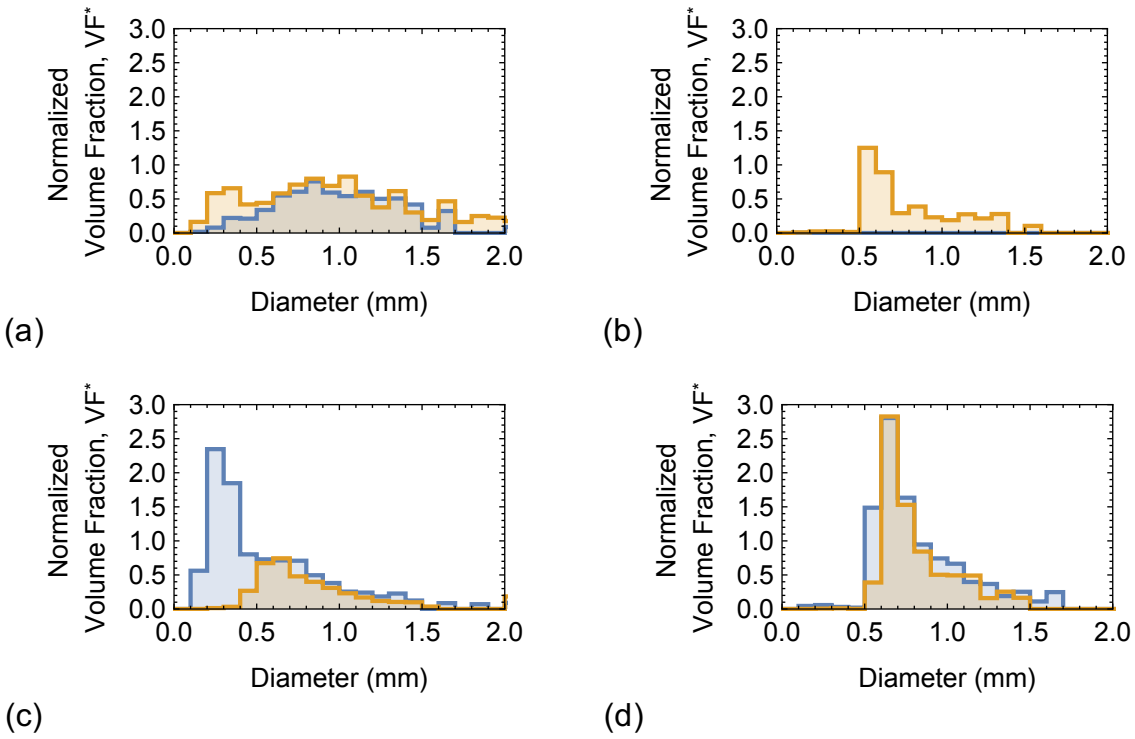

Figure 5.9: Normalized volume fraction probability density functions comparing quiescent flux (blue) to flux delivered with a strong plume (orange).
(a) close spacing, $z = 1.38\,\mathrm{m}$, (b) far spacing, $z = 1.38\,\mathrm{m}$,
(c) close spacing, $z = 0.10\,\mathrm{m}$, (d) far spacing, $z = 0.10\,\mathrm{m}$.

Figure 5.9 shows VF^* distributions at two heights for the close and far sprinkler spacing. In each figure, quiescent and strong plume conditions are compared.

The first observations can be made in the close spacing cases on the left of Figure 5.9 (a and c). Focusing on the quiescent condition drop size distribution indicated with the blue curves, it is clear that there are significantly more small drops at the base of the jet (Fig. 5.9c) compared to those at higher elevations (Fig. 5.9a). When the spray is subject to the air jet, these small drops are rejected from the

low elevations, as seen by comparing the orange curve in Fig. 5.9c (representing the jet condition distribution) with the blue curve (representing the quiescent condition distribution). Essentially all small drops are rejected, as there is no volume fraction of drops less than 0.5 mm. At the higher elevation, however, the volume fraction of small drops has increased because the small drops are carried by (and in the direction of) the jet flow, also reflected in Fig. 5.6b. Small drops having terminal velocity less than the velocity of the jet will be turned away and cannot penetrate to the jet surface. While these drops will not contribute to direct fuel surface cooling, they may still contribute to ultimate suppression or mitigation through ceiling jet cooling or redistribution to other surfaces, preventing fire spread, or improving tenability within a compartment. In the far spacing case, on the right of Fig. 5.9 (b and d), there is essentially no volume at the higher elevation location in the quiescent case (Fig. 5.9b) because the measurement location is above the umbrella-shaped sprinkler spray. However, in the jet challenge case also depicted in Fig. 5.9b, the volume is non-negligible (orange curve) where a significant amount of spray has been redirected upwards. The larger drops capable of reaching the more remote jet centerline in the far spacing are also more capable of penetrating the jet (being driven by their own momentum and less influenced by jet drag). This is reflected by the drop distribution in the far spacing case remaining relatively unchanged compared to the quiescent case for that condition.

Comparison of the drop distributions in the quiescent case (blue curves) between the close and far sprinkler spacings (left and right of Fig. 5.9) highlights the

natural drop filtering due to drag influence. A very small volume is carried to the plume centerline by small drops for the far spacing, while at the close spacing nearly 50% of the volume fraction is delivered in drops smaller than 0.5 mm in diameter.

This drop size filtering due to drag effects is also demonstrated in Fig. 5.10 which depicts velocity vectors for characteristic drop sizes (determined by volume fraction) at a select location (plume centerline at $z = 0.42\,\mathrm{m}$) in the close spacing configuration. This depiction identifies drop size dependent behavior of velocity measurements presented in Fig. 5.6. Each vector represents an equal fraction of volume flux from each sprinkler according to increasing discrete drop size bins (d_{v05}–d_{v95}) as described in the legend. The length of each vector corresponds to the mean velocity of each drop size class (and corresponding equally weighted flow fraction). Vectors for each sprinkler can be clearly identified by their respective x-directions and correspond to 100% of the volume flux from each individual sprinkler. Figure 5.10a shows the quiescent case where all vectors are directed downward. The drag influence of the smaller drops is shown by the shorter velocity vectors and the orientation at an angle closer to vertical. Large drops maintain a larger velocity magnitude and preserve more of their initial x-velocity outward from the sprinkler. Figure 5.10b shows the same measurement but in the $v_p = 3.7\,\mathrm{m/s}$ case. Small drops are influenced by the jet and have been re-directed upwards, while intermediate drop vectors have been turned from their quiescent direction (maintaining x-velocity, with significant reduction in z-velocity) but have not been completely overcome by the jet. Large drops are slowed to a lesser extent, indicated by the warmer colored

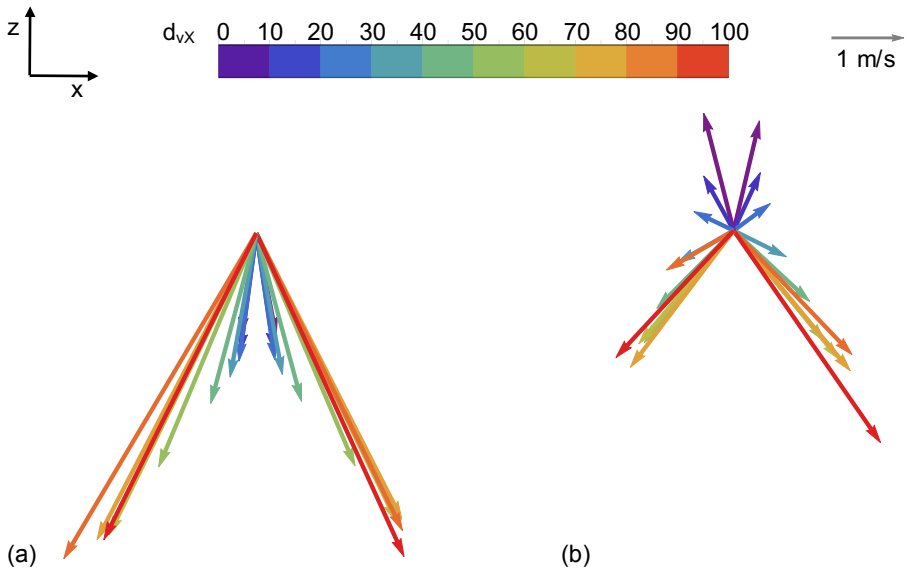

Figure 5.10: Volume flux vectors representing equal volume fractions for the close spacing at $z = 0.42\,\mathrm{m}$ on plume centerline. (a) $v_p = 0\,\mathrm{m/s}$, (b) $v_p = 3.7\,\mathrm{m/s}$.

vectors (i.e. red) that maintain more of their quiescent direction.

The downward volume flux of the spray, particularly when opposed by a plume, is a key quantity for predicting fire suppression. The spray must deliver enough volume to extract sufficient heat from the fuel to suppress the fire. This volume delivery is further complicated when the spray must penetrate through an opposing plume to the base of the plume surface. Measurements of volume flux were calculated using the optical shadowgraph images at 5 elevations within the plume region. The results are shown in Fig. 5.11 for each spacing configuration in the quiescent case and the plume case. The shaded region indicates a flux $\pm 15\%$ from the optically measured value. In each configuration, the optical flux is also compared to a mechanically

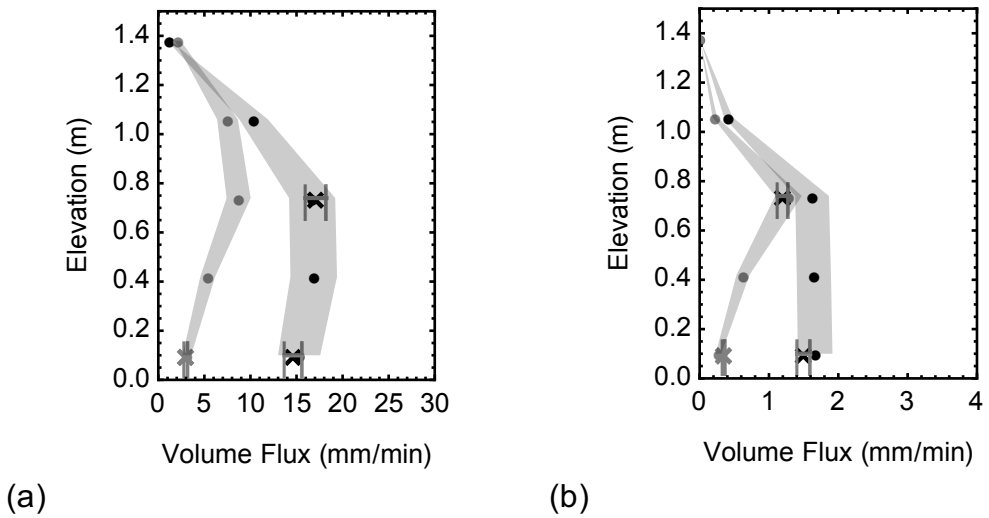

Figure 5.11: Volume flux was measured optically along the plume centerline at 5 elevations in the quiescent (black) and plume (gray) case. The × symbols represent physically collected volume flux data points. (a) near spacing, (b) far spacing.

measured flux, indicated by the × symbols. The mechanically measured flux results provided very repeatable results, with measurement errors within ±6%, as indicated by the error bars.

5.4 Summary

Spray-plume interactions and the ability of the spray to penetrate through the plume govern the suppression effectiveness of fire sprinklers. Detailed measurements of spray-plume interactions with multiple sprinkler and forced-air jet configurations were performed using unobtrusive optical shadowgraphy. Measurements of drop size, velocity, and volume flux show along vertical profiles in the plume region reveal complexities associated with drop transport under quiescent conditions, which

are only enhanced further when the spray interaction with an opposing jet is captured. The non-uniformity of sprinkler sprays means that small changes in location can lead to significant changes in spray characteristics such as drop size distribution and volume flux, which may have direct influence on penetration and suppression performance. Additionally, the measurements provide data for CFD model validation along intermediate locations of spray dispersion computations.

Chapter 6: Plume Penetration

The predominant suppression mechanism of sprinkler sprays is the surface cooling of the burning solid fuel. This is achieved when drops are able to penetrate through the upward motion generated by the fire plume. Current protection design methods use a general quiescent design density (overall average volume flux) delivered to a design area to determine system flow requirements with no direct consideration given to the ability of the spray produced to penetrate to the surface. Understanding the phenomena and physical scaling behind penetration can aid in protection design evaluation and in potential technological development in sprinklers. While penetration will be correlated with suppression effectiveness, there are additional factors to consider—100% penetration to the surface will not guarantee suppression if the delivered volume flux is below the critical value required for suppression. Additional suppression phenomena, such as gas cooling through drop evaporation in a fire compartment, radiation attenuation, and surrounding surface wetting are not accounted for in the penetration ratio metric. However, these effects are beyond the scope of this analysis, and will work to improve the suppression effectiveness of a particular sprinkler if direct penetration to the burning surface can be achieved.

This chapter presents measurements of penetration and a scaling analysis to predict the degree of penetration depending on local spray properties. Penetration of the spray to the surface of the plume was determined by measuring volume flux from the SAF as a function of variable plume velocity. A majority of the measurements were done with the two sprinkler configuration which provided local spray details. Observation of suppression events and physical intuition suggests there are two contributing mechanisms that may determine penetration effectiveness of a spray [6, 29]. Analysis of the trends observed from the current penetration measurements considers two regimes of spray-plume interaction with different mechanisms of penetration to identify scaling laws to predict the penetration. First, individual drops are considered independently as they interact with the plume, and second, consideration is given to the drag force interactions induced by the spray onto the plume by the collection of all drops within the spray. The measurements of local spray properties from the quiescent condition (no plume) measured in Ch. 5 including drop size, velocity, and volume flux, were used to inform the scaling laws.

A scaling analysis in terms of quiescent spray characteristics is desirable as prediction and measurement of such values is easier compared to the more complex condition including spray-plume interactions. The quiescent spray condition presents the total potential the spray has to penetrate or influence the plume dynamics. Recent advancements in model development show accurate prediction of local spray characteristics [45]. Even simplified models, given the accurate initial spray input (presented in Ch. 2), can accurately predict important local spray char-

acteristics in quiescent conditions. Development of scaling laws for prediction of penetration performance of a given sprinkler would provide an engineering analysis to determine protection system effectiveness.

Experiments measuring spray penetration to the plume surface were attempted such that the two penetration mechanisms had different relative contributions (i.e. dominated by individual drops or total drag force work applied to the plume). Table 6.1 highlights the general test conditions that were explored to measure the different penetration regimes. Four different test conditions were achieved by leveraging two different sprinkler spacing conditions (close and far spacings presented in Ch. 5) and either two or four sprinklers operating in the array. In general, due to drag filtering, the far spacing case provided larger drops with higher terminal velocities, while the near spacing provided smaller drops. The number of sprinklers was used to control the drag influence of the spray through variation of the volume flux. The plume velocity was varied over a range of velocities in each of the test configurations. The penetration regimes are described in Sec. 6.2.

Table 6.1: Test matrix of desired general spray-plume interaction conditions and required facility configuration.

Penetration Regime		Test Configuration	
u_p/v_t	W/KE	Spacing	# Sprinklers
Low	Low	Far	2
Low	High	Far	4
High	Low	Close	2
High	High	Close	4

6.1 Plume Penetration Measurement Results

Measurements of volume flux delivered to the local plume surface were taken as described in Sec. 5.2.1, using a small collection cup at the plume surface, under the influence of a range of plume strengths to determine the penetration of the spray through the plume. The degree of successful penetration can be quantified by a ratio of measured volume flux in the quiescent no plume case to the actual delivered flux when the plume is present,

$$PR = \frac{\dot{V}''}{\dot{V}''_Q} \tag{6.1}$$

indicating the fraction of water delivered to the target location relative to the maximum possible amount through a quiescent environment.

Measurements of plume penetration calculated according to Eq. (6.1) from the two-sprinkler configuration are plotted in Fig. 6.1 as a function of the opposing air jet strength. As the jet velocity increases the penetration ratio is reduced. This result was expected when the jet velocity creates a condition where drops are no longer able to penetrate to the plume surface and are turned around and redirected by the stronger air jet. It is notable that the critical plume velocity for penetration occurs at different values depending on the configuration and whether the sprinklers are located close or far from the jet centerline. The vertical dashed lines indicate a critical velocity for 50% penetration, and aligns closely to a critical point where penetration ratio transitions rapidly. At first glance, results indicate that the spray is better at penetrating if it is spaced far from the centerline. One may assuming

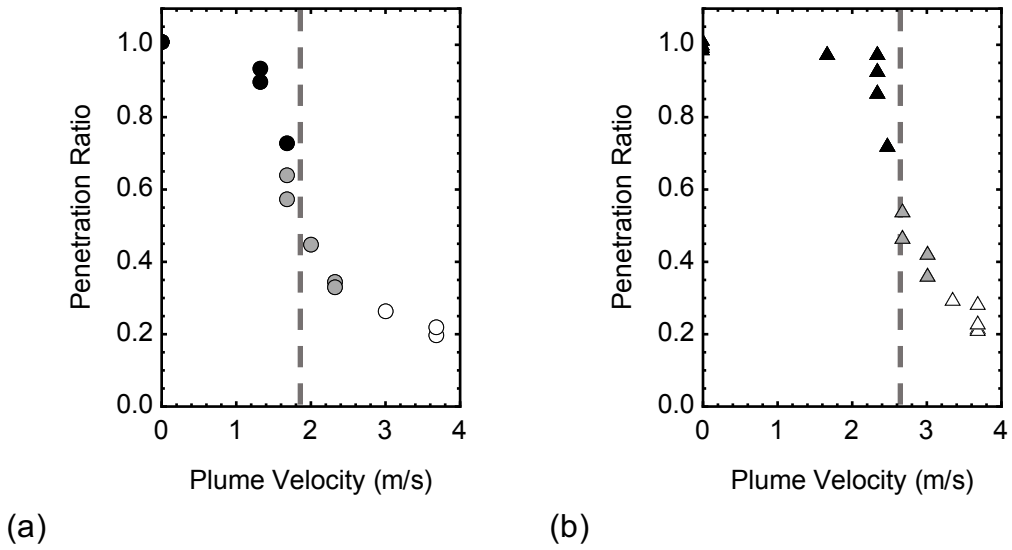

Figure 6.1: Penetration ratio measurements for the two sprinkler configuration with (a) close and (b) far spacing. The vertical dashed line represents the jet velocity corresponding to a 50% penetration ratio and a rapid transition in penetration ratio.

that the closer spacing has a more dense spray with higher spray velocities and stronger momentum, but this result is counterintuitive. A look at the scaling for plume penetration is presented in the following sections to identify the behavior of the spray-plume interactions and to provide an engineering assessment of a given spray condition, identifying the contributing factors for plume penetration.

6.2 Penetration Regime Introduction

In the first regime, spray penetration depends on the ability of individual drops to maintain sufficient momentum on their own to avoid being turned away from the competing gas flow [16]. This suggests that smaller drops, being more susceptible

to individual drag interactions, will be unable to penetrate to the fuel surface. In the first regime, drops are considered individually to determine their penetration ability. In this case it is assumed that the drops are relatively large and the spray is relatively sparse so there is not a significant impact on the plume dynamics, as indicated by the cartoon in Fig. 6.2a, where the plume velocity is unchanged by the spray. This is considered the individual action regime, conventionally termed as one-way coupled to the gas phase, where the spray is dominated by individual drag interactions. In this regime, a critical scaling factor using the drop terminal velocity is explored, where only drops with supercritical terminal velocities penetrate the plume. Smaller drops may still be able to penetrate depending on the specific velocity vector and plume entry location, but are largely redirected by the opposing gas flow such that they do not land at the targeted location and do not significantly contribute to suppression.

However, sprays with drops that are relatively small compared to the plume velocity and the drag induced by the gas flow are often used with successful suppression, suggesting there is a second regime of spray-plume interaction. Examples of such events include water mist spray nozzles or the suppression of large fires with significant buoyancy induced flows, often a challenge in storage applications. In the second regime, penetration is influenced by the spray as an ensemble, where a significant drop number density and/or velocity causes the plume dynamics to change [30,31], allowing drops that would otherwise be redirected if they were penetrating alone to penetrate the plume and reach the surface [6,24]. This is represented

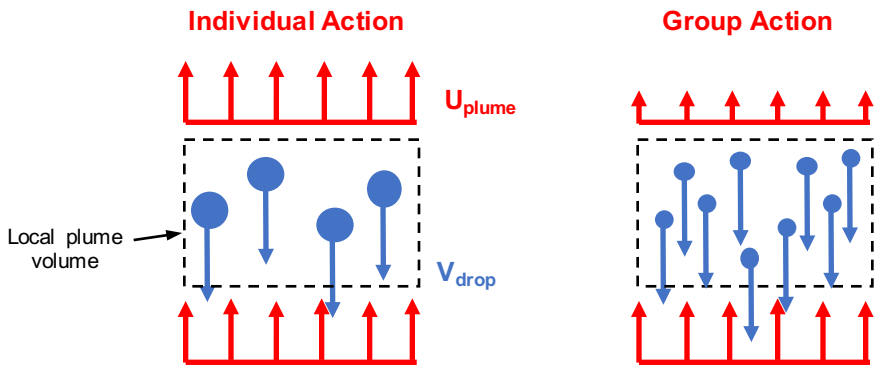

Figure 6.2: Two regimes of penetration dynamics are considered; individual action and group action regimes. The interaction regime is characterized by the influence the drops have on the dynamics of the gas-phase plume.

in Fig. 6.2b by the increased number of smaller drops, and a change in the plume velocity induced by the drag force of the spray as a group. In this regime, it is proposed that the accumulated work effects of the spray, due to the drag imparted on the plume, relative to the characteristic kinetic energy of the plume is a critical penetration scaling parameter. An analytical framework to identify scaling parameters for plume penetration of a certain spray is detailed in the following sections, considering the two behaviors.

6.3 Individual Action Regime

6.3.1 Terminal Velocity Scaling Analysis

At the most basic level of penetration, a drop must maintain a net downward velocity throughout its trajectory. In the individual action regime, drops are consid-

ered independent of one another and with one-way coupling to the gas phase through drag interactions, meaning the gas velocity is unchanged. In the limiting case, all drops will reach a terminal velocity as they are influenced by drag. If the terminal velocity is sufficiently large to maintain a net downward velocity in the presence of the plume motion, it is possible for the drop to penetrate the plume. Therefore, a critical scale for an individual drop to penetrate an opposing plume may be the drop's terminal velocity. Drops that have subcritical terminal velocities cannot be guaranteed to penetrate. Unless trajectory conditions are favorable, the subcritical drop will be redirected away from the target, and there will be no suppression from these smaller drops.

Penetration analysis in this regime considers the forces acting on a drop falling through the air. A free body diagram is shown in Fig. 6.3 including the gravitational body force, $\mathbf{F_G}$, acting downward and the drag force, $\mathbf{F_D}$, acting opposite the relative velocity vector shown by the kinetic diagram. If the drag force is not strong enough to reverse the direction of motion, the drop is unstoppable and is therefore considered to penetrate the plume. The critical force condition is determined using the force balance between the gravitational and drag forces. Beginning with Newton's second law,

$$\Sigma\mathbf{F} = m\mathbf{a} = m\frac{d\mathbf{v}}{dt} \tag{6.2}$$

and substituting in the equations for drag and gravitational forces

$$m\frac{d\mathbf{v}}{dt} = \frac{1}{2}C_D\rho_a A_d|\mathbf{u}-\mathbf{v}|(\mathbf{u}-\mathbf{v}) + m\mathbf{g} \tag{6.3}$$

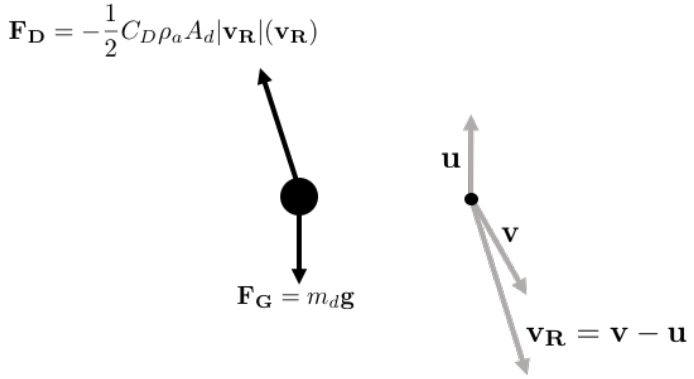

Figure 6.3: Free-body and kinetic diagrams of a single drop traveling through air includes gravitational body force and a drag force.

where m is the mass of the drop, C_D is the drag coefficient, ρ_a is the air density, A_d is the frontal area of the drop, $\mathbf{u}$ is the air velocity vector, $\mathbf{v}$ is the drop velocity vector, and $\mathbf{g}$ is the gravitational acceleration vector.

For the remainder of the single drop analysis only velocity in the vertical z-direction is considered, which is a reasonable simplification when discussing both terminal velocity and vertical plume penetration. In this case, the falling drop motion directly opposes the upward air velocity. To determine the critical drag force that a drop is able to resist without stopping or reversing direction, the vertical component of Eq. (6.3) is set to a zero acceleration and after simplification, the relationship of the velocity difference is found to be

$$u_z - v_z = \left(\frac{4 \rho_d d g}{3 \rho_a C_D} \right)^{1/2} \tag{6.4}$$

where u_z is the magnitude of the upward plume velocity and v_z is the magnitude of the downward drop velocity. Recall the equivalent Eq. (5.3), which now shows

that the terminal velocity is the relative velocity between the drop and the air, $v_{term} = u_z - v_z$. For penetration the drop must maintain a net downward velocity, $v_z > 0$. This critical condition is found when $v_{term} > u_z$. If the plume velocity is less than the opposing drop terminal velocity, it is not possible for the drop to be stopped or reversed, and the drop cannot be rejected from the plume.

The spray can be considered in terms of individual drop penetration through a measured (or predicted) drop size distribution. The cumulative volume fraction, CVF(d), quantifies the fraction of the measured spray that is contained in drop sizes smaller than a given diameter. The complement of this value, $1 - \text{CVF}(d)$, determines the fraction of the spray volume that is greater than a given size, or corresponding critical terminal velocity. Thus, it is proposed that the penetration can be scaled according to the equation

$$PR(u_z) \sim [1 - \text{CVF}(v_{term} = u_z)] \tag{6.5}$$

where the CVF(v_{term}) is the CVF in terms of a local drop terminal velocity distribution, evaluated at the critical terminal velocity equal to the competing plume velocity.

6.3.2 Terminal Velocity Scaling Results and Discussion

Penetration through the plume will depend on local spray characteristics. Non-uniformities stemming from the formation of the spray will influence the specific characteristics of the interaction depending on the target location relative to the

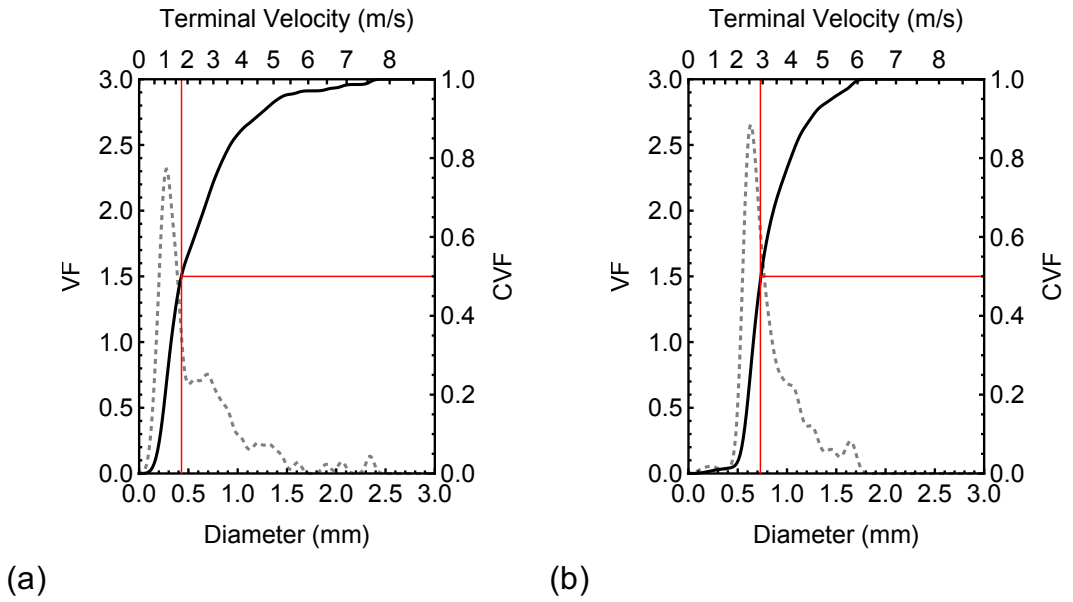

Figure 6.4: Local drop size distributions of the (a) close spacing and (b) far spacing configuration, along with corresponding terminal velocity (upper axis) measured at $z = 0.1$ m. Lines represent the PDF (dashed), CVF (solid), and d_{v50} (red).

sprinkler. As identified in the proposed scaling, the local drop size distribution is important for the terminal velocity analysis. Drop size distributions were calculated for each of the sprinkler spacing configurations in the quiescent no plume condition, measured at a location 10 cm above the base of the plume, and are plotted in Fig. 6.4, characterizing the drops that were delivered to the plume target location. Drops higher in the plume region pass through the plume, but are not on a trajectory to reach the target at the plume.

The probability density of each drop size is plotted by the gray dashed line (values read to left), while the cumulative volume fraction is plotted by the black

line (values read to right), indicating the fraction of the spray volume with drop diameters less than a given size. The characteristic volume median drop size, d_{v50}, is identified by the red leading lines where the CVF reaches 0.5. The terminal velocity corresponding to the given drop diameter is indicated on the upper x-axis. Due to the location of the plume within the spray, a significant difference is observed in the local drop size distributions and associated drop terminal velocities. In the far spacing configuration, the distribution has shifted to the right, where there are essentially no drops smaller than 0.5 mm. In the near spacing case, more than 50% of the spray is contained in drops smaller than 0.5 mm. These differences in drop size will directly influence the penetration behavior based on the terminal velocity criterion.

Results of the penetration measurements and the scaling prediction of Eq. (6.5) using the measured drop size distributions are presented in Fig. 6.5 as a function of plume velocity. The plume velocity is presented as a ratio with a characteristic spray velocity, v_{t50}, the terminal velocity of the local d_{v50} drop size. This permits comparison between spacing configurations based on the terminal velocity criterion for penetration that $v_t/v_p > 1$. Low plume velocities appear to the left of the plot with high penetration. Penetration reduces to the right as the plume velocity increases. Experimental results are shown by the black points, while the scaling prediction Eq. (6.5) is shown by the lines. As the plume velocity exceeds the characteristic terminal velocity at a ratio of 1, a steep reduction in penetration is observed. The details of the drop size distributions accurately predict the shape of the experimen-

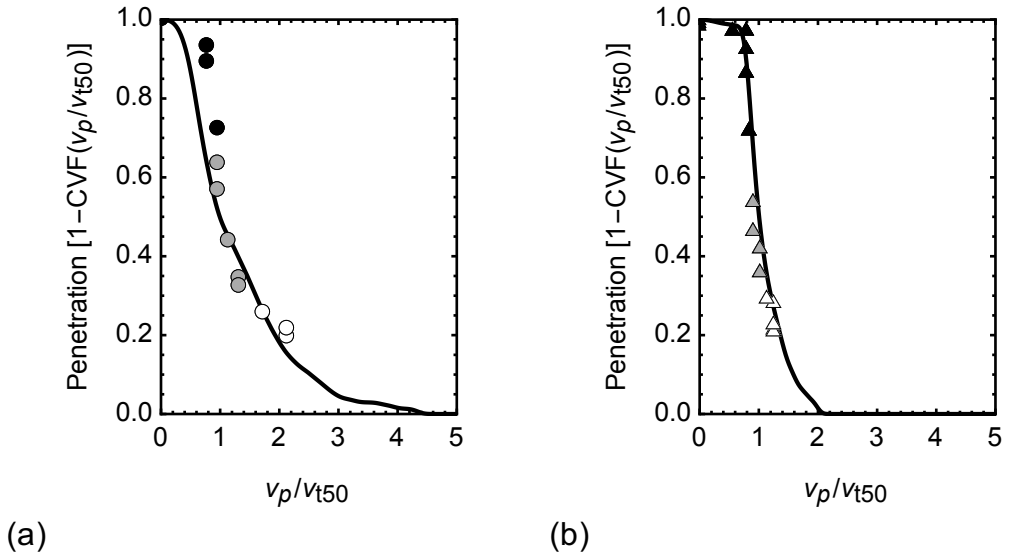

Figure 6.5: Measurements of penetration (points), and predictions based on measured local drop size distributions using terminal velocity scaling law (lines) in the close (a) and far (b) spacing configurations.

tal results, including the extended tail observed in the near spacing case due to the wider drop size distribution.

Predictions from the terminal velocity scaling may show a conservative estimate, particularly in the close spacing case where drops are often still traveling faster than their terminal velocity, as shown in Fig. 5.7a. Smaller drops that enter the plume region at the base of the plume and have a short residence time may not be reversed by the plume prior to reaching the surface, contributing more penetration than predicted by the scaling alone, resulting in experimental data points above the predicted line. Any influence of group spray drag interactions will also increase the actual penetration compared to the terminal velocity scaling, and will be discussed later.

The results indicate that the reason the far spacing case initially appears to be a better suppression condition (on the basis of penetration ratio) in Fig. 6.1 is due to the spray characteristics at the interaction location. The larger d_{v50} drop diameter at the far spray radius indicates that, overall, the individual drops will resist the opposing drag forces better and maintain more momentum than the smaller drops that are found closer to the centerline of the sprinkler. This result suggests that a solution to the penetration problem is just to use larger drops throughout, which has been recommended before and is a desired characteristic of large orifice and large drop sprinklers. One of the largest orifice sprinklers today is an ESFR type sprinkler with k-factor 363 $\mathrm{LPM/bar^{1/2}}$ (25.2 $\mathrm{gpm/psi^{1/2}}$). Based on the minimal operating pressure of 0.5 bar stipulated by NFPA 13 [3] and the d_{v50} drop size correlation [20], the largest expected volume median drop size is estimated to be approximately 2.4 mm, with a terminal velocity of 8 m/s. While this is significantly larger than the terminal velocity of the current tested Tyco D3 sprinkler, it is still less than maximum plume velocities in excess of 10 m/s observed in high-challenge storage fires [27, 46]. An additional consideration for a maximum drop size is that drops exceeding a critical diameter will breakup a second time into smaller drops when surface tension forces cannot resist the inertial forces due to the motion. This is described by the drop Weber number, $We = \rho_a v^2 d/\sigma$, where ρ_a is the air density, v is the relative velocity of the drop and air, d is the drop diameter, and σ is the water surface tension. The breakup limit is generally observed when We exceeds 12 [47]. Combining the terminal velocity equation and the critical $We \approx 12$

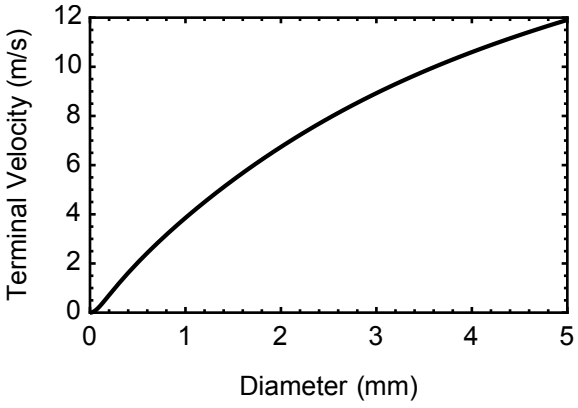

Figure 6.6: Terminal velocity versus drop diameter.

condition yields a maximum drop diameter of 5 mm. This provides a generous upper limit as the injection velocity is generally much greater than the terminal velocity, and therefore secondary breakup would occur at a smaller drop size. An additional consideration of the ESFR type sprinkler is the central spray core that is generated directly beneath the sprinkler, acts more as a jet stream of water rather than a spray of drops. This will provide locally enhanced penetration, however if the main target for suppression is off-axis, the drops and spray dispersion will be the more important factor for suppression. The increased drop size approach reaches impractical limitations and leads to the second interaction regime, which leverages smaller drop sizes.

6.4 Group Interaction Regime

6.4.1 Spray Work Scaling Analysis

An additional consideration for scaling penetration of the spray through the plume, particularly for the near spacing case, is the accumulated influence of the spray as a whole. As previously described, the group action regime is considered when the spray produces a significant drag force on the plume, causing the plume dynamics to change. In this case, drops are no longer considered on an individual basis because the one-way coupled relationship between the drops and gas phase no longer accurately reflects the plume interaction dynamics and the drop trajectory behavior. In the group interaction regime, it is possible for smaller drops with subcritical terminal velocities to penetrate the plume and reach the target surface; such drops would be overcome by the plume and be redirected if considered in the individual action regime. Several previous studies indicate these small drop interactions have an impact on penetration, identifying a characteristic global value for either spray momentum [6, 24] or drag imparted by the spray on the plume [30]. This characteristic momentum or force acting on the plume causes a change in the plume dynamics, allowing the spray to penetrate. While these previous studies investigated the relationship between a characteristic value, the current approach considers the distance over which the spray and plume interact. The drag force experienced by the drops is also acting in the opposite direction against the motion of the plume, reducing the kinetic energy within the plume. It is proposed that the

ability of the spray to influence the plume dynamics through a reduction in plume kinetic energy corresponds to the ability of spray to penetrate a weakened plume.

To evaluate the influence of the spray on the plume dynamics, an energy balance is considered around a control volume of the plume, selecting only the gas phase, shown in Fig. 6.7. The spray in this area is considered for the amount of work the drag forces from the drops will impart onto the gas phase. The analysis is considered in the vertical direction. The first law of thermodynamics states that the rate of change of energy within the control volume, dE/dt, as the relation

$$\frac{dE}{dt} = \dot{Q}_{net} - \dot{W}_{net} \tag{6.6}$$

where dE/dt represents the rate of change of energy within the control volume, consisting of internal, kinetic, and potential energies, $\dot{Q}_{net}$ represents the rate of heat added to the control volume, and $\dot{W}_{net}$ is the rate of work done by the control volume.

Recognizing the dE/dt term to be $d(me_t)/dt$, where m is the mass within the control volume and e_t is the total energy per unit mass, the derivative term can be expanded to

$$\left(e_t \frac{dm}{dt} + m\frac{de_t}{dt}\right) = \dot{Q}_{net} - \dot{W}_{net} \tag{6.7}$$

Continuing with the assumption that the mass flow from the plume is steady in time and is conserved into and out of the control volume, and there is no heat gained or lost by the plume system due to its interaction with the spray, the dm/dt

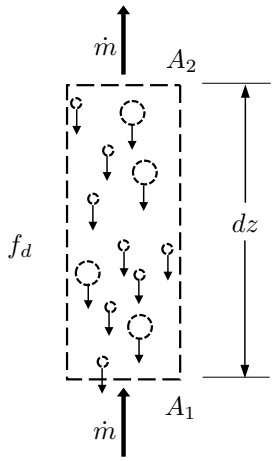

Figure 6.7: Control volume of plume containing only the gas phase, enclosing the full area of the plume cross section and a differential height, dz. The spray is treated as an obstruction to the flow within the volume and imposes a downward force on the flow.

and $\dot{Q}_{net}$ terms can be removed, leaving

$$m\frac{de_t}{dt} = -\dot{W}_{net} \tag{6.8}$$

The time derivative can be converted to a position derivative using the relation of $dz = u(z)dt$, yielding

$$mu\frac{de_t}{dz} = -\dot{W}_{net} \tag{6.9}$$

In the open boundary flow case, the atmospheric hydrostatic pressure provides a balance between the gravitational body force and pressure forces, resulting in no net work done on the control volume. The cancellation of those terms leaves only the kinetic energy, e_k, remaining on the left hand side, and means the $\dot{W}$ term on the right hand side consists of only drag body forces from the drops. This can be written as the sum of the drag force on all drops within the control volume, $\dot{W} = \sum(f_d \cdot u)$,

where f_d is the drag force on an individual drop.

The total mass within the control volume can be written as $\rho\, dV$,

$$\rho u\, dV \frac{de_k}{dz} = \sum (f_d \cdot u) \tag{6.10}$$

Dividing the right side by $u\, dV$, the velocity terms cancel and yields a total drag force per unit volume, $\sum f_d/dV = F_d'''$. The F_d''' term can be calculated based on locally measured (or model predicted) quiescent spray characteristics, including drop size, drop velocity, and number density, at various locations of interest so that a profile of these characteristics is known as a function of height within the plume region $F_d'''(z)$. Substituting in $e_k = \frac{1}{2}\rho u^2$ results in the relationship

$$\frac{1}{2}\rho \frac{du^2}{dz} = F_d'''(z) \tag{6.11}$$

Separating the variables yields a final form, relating the plume kinetic energy to a cumulative volumetric work term,

$$\frac{1}{2}\rho u^2 = \int_0^{L_{ref}} F_d'''(z) dz \tag{6.12}$$

where the integration along the z-direction is bounded by the ground and a reference height, L_{ref}, determined by the configuration geometry of the sprinkler and plume alignment. The height of L_{ref} includes spray that is tracing trajectories to the target surface. The important parameters for the spray work scaling are the relationship of the total volumetric work that the spray exerts on the plume, $\int F_d'''(z) dz$ and the initial volumetric kinetic energy of the plume at the base, $\rho u^2/2$.

It is proposed that when the spray drag forces are sufficient to remove the kinetic energy associated with the plume flow, the plume reaches a critical condition

where it cannot overpower the spray, providing a scaling relationship for penetration

$$PR(v_p) \sim \int F'''(z)dz \,/\, KE \tag{6.13}$$

6.4.1.1 Comparison to Spray Momentum

Previous studies suggest that spray momentum compared to the plume momentum is an important parameter determining spray-plume interactions. However, determination of the appropriate scale between the two momenta is unclear. Through the consideration of the drag forces that the plume and drops exchange, the evolution of the effect of the momentum can be evaluated. The evaluation of the spray work can be compared to the spray momentum in the following way.

The momentum of the spray (per unit area), $\dot{M}_s''$, can be calculated from the product of mass flow rate of water drops, $\dot{m}''$, and the velocity of the drops, v,

$$\dot{M}_s'' = \dot{m}'' v \tag{6.14}$$

Substituting for $\dot{m}''$ to introduce the volume flux, $\dot{V}''$ of the spray,

$$\dot{M}_s'' = \rho_w \dot{V}'' v \tag{6.15}$$

and then multiplying by v/v and recognizing that the spray volume fraction can be written as $VF = \dot{V}''/v$, the simplification results in

$$\dot{M}_s'' = \rho_w VF v^2 \tag{6.16}$$

producing a final scaling for spray momentum flux as

$$\dot{M}_s'' \sim VF v^2 \tag{6.17}$$

The two terms in the scaling relate to the amount of water delivered, and the pressure of the injection (influencing both volume and velocity). This value provides a general integral metric describing the spray momentum, but generally ignores the localized interactions. It is well suited for a consideration of the interactions present in a directly aligned configuration where the momentum of the spray acts along the full direction of the plume.

For comparison, the spray work scaling can be explored beginning from the total drag force, F_D, produced by the spray,

$$F_d = N_d \left(\frac{1}{2} \rho_a C_D A_d u^2 \right) \tag{6.18}$$

where the term in brackets is the drag force on a single drop. The variable N_d represents the total number of drops in the spray, which can also be written as $N_d = ndV$, where n is the number of drops per unit volume and dV is a differential volume containing drops. Another relationship for volume fraction can be written to include the volumetric drop density

$$VF = \frac{N_d V_d}{dV} = nV_d \tag{6.19}$$

Substitution of these variables results in

$$F_d = \frac{VF}{V_d} dV \left(\frac{1}{2} \rho_a C_D A_d u^2 \right) \tag{6.20}$$

Simplifying the ratio A_d/V_d and dividing each side by dV provides the volumetric drag force introduced in Sec. 6.4,

$$F_d''' = \frac{3}{4} \rho_a C_D \frac{1}{d} VF v^2 \tag{6.21}$$

and the final scaling of the volumetric drag term becomes

$$F_d''' \sim \frac{VFv^2}{d} \tag{6.22}$$

Finally, in the spray work scaling, the F''' term is integrated over the height of the spray-plume interaction, adding the effect of height to the scaling.

$$\int F_d''' \sim \frac{VFv^2H}{d} \tag{6.23}$$

The additional benefits of the drag work formulation, Eq. (6.23) compared to the momentum based approach, Eq. (6.17) is the explicit inclusion of drop size effects and the distance over which the spray and plume interact, through the integral term. These are important characteristics of the interaction that are not directly included in the momentum formulation. By introducing the length scale of the interaction, the formulation is applicable directly to a large range of configurations that can be considered on a local scale rather than the complete integral comparison of the spray and plume momenta.

6.4.1.2 Evaluation of Spray Work

Determining the value of the spray-plume interaction parameter requires knowledge of the spray field in the location of the plume to evaluate the drag interactions. It is possible to use the initial spray measurements as a reasonable first guess, however the initial spray will be significantly different than the spray that has evolved along the path to the target location. Drag effects have a large influence on the spray and will preferentially filter out smaller drops as the radial distance from the

sprinkler increases, as observed in the measurements in Ch. 5. Drag also slows the radial velocity of the drop, curving the trajectory of the drops downward. The combination of these effects will change the characteristic number density and velocity vector of the spray in a given location.

The F_d''' term can be calculated based on measured spray characteristics that are present in the drag equation, including drop diameter and drop velocity, at various locations of interest so that a function of $F_d'''(z)$ is known throughout the plume elevation. Also important is the drop number density n (drops/m^3), which serves as a multiplier of the individual drop drag force to account for all drops in the spray.

The drag force for a single drop can be represented as shown in Fig. 6.3 and used in Eq. (6.3). Multiplying the single drop drag by the total number of drops within the control volume of a given size, N_d, and assuming only the vertical velocity components for plume penetration, provides the total drag force in the vertical direction,

$$F_d = N_d \left(\frac{1}{2} C_D \rho_a A_d (u - v)^2 \right) \tag{6.24}$$

The volumetric formulation used in Eq. (6.23), F_d''', is obtained by dividing both sides of the drag force by the differential volume, dV, leaving a volumetric drop number density on the right hand side, $n = N_d/dV$, where n represents the number of drops per unit volume.

Inputs to the local drag force equation are sourced from the optical shadowgraph measurements from the quiescent case, and include A_d and v. Also available

from the shadowgraph measurements is the volume flux, $\dot{V}''$, which is used to determine the drop number density

$$n = \frac{\dot{V}''}{V_d v} \tag{6.25}$$

where v is the vertical component of the optically measured drop velocity and V_d is the drop volume of the drop.

Each drop is a different size and is traveling at a different velocity, so precise accounting of the total drag force would require the evaluation of each drop in the spray. In practice, the spray can be considered in several drop size "classes" consisting of drops within a given size range. The measured drops can be collected into discrete groups so that a characteristic drop size and velocity can be used for each class, and the measured volume flux can be used to determine the number density to use for each drop size class.

For this analysis, the drop size distribution for all measurement locations within the plume was considered, and divided into 10 drop size groups in ranges of d =(d_{min}–d_{v10}), (d_{v10}–d_{v20}), (d_{v20}–d_{v30}), etc., such that each class contained equal volume fractions, or 10% of the measured volume flux. The characteristic diameter of each class was the median of the class, i.e. d_{v5},d_{v15},d_{v25}, etc. The spray properties n and v were determined for each drop size groups at each elevation location to provide a profile for each drop size class. For each group, $F'''(z)$ was evaluated, and summed together to obtain the total local spray drag force, which was then integrated over the height of the spray interaction. Appendix D shows the calculation of the local drag force profile along the plume elevation for the different drop

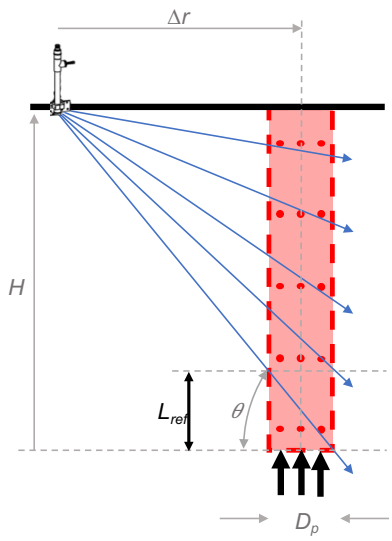

Figure 6.8: The function of local drag force is integrated over the interaction distance characterized by drops that are directed to the base of the plume, a function of the configuration geometry.

size groups. The relevant interaction height was determined by the spray that was directed to the target location through geometry, indicated in Fig. 6.8, and identifies only drops which have a potential to reach the target area and directly influence penetration. While the spray above this height has additional drag influence on the plume, these interactions do not have an influence on the interactions that govern the local penetration of the spray to the base of the plume. At heights above this region, the influence of the spray on the plume could be calculated to evaluate how the plume dynamics evolve, through a solution of Eq. (6.12) where the plume velocity varies with elevation. In this case, a stagnation point where the spray and plume meet could possibly be identified. While this would provide an analysis of the spray influence on the plume, the resulting information about how the plume

penetrates through the spray is not the point of interest when determining the spray penetration through the plume.

6.4.2 First Law Scaling Results

Penetration results viewed in terms of the spray work scaling are seen in Fig. 6.9 for the close spacing and far spacing condition with two operating sprinklers. Circle points represent the near spacing condition, triangles represent the far spacing. The data points are again shaded based on a penetration value (white <30%, black >70%, and gray in-between). Results clearly show that the spray influence is a poor predictor for penetration in the far spacing case because the spray influence is very small for all plume velocities. This is expected due to the lower number of drops, larger drop diameters, and lower volume flux at the far locations. Additionally, the larger distance from the sprinkler to the plume centerline reduces the effective interaction height, shown as L_{ref} in Fig. 6.8. The primary factor in this result, however, is likely the much smaller number density in the far spacing case. In the close spacing case a correlation between penetration ratio and the penetration scale exists. In this configuration, the spray work scaling is becoming important, and at a W/KE ratio near 1, penetration ratio transitions through the marginal range.

The results presented for the two conditions (near and far spacing) in Fig. 6.9 come from the same global spray properties; the overall spray is the same, but the main difference is due to location effects. From Eq. (6.23), the influence of local values includes

- drop number density
- vertical drop velocity
- drop size
- interaction height based on location geometry

The implementation of a location based analysis including local spray characteristics allows for inclusion of these additional relevant spray physics compared to an integral metric based on a global momentum value or an overall drop characteristic such as a Sauter mean diameter describing the drag influence.

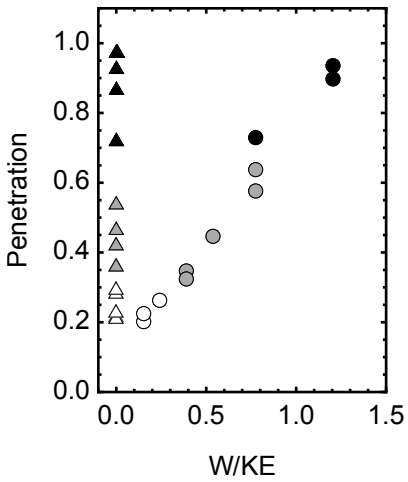

Figure 6.9: Plume penetration scaled with spray work. • near spacing, ▲ far spacing. Shading corresponds to penetration value. White <30%, black >70%, gray in-between.

However, with the success of the terminal velocity scale, it is not conclusive that the spray work scale is the dominant scaling of the interaction. For a more definitive analysis of the scaling, another condition, towards a denser spray with

smaller drops, would be required, which is not achieved with the current experimental set-up. While these drag interactions may play a role in the near spacing case, the current results are inconclusive about the analysis. Additional study applying the analysis to centered spray-plume configurations and to sprays with smaller drop sizes that do not correlate with the terminal velocity may provide more insight, and is discussed in Sec. 6.5.

In this analysis, drag effects of the spray on the plume were considered in the current configurations, however, results suggest the overall work and kinetic energy transfer between the spray and the plume is not a dominating factor when considering the off-center configuration. Drops that enter the plume from the side of the plume and at lower elevations along a trajectory directed at the base of the plume will interact independently from the influence of the spray at higher elevations. These drops will not be influenced by the plume during their entire lifetime. Independent of where drops enter the plume is the drag force balance at the terminal velocity limit. This seems to be an effective scaling for penetration, when compared to a characteristic plume velocity.

6.5 Scaling Analysis Extension

6.5.1 Reach of Current Analysis

The results of the two scaling analyses indicate that the conditions tested in the SAF operating with two sprinklers are dominated by the individual drop penetration

due to terminal velocity. While a correlation between W/KE is observed in the close spacing case, there are very few conditions with a supercritical work parameter, and even in these cases the terminal velocity is still an important factor. The relationship between the two scaling parameters is seen in Fig. 6.10 which plots the velocity ratio versus the spray work parameter for each flow configuration, indicating the relative contribution of each penetration mechanism. The shaded region at the bottom of the plot indicates the penetration regime where drops penetrate due to their individual terminal velocities. Data points in this bottom region correspond to definite penetration based on the terminal velocity scaling. The second shaded region, to the right of the plot at $W/KE > 1$ corresponds to the regime where penetration is achieved due to the spray work interactions with the plume. Points in the bottom right where the two shaded regions overlap correspond to an inconclusive condition where both penetration mechanisms are possible. While the two regimes have been presented separately, and a line marking the shaded region is defined, they will not work completely independently; the influence of both penetration regimes may combine and the boundary between regimes is not perfectly clear cut. For example, a spray imposing moderate work on the plume will slow the plume velocity, allowing for a lower critical terminal velocity requirement for penetration, and the combined action of the spray interaction will lead to increased penetration than when considering the terminal velocity criterion alone. The color of each data point corresponds to the level of penetration achieved. Black points indicate $PR > 0.7$ while white points indicate $PR < 0.3$. The gray points suggest an intermediate

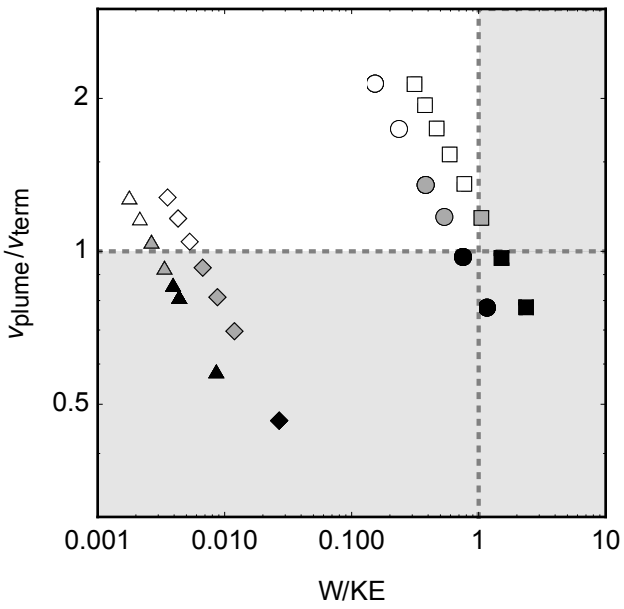

Figure 6.10: Penetration data plotted as a function of scaling parameters for all data sets, identifying the level of penetration by color. (● near spacing 2, ▲ far spacing 2, ■ near spacing 4, ♦ far spacing 4, shading corresponds to penetration value)

transition zone of marginal penetration. From these points it is observed that the general penetration regimes correspond to the level of penetration, however there is some transition region or combination effects where the shaded boundaries have been drawn. The overlap of the two contributing regimes is seen through the marginal penetration cases identified by the gray colored data points.

It is noted that the penetration ratio measurements presented this far correspond to the flow condition used in Ch. 5 with two sprinklers activated; this flow configuration allows for the local spray properties to be measured. The two-sprinkler results are shown in Fig. 6.10 by the circle points (close spacing) and triangle points

(far spacing). These two conditions skirt around the top right quadrant of the plot, indicating that a condition where successful penetration is independent of the drop terminal velocity. To increase the spray work independently from the drop size, an increased number of sprinklers can be used. Additional penetration ratio measurements were taken using all four sprinklers in the SAF simultaneously to nominally double the volume flux while keeping the drop sizes relatively similar. In these cases, the work interactions are doubled due to the doubled volume flux, and are represented in Fig. 6.10 by the square points (close spacing) and the diamond points (far spacing).

There are notable limitations in the four sprinkler data points, however. First, these data points assume the same terminal velocity information as measured in the two sprinkler configuration. This may not be a completely accurate assumption, particularly in the far spacing case where differences in drop size distribution may be enhance by the lower drop count and the influence of initial spray variations due to the slot/tine geometry. This may explain some of the disagreement related to the far spacing 4 sprinkler case (diamond points) where marginal penetration is noted below the critical line in Fig. 6.10. If the terminal velocity of the combined four sprinkler sprays has a slightly lower v_{term} (due to different localized spray drop size distributions) these points would move up on the y-axis. For example, adjustment of the d_{v50} drop size to 0.57 mm instead of 0.73 mm would adjust the terminal velocity to 2.3 m/s instead of 2.9 m/s, shifting the diamond points upward to correspond with the critical line at 1. Additional uncertainty is present in the x-direction as

well, assuming that the work calculated from the two sprinkler condition is simply doubled in the four sprinkler configuration.

Note that there is limited data in the upper right quadrant, where terminal velocity is too weak but penetration may occur due to drag interactions of the spray. Based on the spray generated in the current test conditions, the drop size and spray work conditions are not achievable independently. A condition where the spray work dominates without a potential for individual drop penetration would be desired. These conditions would be characteristic of sprays with even smaller drop sizes than those observed near the sprinklers in the current measurements. While not possible with the current facility, test data reporting fire suppression ability with different low to medium pressure (10.3–13.8 bar) water mist nozzle configurations was explored to expand the current data set.

6.5.2 External Data Set

To explore the scaling in this region, outside experimental data was implemented from water mist fire suppression tests of wood-crib fires [41] which provided incomplete, yet sufficient, spray information to implement the W/KE analysis with some assumptions. Including this dataset also presents to opportunity to apply the current scaling analysis to a case with real fire suppression. There are several differences between this external data set and the current study. The suppression experiments consist of a real fire of approximately 275 kW heat release rate, they use water mist, and the spray nozzle is located directly above the fire at a height of

1.3 m above the fuel surface. Each of these differences requires consideration when the current scaling analysis is applied.

Spray Considerations

For implementation in the W/KE analysis, profiles of spray properties including volume flux, drop size, and drop velocity are required. While the complete data is not presented in the paper, a few assumptions can be made to move forward.

For volume flux considerations, the known flow rate from the nozzle and the known spray angle can be used along with the assumption that the spray is uniformly distributed within the solid cone. While the original cone angle is 90°, the radial component of spray velocity will decay rapidly and the wide trajectory will not persist to the floor. Based on trajectory analysis of the small drop size at an initial angle of 90°, the maximum diameter of the spray can be estimated at 1.2 m. While the floor measured volume flux shows some nonuniformity, the calculated fluxes using this truncated cone method agree well with the reported average delivered density.

The drop velocity profile is also required, and only the initial velocity is provided. Additional information from the nozzle data sheet [48] shows the initial spray cone dissipates into a continuous fog after a listed distance. For calculation, the drop velocity was assumed to follow the solution to the drop drag equation, Eq. (6.3). Using initial conditions as measured in the paper, an initial velocity of 10 m/s is considered at a distance 0.2 m below the nozzle. The solution to the differ-

ential equation suggests that the drop reaches it's terminal velocity in a distance that agrees with the listed reach of the momentum dominated spray region. Therefore, the solution to the drag equation was used to estimate the drop velocity profile.

The mist was generated by nozzles with a range of orifice diameters and at two pressures. For some of the test cases, drop size and velocity of the spray was measured at a distance 0.2 m below the nozzle. The drop size reported is the Sauter Mean Diameter (SMD), which is typically smaller than the volume median d_{v50} drop diameter. While these drop sizes are not directly comparable, they compare reasonably well with a correlation for drop size based on orifice Weber number to predict d_{v50}. Additionally, no drop size distribution is provided in the reference, and so increased fidelity is added by using a drop size distribution; a monodispersed spray is assumed for these conditions.

Because of the configuration differences, the height over which the spray work is considered spans the entire distance from the fuel surface to the sprinkler, as opposed to the current SAF configuration where only a small elevation of the spray is considered for penetration. The local drag force from the spray was integrated from 0 m up to 1.1 m (0.2 m below the nozzle where the provided spray measurements were taken). At locations closer to the nozzle, the spray is extremely dense and is not considered in this analysis.

Plume Considerations

In the current study the competition to the spray is provided by an ambient temperature air jet with a specified initial velocity. This same concept does not directly apply to the case of the real fire condition in the work by Santangelo. However, a characteristic peak velocity of the fire is calculated based on a correlation of the heat release rate, $v_{flame,max} = 1.9HRR^{1/5}$ and is approximately 6 m/s for the wood-crib fires. Additionally, the gas is heated and will have different density and viscosity characteristics than the ambient jet used in the current study. Using the plume findings of Heskestad, the temperature rises by 650 K at the flame tip where the maximum velocity occurs [42], corresponding to a density decrease by a factor of 3 and an increase in viscosity by a factor of 7 [49]. A conservatively high kinetic energy of the plume is calculated using the hot temperature density and the characteristic plume velocity, and the changes in air properties will influence the drag force produced by the drops on the plume.

Additional Datasets

An additional data set was also considered for inclusion in the current analysis. Recent measurements of spray-plume interaction by Zhou in a small-scale configuration include very small drop water mist [24]. However, several considerations make application of the current W/KE analysis difficult to this data set. While very detailed measurements of volume flux, drop size, and velocity were obtained,

there is limited information regarding the elevation profile of these spray characteristics. In this case, the momentum of the spray exhibits a significant influence on the far-field drop velocity. Despite the drops being very small, nominally 0.05 mm, they do not slow to their terminal velocity, and are still traveling at nearly 5 m/s upon interaction with the hot air plume. While this is dramatically slower than the initial velocity of 18 m/s near the injection, the velocity remains much greater than the terminal velocity of the small drops. This suggests the spray nozzle used in this study operates on a different principle where the narrow cone angle of 30° yields jet-like behavior, where the core velocity is maintained at elevated levels, and entrained air contributes significantly to the spray momentum, insulating it from direct plume influence. In fact, the nozzle used by Zhou uses an orifice atomization, while the BETE P nozzles used by Santangelo use an impingement atomization, significantly reducing the injection velocity from the orifice.

6.5.3 Result Discussion

The results of the scaling analysis to the expanded data set from the wood-crib testing is shown in Fig. 6.11 by the star shaped points. The different test conditions are also labeled by the spray nozzle used. Immediately noticeable is the influence of the very small drop sizes present in the spray, resulting in very high v_p/v_t ratios.

The points are once again colored by the extent of penetration. The P120 test delivers the highest volume of water and is predicted to have the largest plume influence. Suppression in this case is very successful. In the P66 and P80 cases,

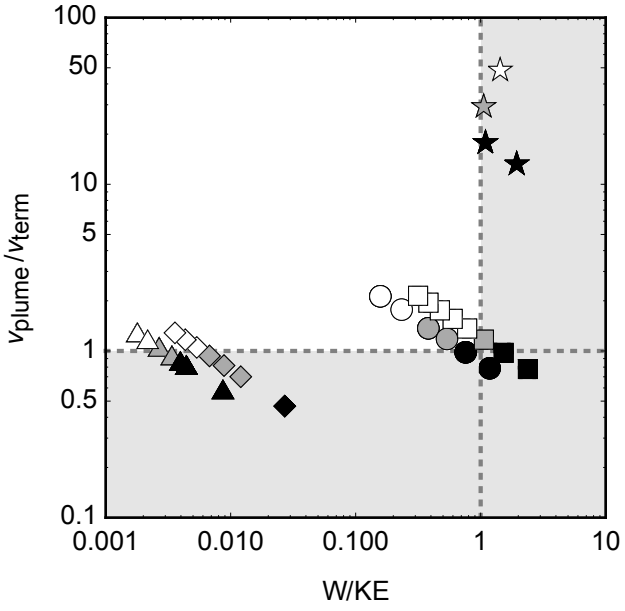

Figure 6.11: Extension of the results to include application of the scaling analysis on mist suppression testing of real fires. (• near spacing 2, ▲ far spacing 2, ■ near spacing 4, ♦ far spacing 4, ★ fire suppression tests from [41], shading corresponds to penetration value)

suppression is not as easy. The reduced volume flux suggests a smaller W/KE ratio closer to the proposed critical vale around 1. A significant outlier is observed in the P54 nozzle test condition. It is very possible that the assumptions for the W/KE calculation are not accurate to the spray conditions. However, it is important to note that suppression depends on factors other than percent penetration, including a critical application rate or delivered volume flux. While the point lies in the upper right quadrant indicating penetration due to spray work interactions, it does not necessarily mean that a critical volume flux was achieved. This test case supplies the lowest volume flux in the quiescent condition to begin with, so even though penetration may be occurring, suppression may not be successful strictly because the

actual amount of water available to be delivered is insufficient for suppression. This result highlights the fact that there are additional factors than solely penetration ratio that govern suppression. This is a case in the current measurements as well. Even though the far spacing case shows a high penetration ratio, the actual volume flux delivered to the target even at $PR = 1$ (1.5 mm/min) is still less than the volume flux delivered in the weakest close spacing test condition (2.8 mm/min).

Additional consideration that is not accounted for in the current analysis is the effect of evaporation. Particularly in the P54 nozzle test, the drop size is very small at an estimated 100 μm, and would be susceptible to very fast evaporation.

6.6 Summary

The ability of a sprinkler spray to penetrate through a simulated fire plume was investigated for a range of spray characteristics and plume strengths. While current sprinkler protection design methods do not consider local spray variations or the ability of a given spray to achieve penetration through a fire plume, a scaling analysis was explored in to provide a framework useful for evaluation of a given sprinkler design through knowledge of local quiescent spray characteristics. Two regimes of spray-plume interaction and penetration were explored—the first based on individual drops and terminal velocity, the second based on accumulated spray drag interactions from the entire spray. In both cases, penetration is governed by very localized spray-plume interactions corresponding to a small fraction of the total dispersed drops in the vicinity of the plume. It is the local drop characteristics that

determine penetration rather than a more global integral representation of the spray. The analysis framework is used to identify and evaluate the relevant drops in the spray based on the physical mechanism responsible for penetration.

In the experimental conditions currently tested, the terminal velocity criterion for penetration yields excellent results to predict the level of spray penetration. The differences in local spray drop size distributions are a dominating factor regarding penetration and predict the experimental results well. Viewing the measurements with respect to the work from spray drag interactions shows that far from the sprinkler centerline, where the spray is sparse and contains only large drops, there is limited influence on the plume and the spray work is a poor indicator of penetration ability. However, near the spray centerline where the spray is comprised of small drops, work effects show a correlation to penetration. These work effects incorporate spray number density, drop velocity, drop size, and the effective vertical distance of the interaction. It is likely that the scaling for each regime overlaps somewhat, and there are configurations such as the current near spacing case where both scaling parameters must be evaluated to determine the penetration potential of the spray. Extension of the analysis to external fire suppression datasets is feasible, and shows relatively consistent results to the current dataset.

Chapter 7: Conclusions

The present work implements a unique multi-sprinkler facility, representing a fundamental sprinkler protection grid configuration, to investigate the dispersion and subsequent interactions of fire sprinkler sprays with a competing fire plume. Understanding of the spray-plume interactions, which dominate the suppression effectiveness of sprinklers, is critical for improvements in fire sprinkler protection of increasingly demanding hazards as well as for development of detailed computer modeling of such suppression sprays. Both the initial and dispersed spray measurements show the complex and spatially non-uniform characteristics of the spray, and are unique for individual sprinklers. This fact complicates both fire suppression effectiveness and the ability to accurately model suppression sprays using CFD solvers. The research objectives were grouped into three areas, including (1) development of a CFD spray model validation dataset, (2) refinement of spray dispersion measurement methods, and (3) development of a framework to identify plume penetration performance for engineering application. The results and contributions are summarized as follows.

7.1 Comprehensive Experimental Dataset

The set of comprehensive spray measurements presented throughout this research provides insight to the mechanisms of plume penetration along with a much desired dataset for implementation in CFD models, for both initial spray input conditions as well as data for model validation and development. The dataset is comprised of measurements describing the spray from initial injection, to volume flux distribution on the floor, and interaction and penetration through a simulated fire plume. The complete details of experimental set-up and configuration, along with detailed local spray measurements, was previously unavailable. The dispersed spray and plume interaction measurements, while providing physical insight through the presented scaling analysis, would be relatively unhelpful for model validation without the accompanying initial spray details due to the variations in spray characteristics that occur naturally in sprinkler sprays. The inclusion of all measurements from the same configuration allows for the direct application of the presented data for model validation.

The comprehensive experimental dataset contributes

- detailed spatially-resolved measurements to support model validation
- a complete dataset including relevant initial spray and far-field spray dispersion measurements
- critical alignment and experimental configuration details to provide reliable

boundary conditions

7.2 Refinement of Spray-dispersion Measurement Methods

Volume flux measurements of spray dispersion from an array of sprinklers, in a general sprinkler system grid configuration, were taken with a fine resolution of 5 cm. In addition to supporting model validation, these measurements highlight the limitations of current industry standard acceptance tests in regards to identifying spatial variations in the spray pattern that may influence the suppression effectiveness of a particular sprinkler.

The dispersed spray measurements contribute

- spatially-resolved dispersed spray measurements to support model validation
- a high resolution analysis providing insight to critical length scales
- evidence for requirements of the spatial resolution of measurements corresponding to 4% of spray reach

7.3 Penetration Framework

A scaling framework considering the contributions of individual drop terminal velocities for plume penetration, as well as the accumulated influence of drag interactions from the entire spray was presented to predict penetration performance based on local quiescent spray characteristics. This analysis may be useful for engineering application by considering the local spray properties and behavior in regard

to penetration performance.

The penetration measurements and scaling analysis contribute

- a framework for the analysis of spray penetration capability based on quiescent spray properties
- results show that local drop size distribution and terminal velocity ratio predict penetration performance
- an analysis of local accumulated spray work contributions rather than a global characteristic momentum ratio to predict penetration in the group action regime
- analysis of additional fire suppression data to apply the current analysis to expanded conditions and real fire data

This study was limited in terms of available lab capabilities, such as ceiling height, ability to use a real fire, and the analysis ignores the influence of evaporation, which may have an impact on the applicability of the spray work analysis for sprays of very small drops. Future work to include additional spray configurations with the same spray data could extend the analysis and better determine the limitations and applications. The current experimental configuration limited the analysis to conditions where the terminal velocity was still coupled to the spray work scaling parameter. Additional test conditions with smaller drops are required to better evaluate the spray work analysis independent of the drop terminal velocity. Future work regarding the influence of evaporation, application to a real fire plume, and

incorporating the complexities of dense sprays with high entrainment, such as fine water mist, would further advance the understanding of the spray-plume interaction. For the engineer, this current research shows that the penetration is directly related to the spray drop size distribution, and the drop terminal velocity is the critical parameter.

Appendix A: Complete Initial Spray 4S Measurements

Measurements of the initial spray are presented here for each sprinkler used in the study for CFD model spray initialization. Sprinklers were Tyco D3 spray nozzles with k-factor 33 LPM/bar$^{1/2}$ (2.3 gpm/psi$^{1/2}$) operating at a pressure of 1.38 bar (20 psi).

For each sprinkler, five datasets are presented including volume flux, $\dot{V}''$, volume median drop diameter, d_{v50}, drop distribution width parameter γ, break-up radius, r_{bu}, and the drop velocity at the break-up location, u_{bu}. Measurements include complete 360° azimuthal measurements at 11 elevation angles. The quadrants of the sprinklers not directed toward the center of the array have been shaded.

The drop size distribution can be defined using the local d_{v50} and γ measurements at a given elevation angle θ and azimuthal angle ϕ around the initial spray through the combined log-normal Rosin-Rammler distribution [17, 20],

$$CVF_{V,d}(d|\theta,\phi) = \begin{cases} \frac{1}{\sqrt{2\pi}} \int_0^d \frac{\gamma}{1.15d'} \exp\left[\frac{-\ln\left(d'/d_{v50}\right)^2}{2(1.15/\gamma)^2}\right] dd', & d < d_{v50} \\ 1 - \exp\left[-0.693\left(d/d_{v50}\right)^{\gamma}\right], & d > d_{v50} \end{cases} \tag{A.1}$$

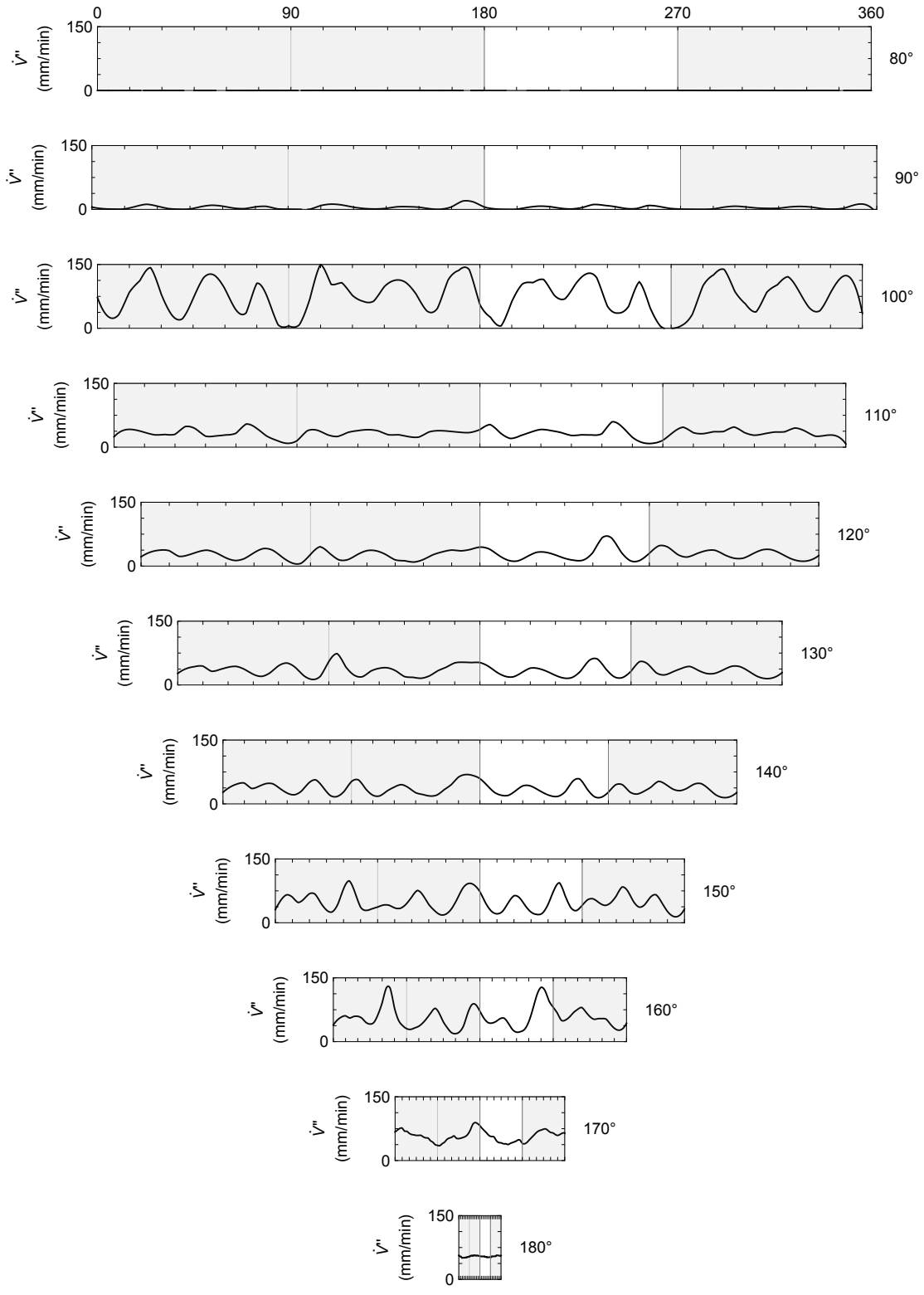

Figure A.1: Volume flux measurements, $\dot{V}''$, for Sprinkler #1 (mm/min).

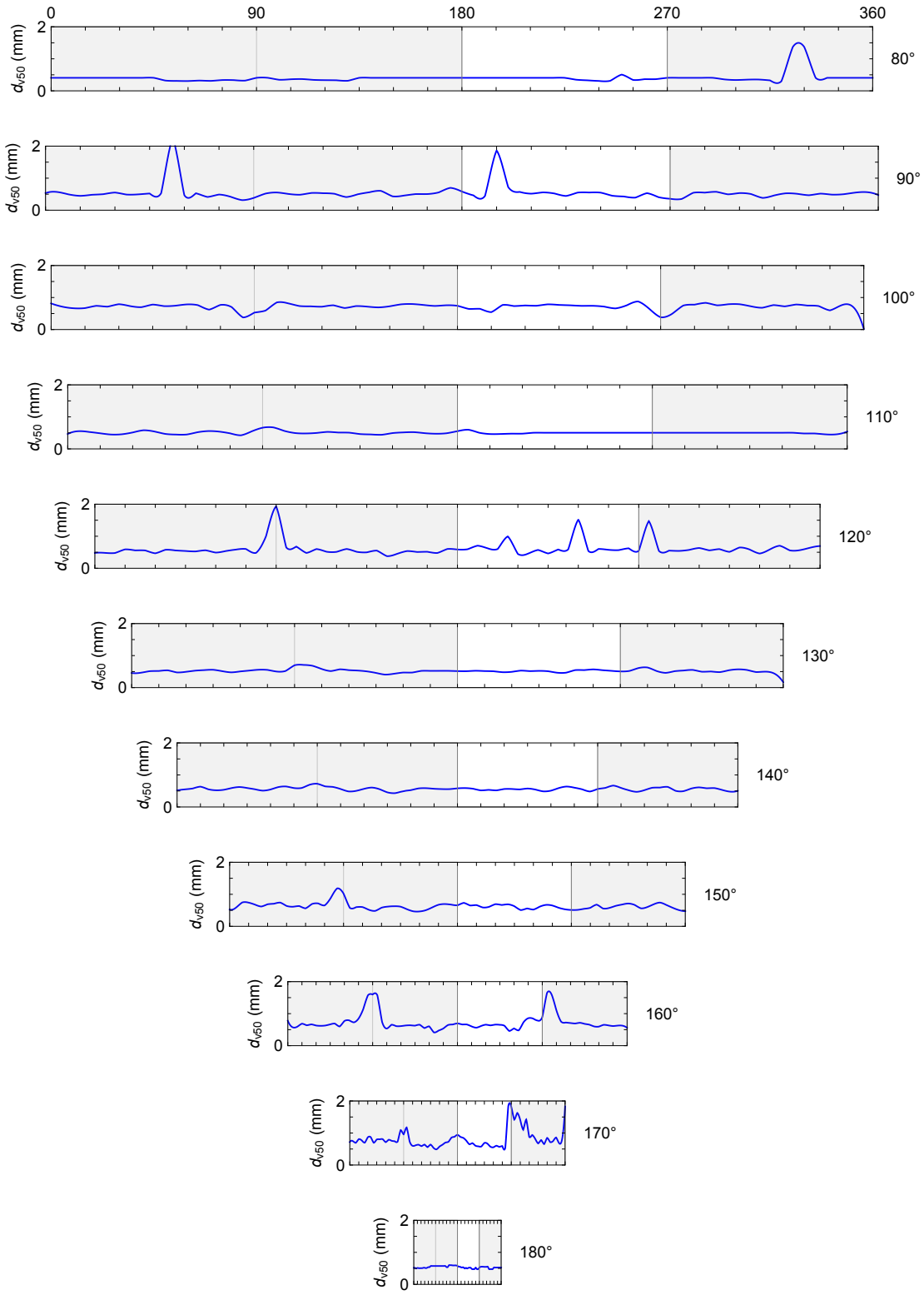

Figure A.2: Drop size, d_{v50}, measurements for Sprinkler #1 (mm).

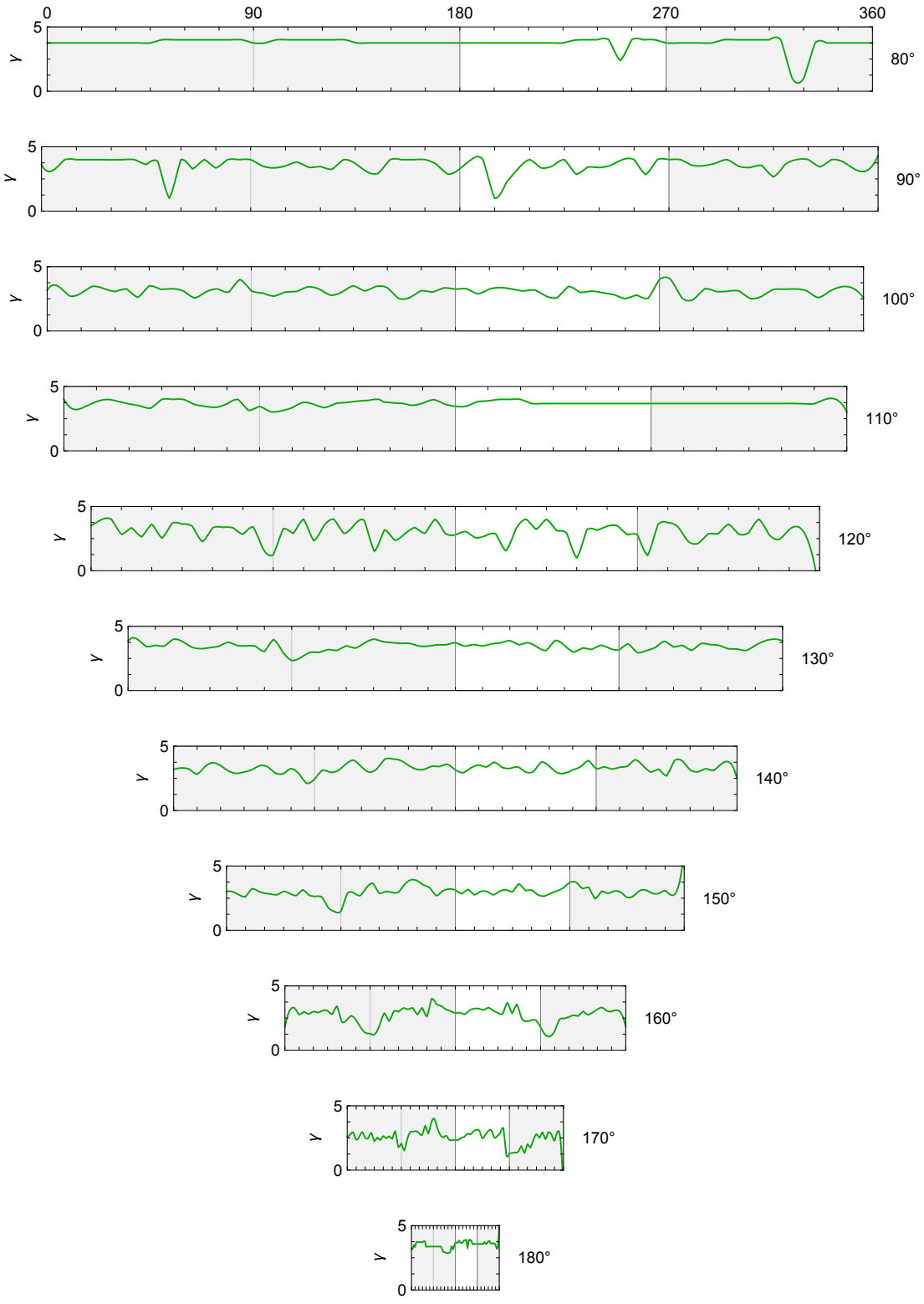

Figure A.3: Drop size distribution width measurements, γ, for Sprinkler #1.

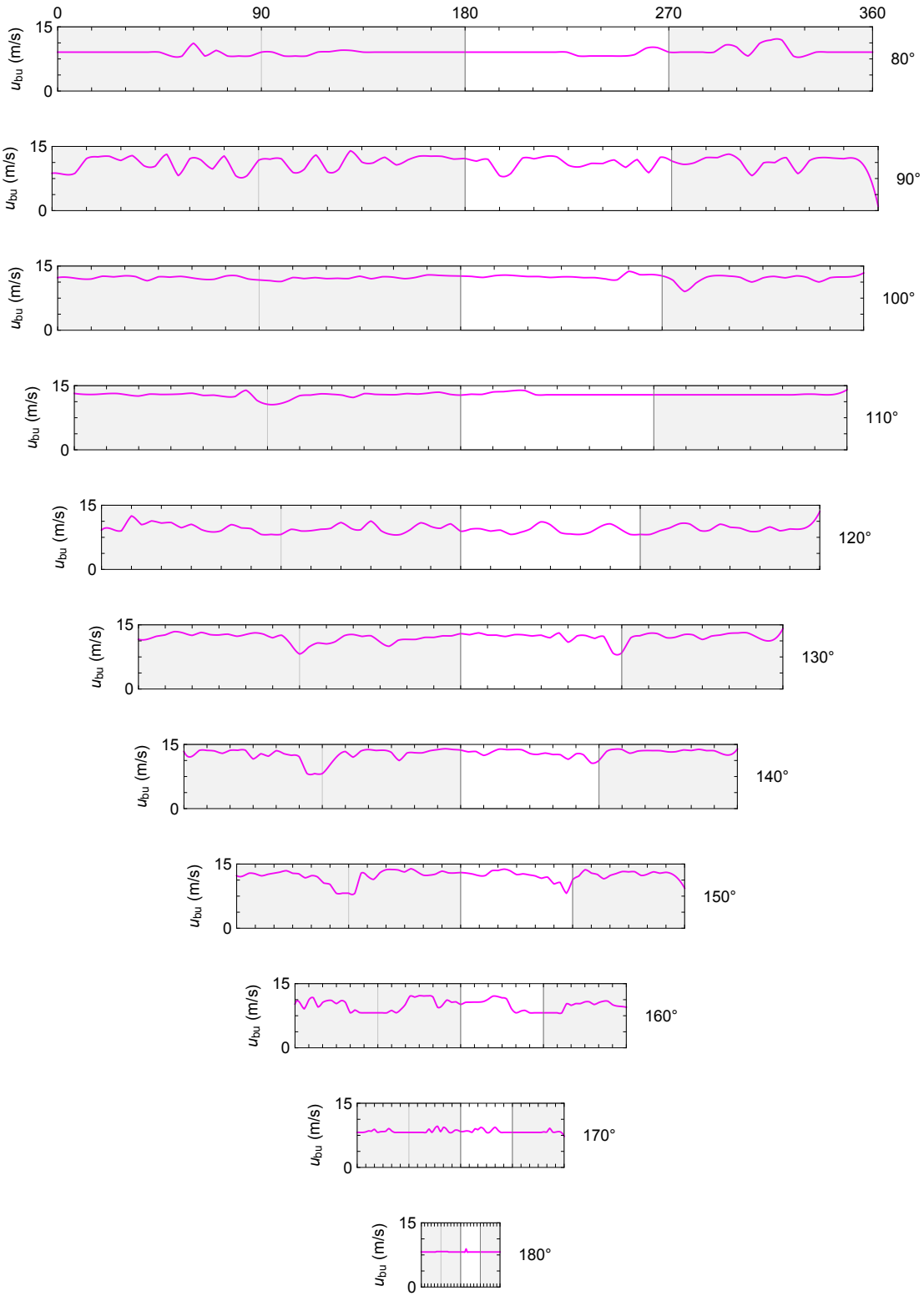

Figure A.4: Initial drop velocity measurements, u_{bu}, at the break-up radius r_{bu} for Sprinkler #1 (m/s).

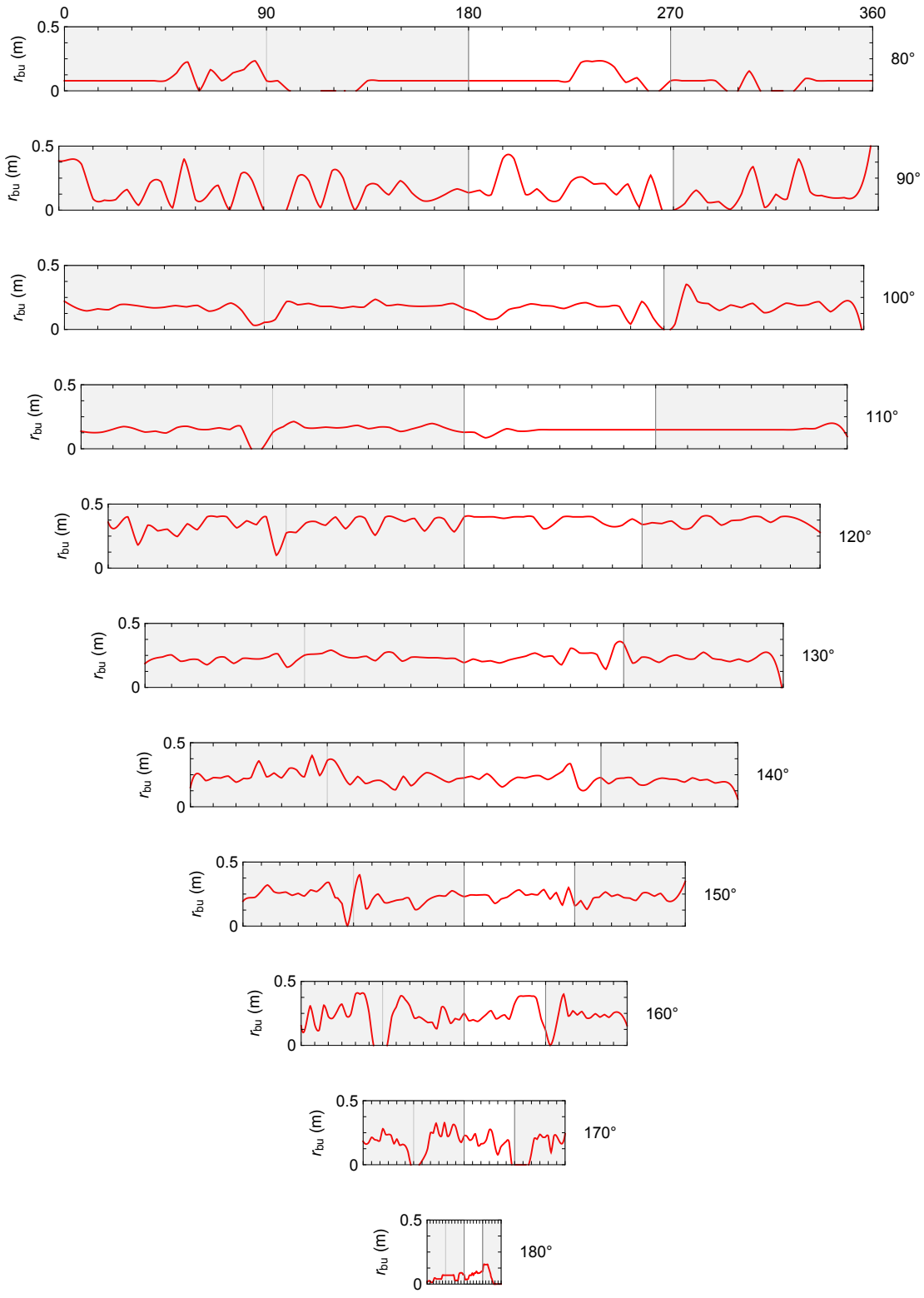

Figure A.5: Break-up radius, r_{bu}, measurements for Sprinkler #1 (m).

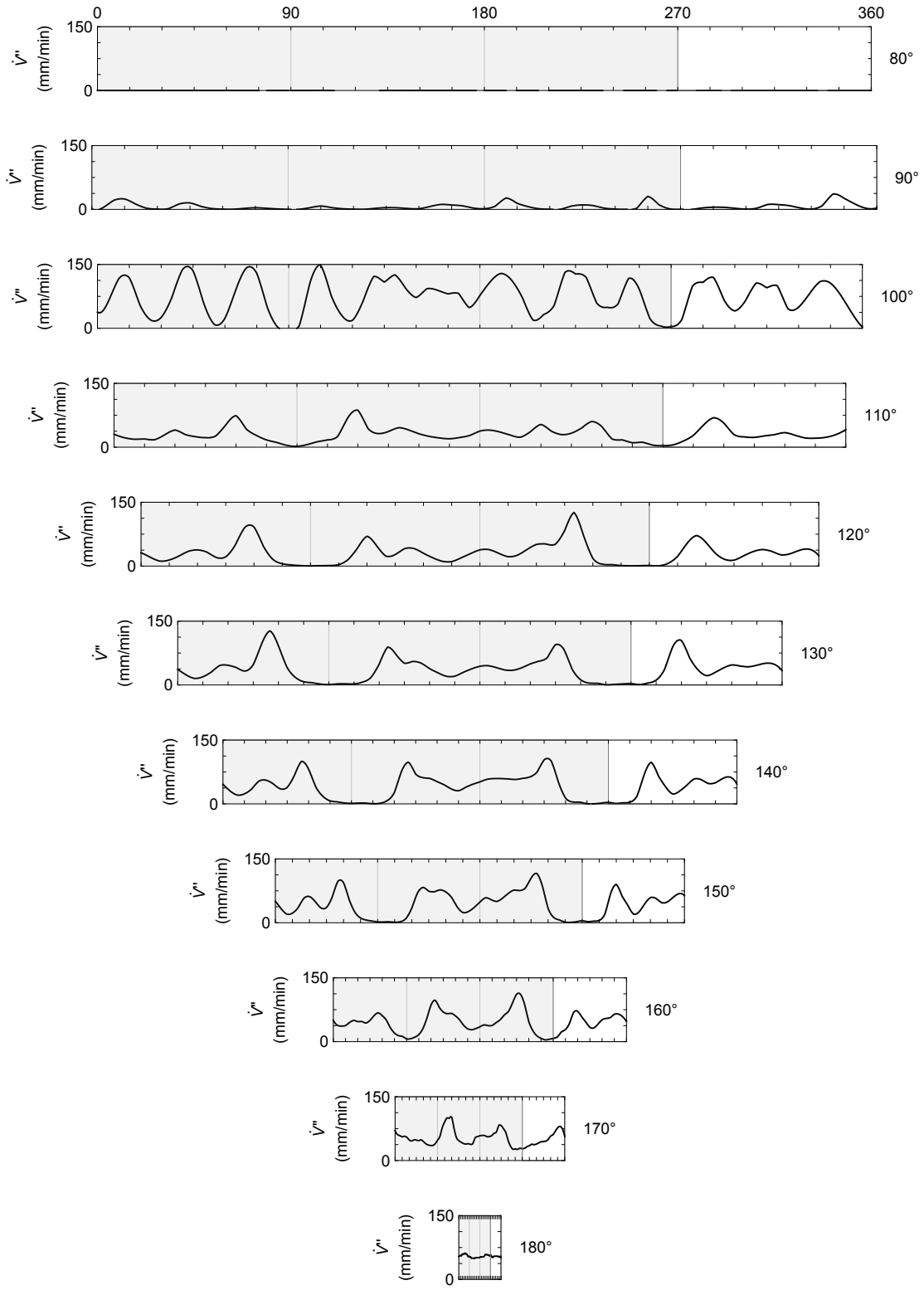

Figure A.6: Volume flux, $\dot{V}''$, measurements for Sprinkler #2 (mm/min).

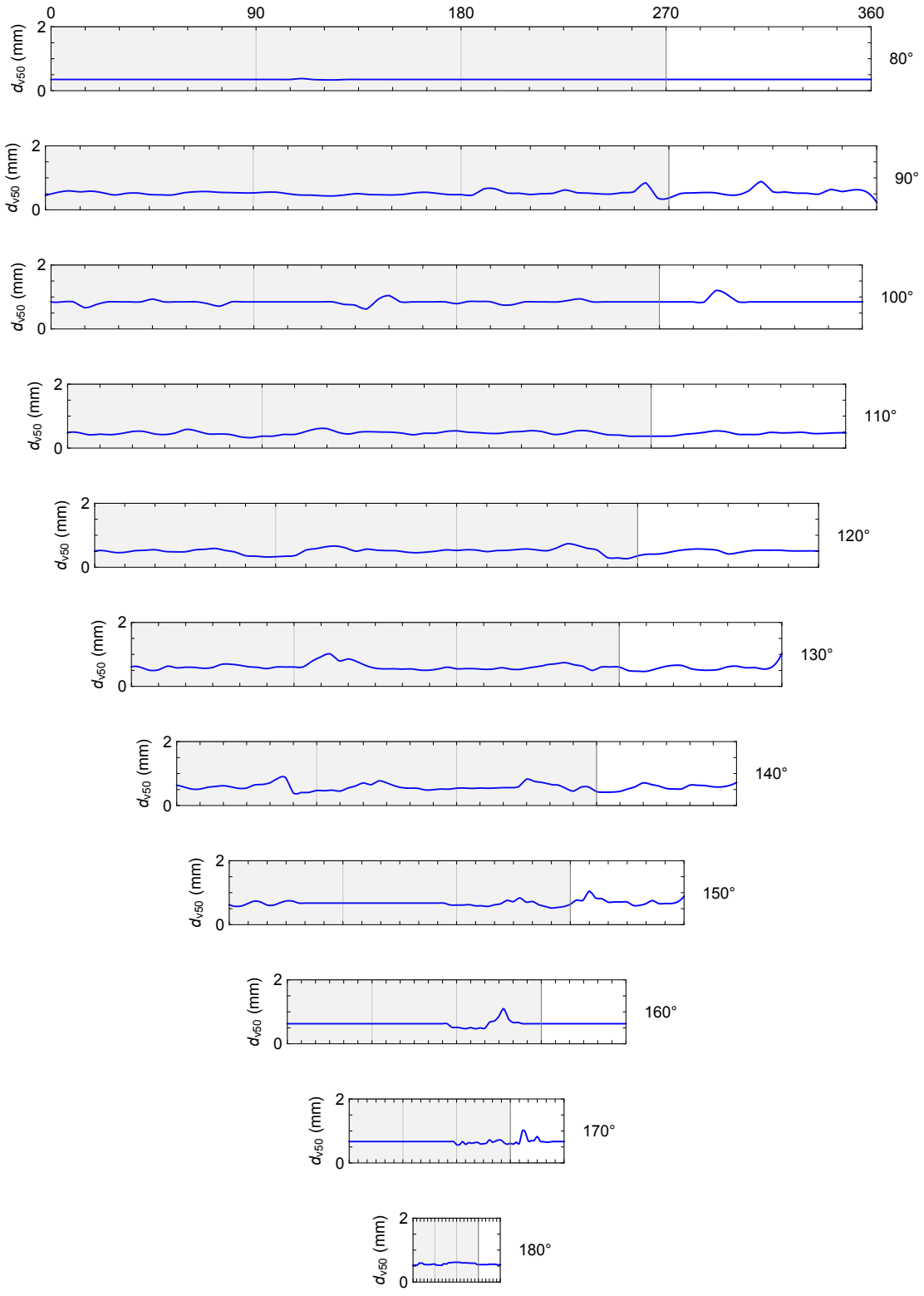

Figure A.7: Drop size, d_{v50}, measurements for Sprinkler #2 (mm).

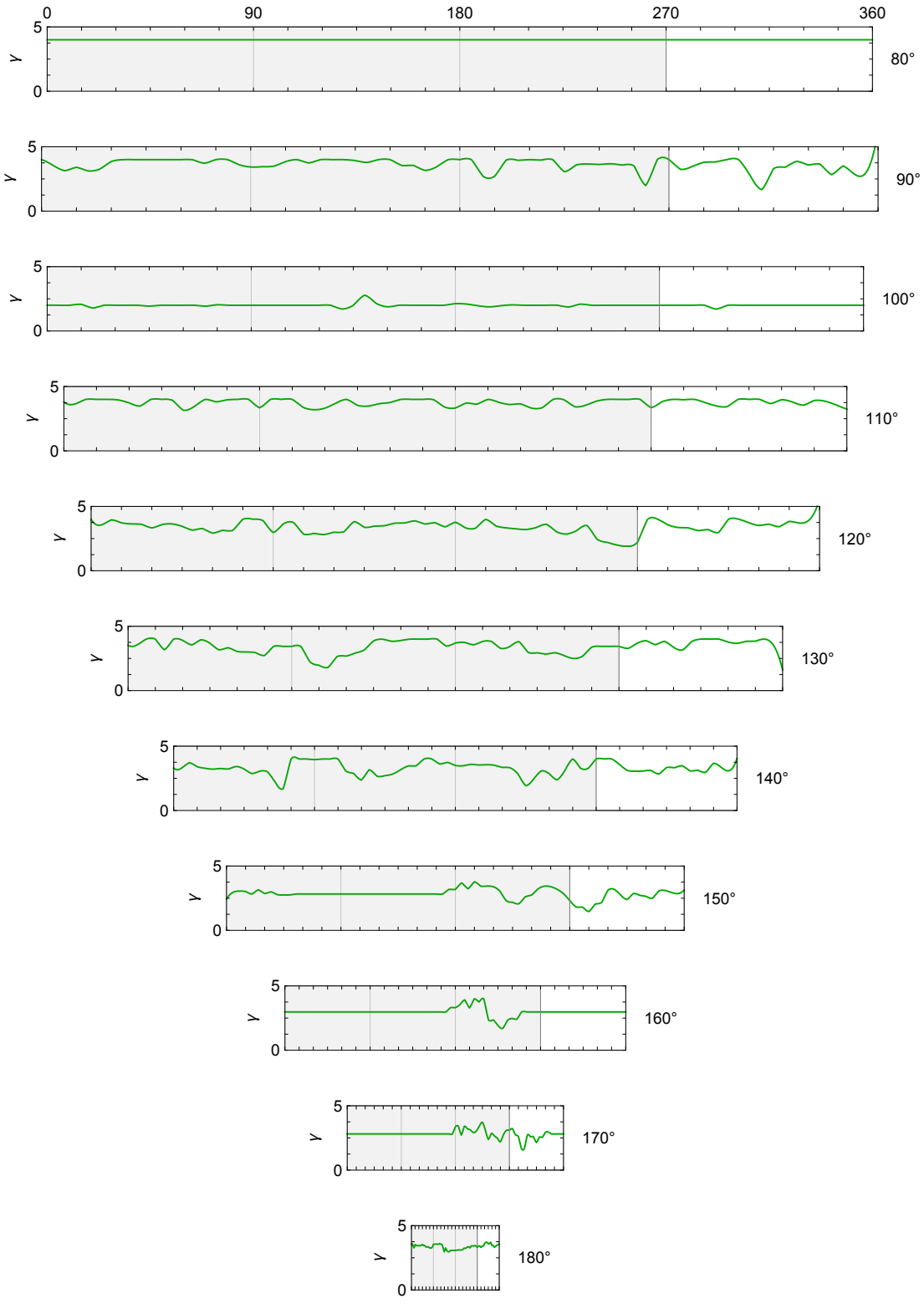

Figure A.8: Drop size distribution width measurements, γ, for Sprinkler #2.

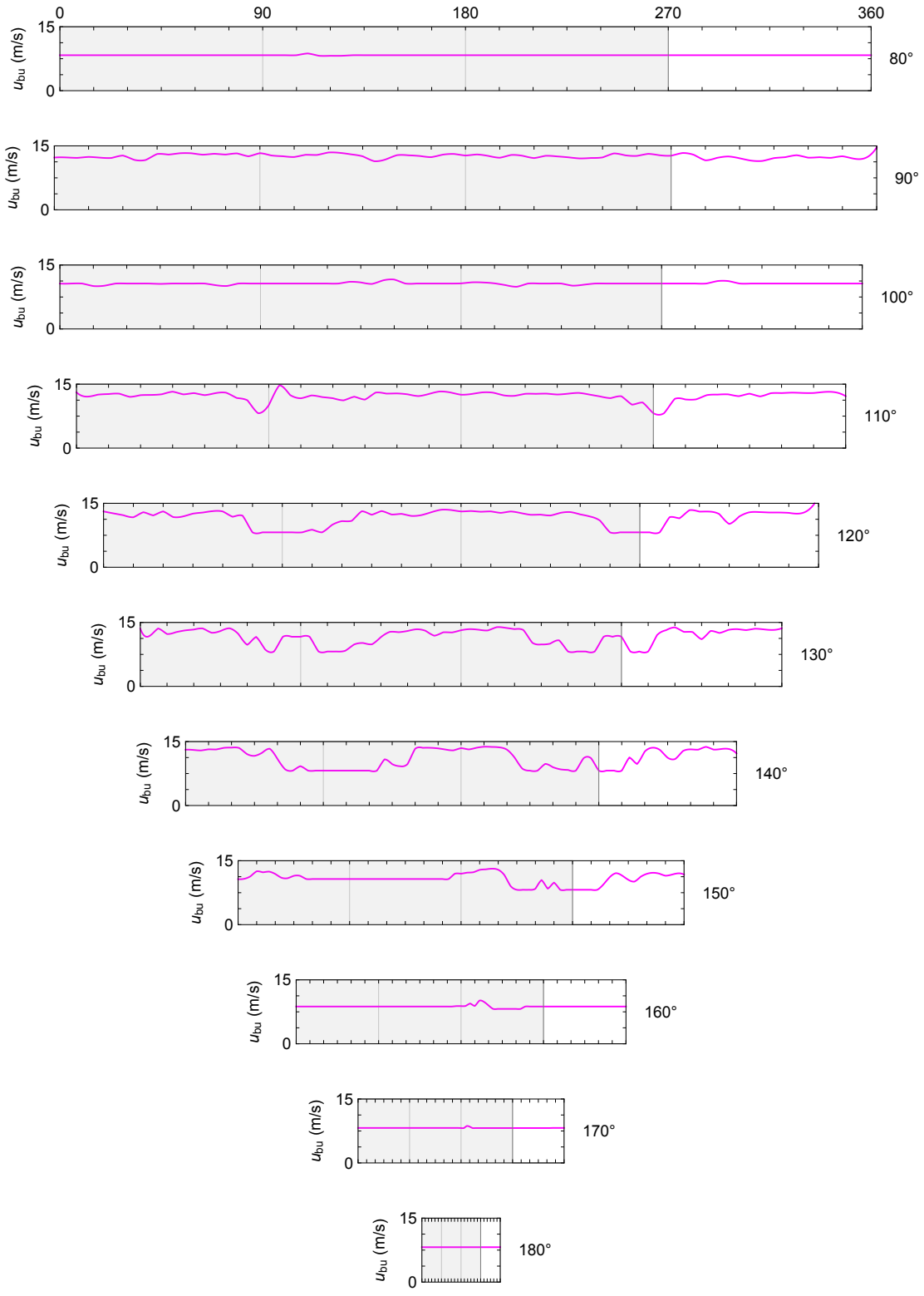

Figure A.9: Initial drop velocity measurements, u_{bu}, at the break-up radius r_{bu} for Sprinkler #2 (m/s).

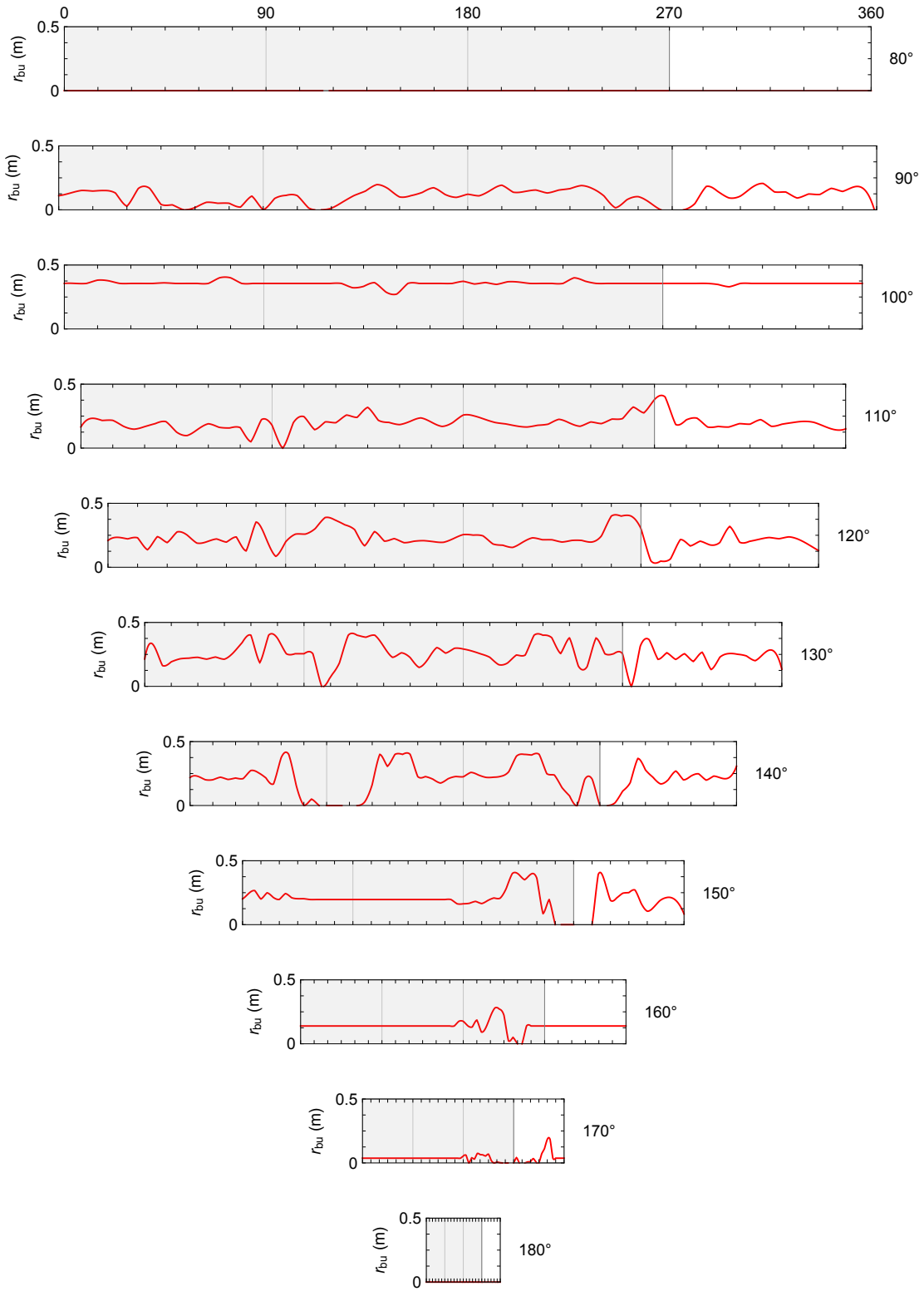

Figure A.10: Break-up radius, r_{bu}, measurements for Sprinkler #2 (m).

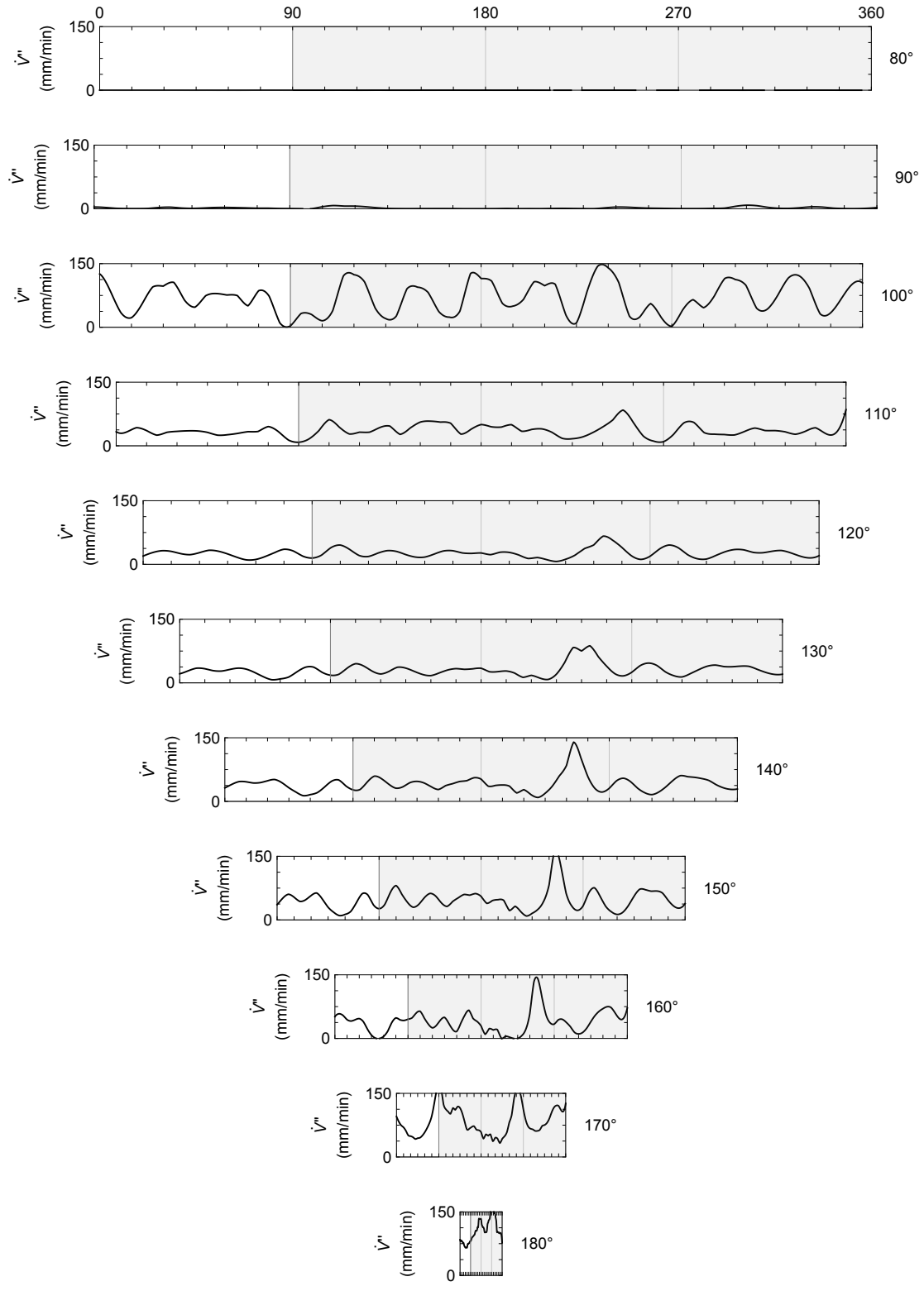

Figure A.11: Volume flux measurements, $\dot{V}''$, for Sprinkler #3 (mm/min).

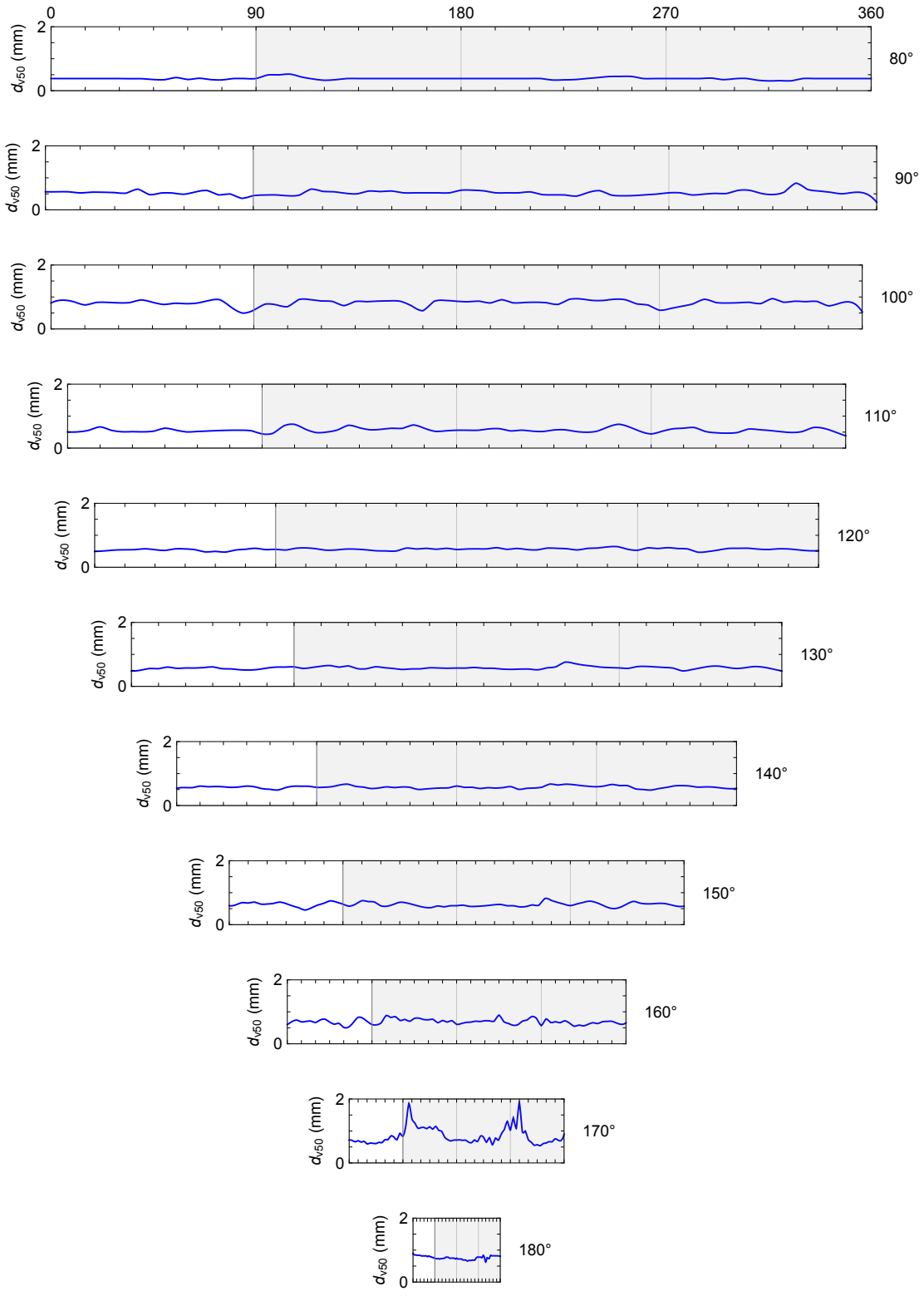

Figure A.12: Drop size, d_{v50}, measurements for Sprinkler #3 (mm).

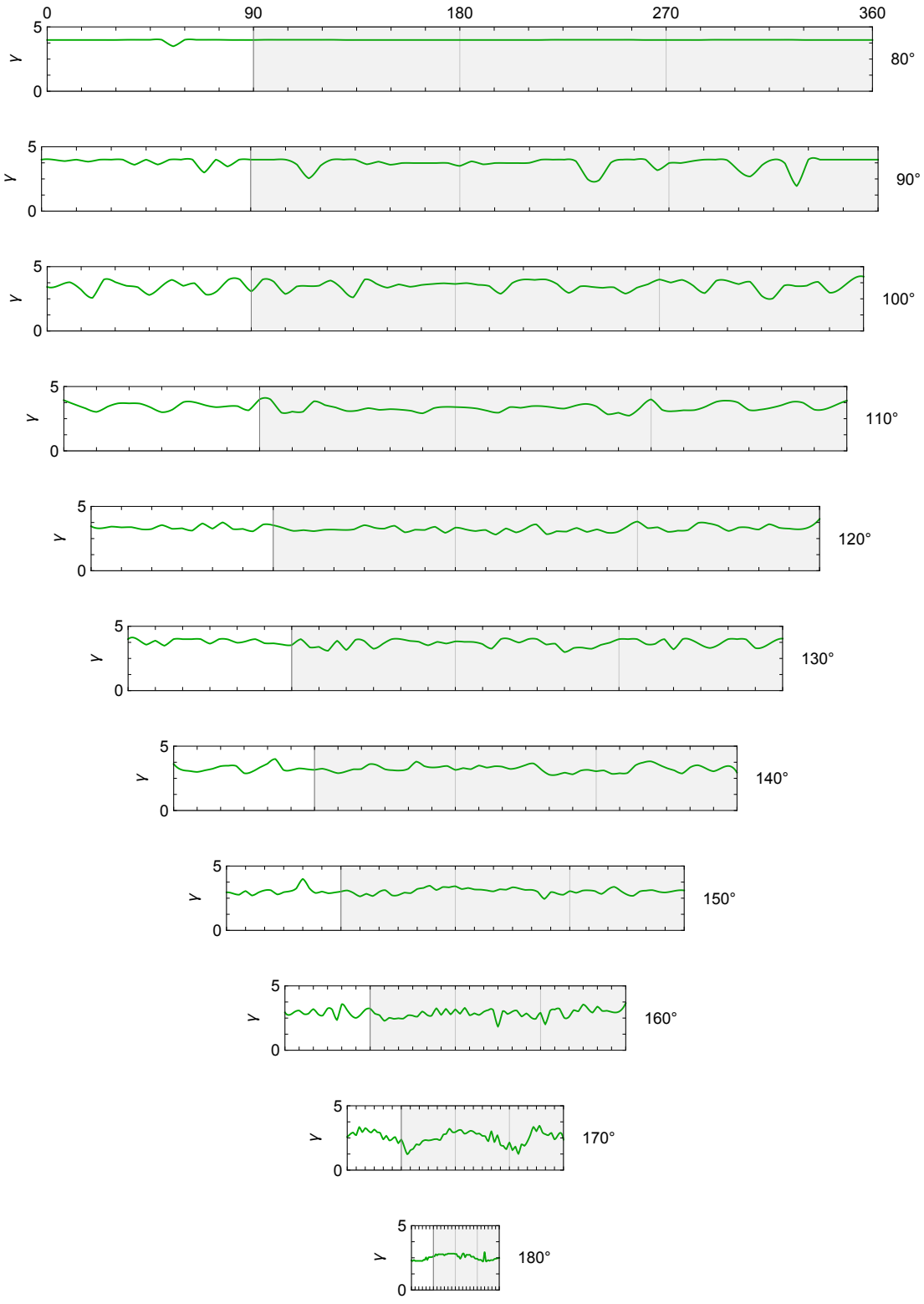

Figure A.13: Drop size distribution width measurements, γ, for Sprinkler #3.

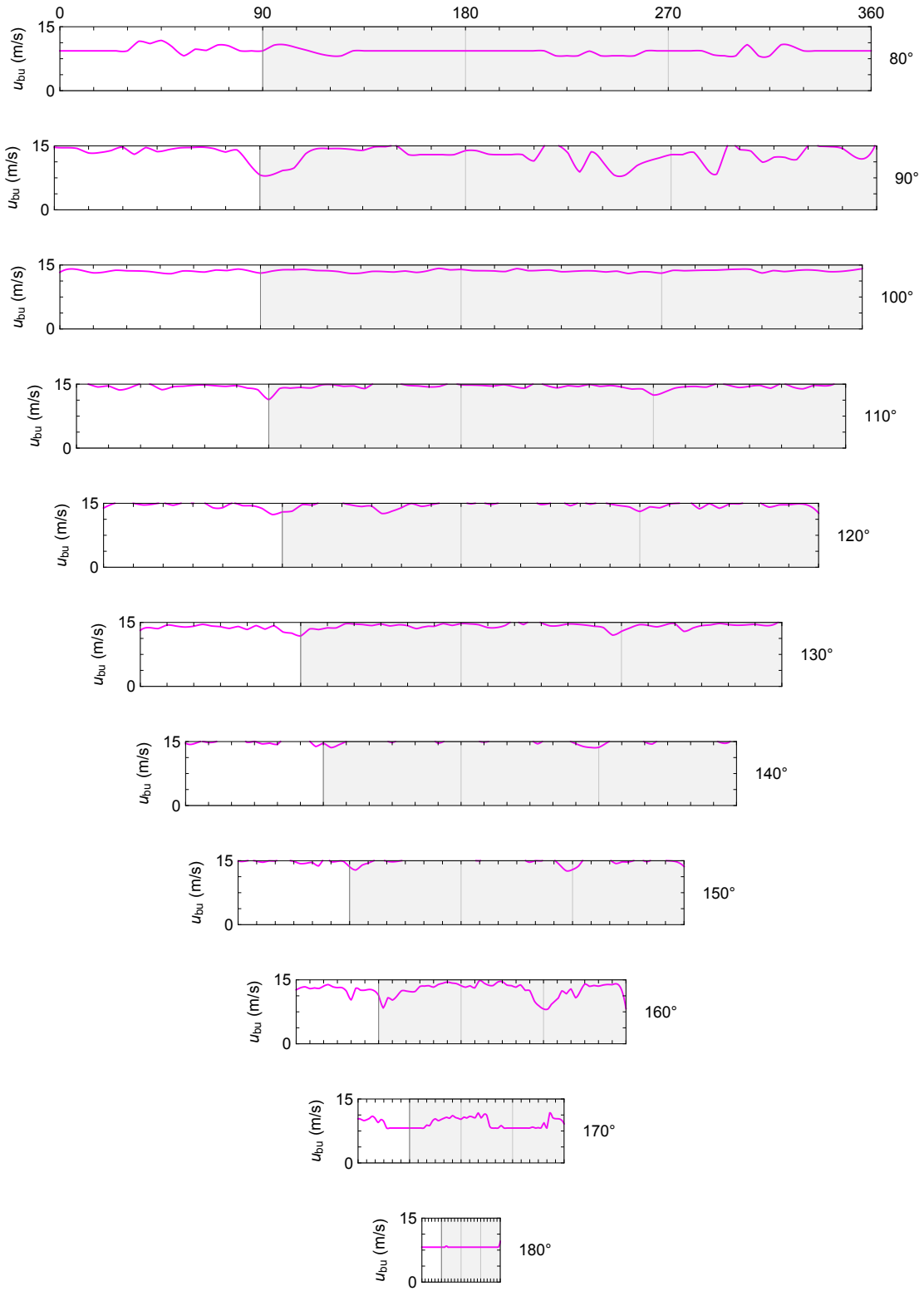

Figure A.14: Initial drop velocity measurements, u_{bu}, at the break-up radius r_{bu} for Sprinkler #3 (m/s).

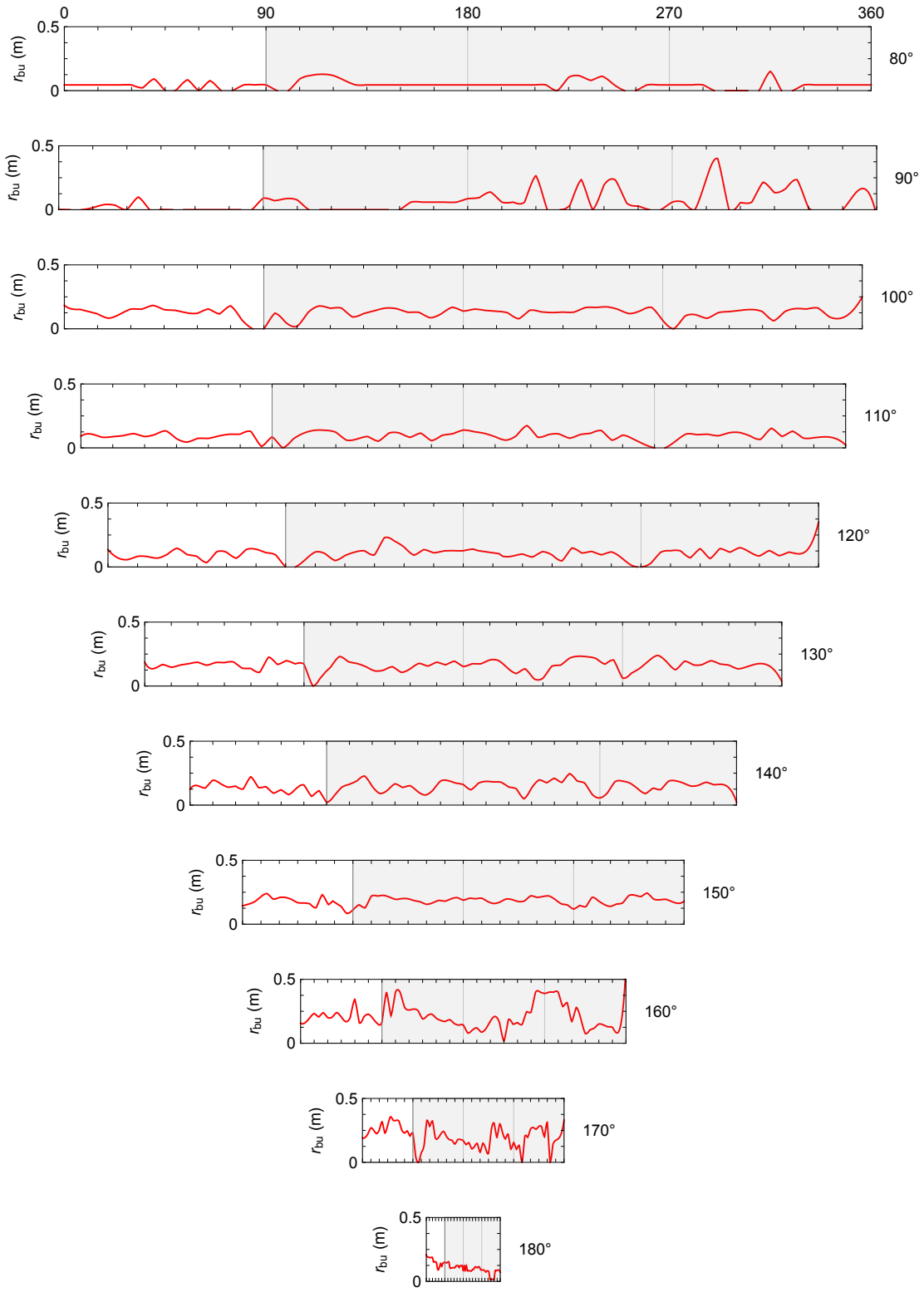

Figure A.15: Break-up radius, r_{bu}, measurements for Sprinkler #3 (m).

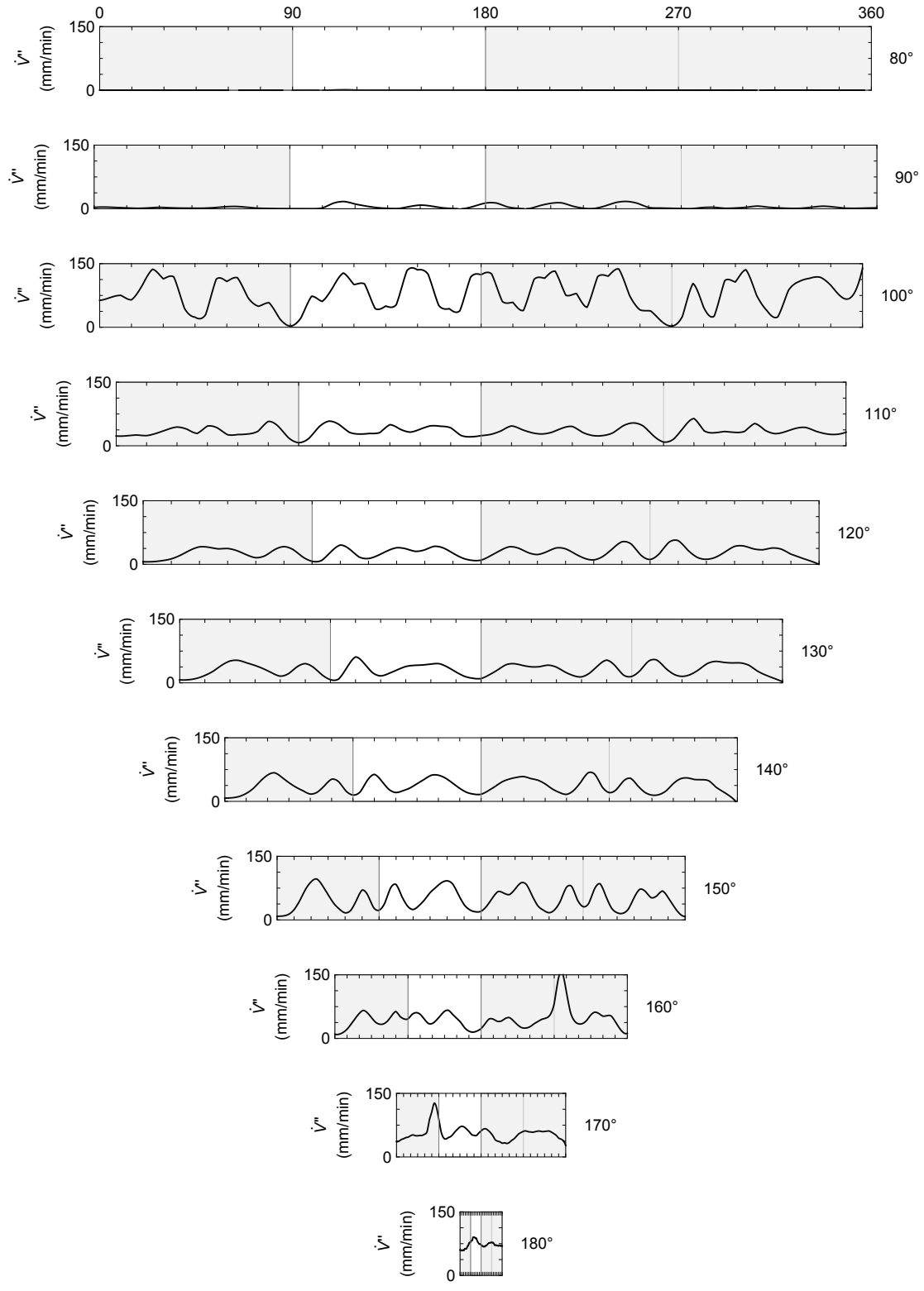

Figure A.16: Volume flux measurements, $\dot{V}''$, for Sprinkler #4 (mm/min).

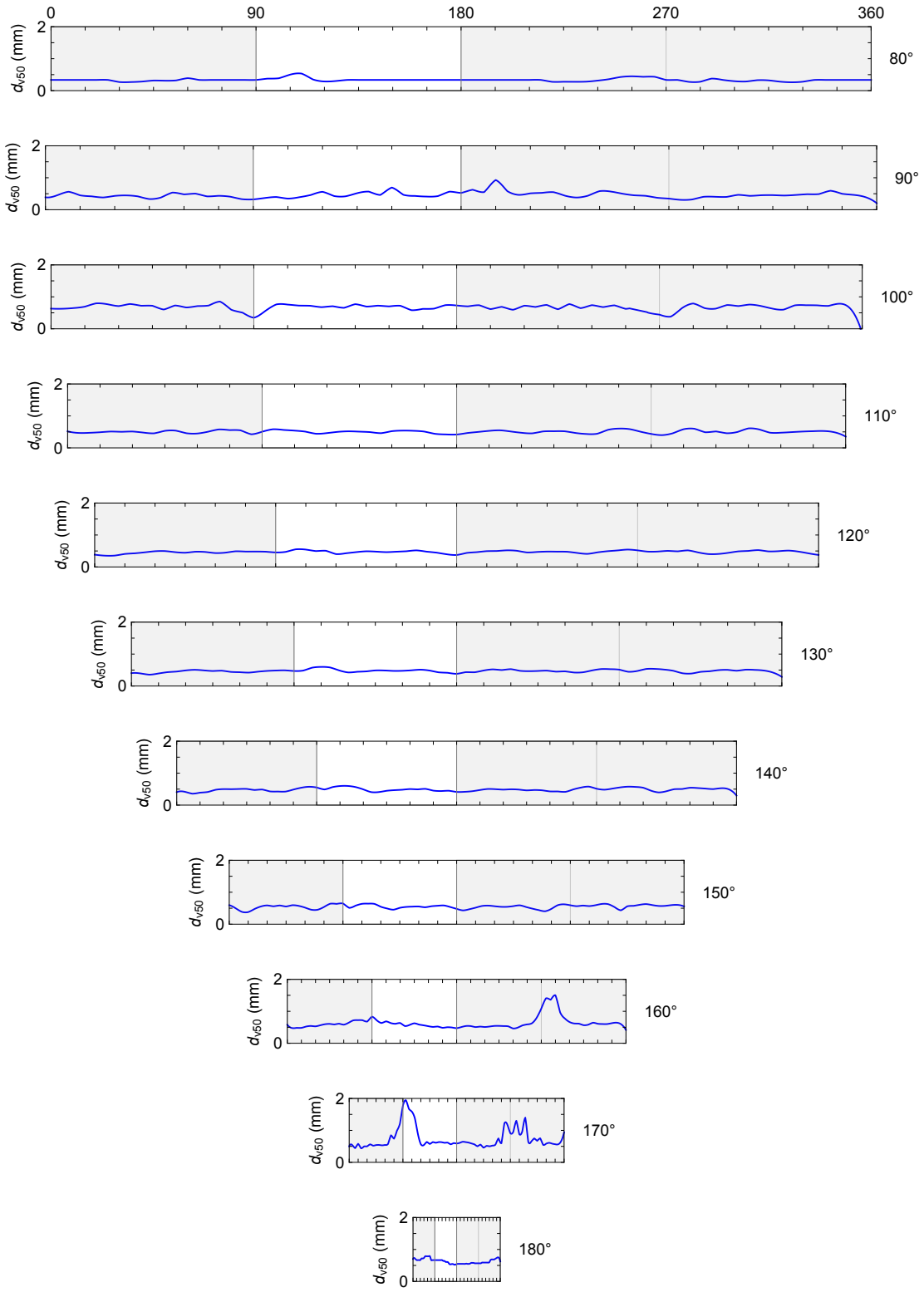

Figure A.17: Drop size, d_{v50}, measurements for Sprinkler #4 (mm).

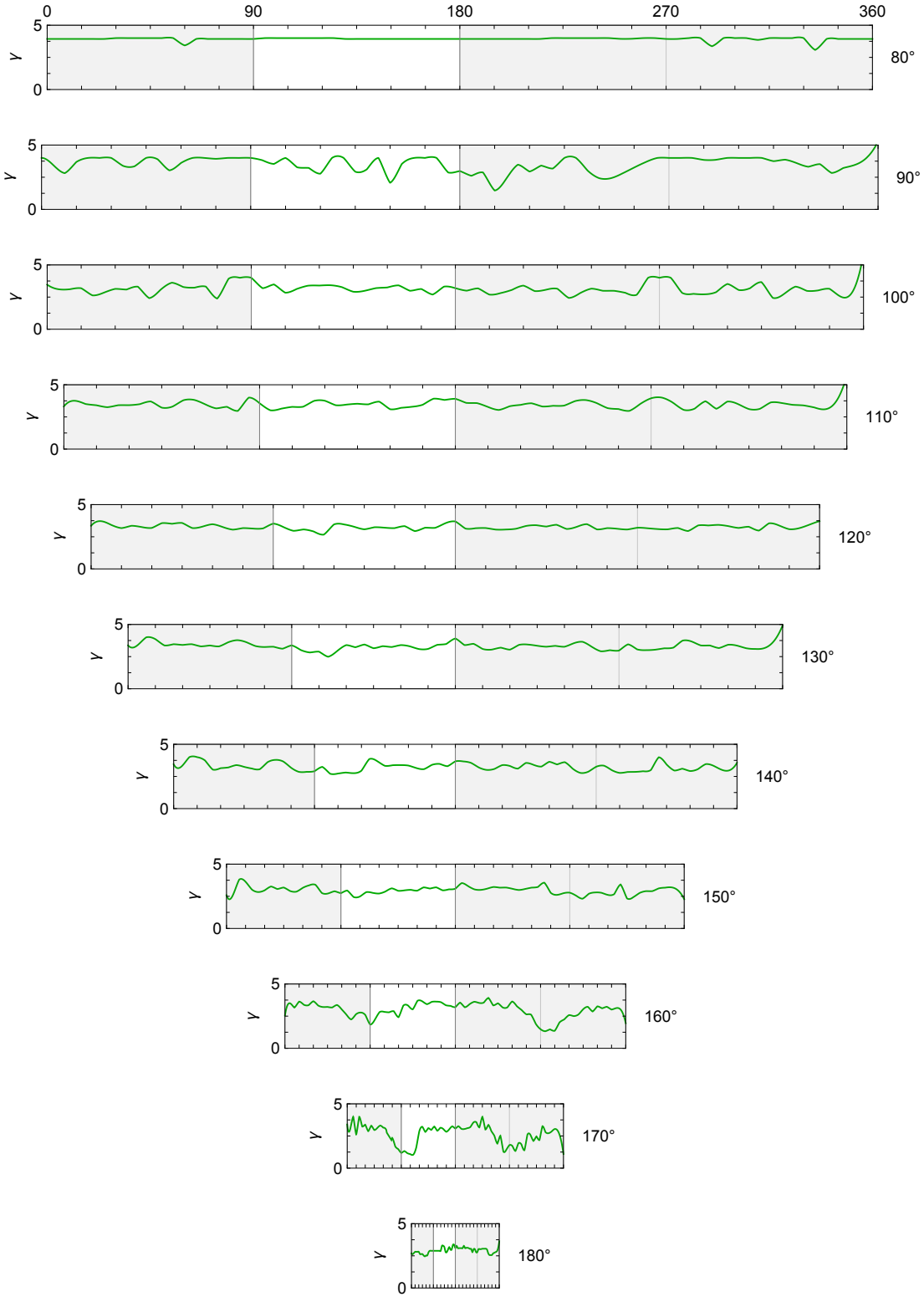

Figure A.18: Drop size distribution width measurements, γ, for Sprinkler #4.

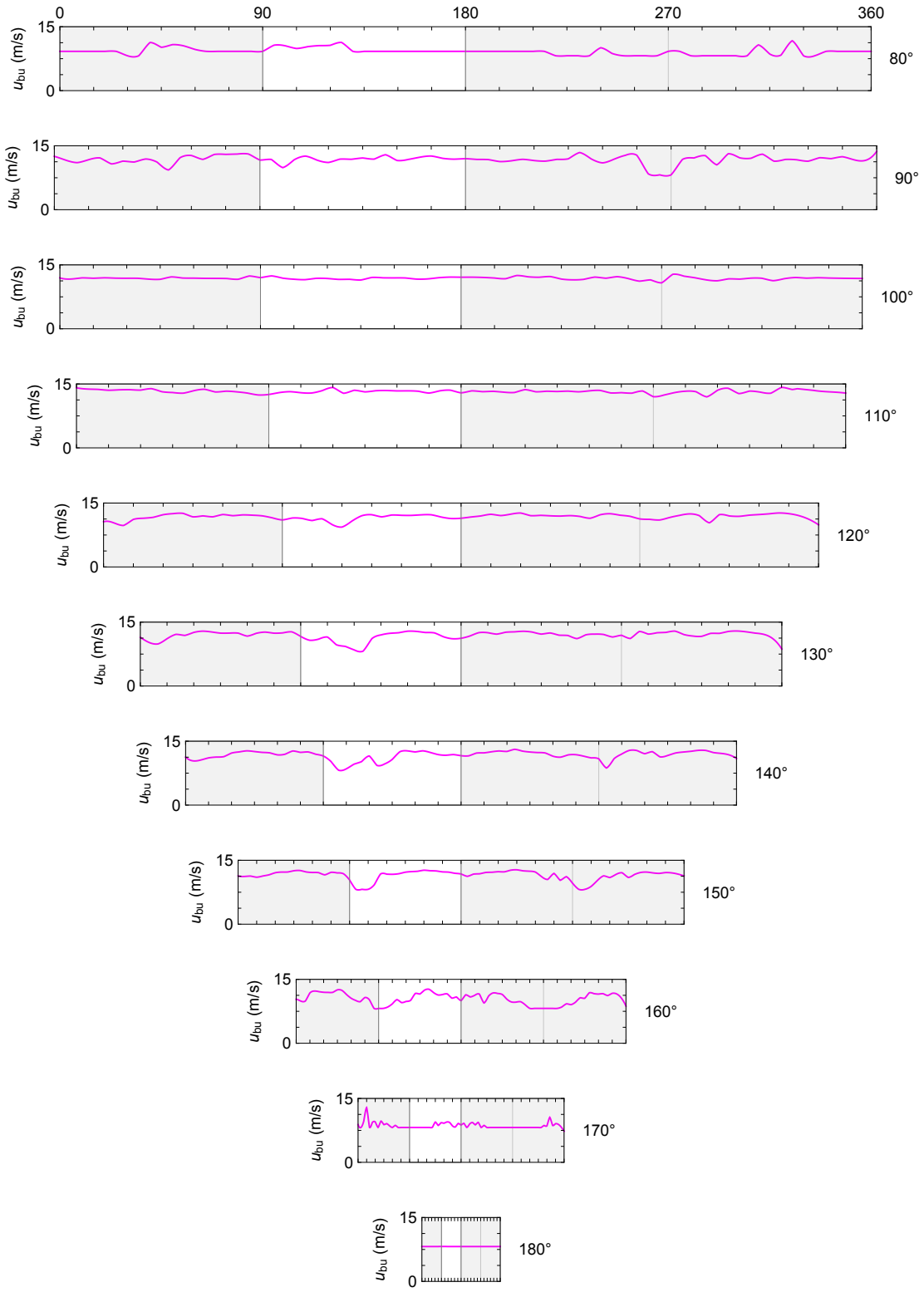

Figure A.19: Initial drop velocity measurements, u_{bu}, at the break-up radius r_{bu} for Sprinkler #4 (m/s).

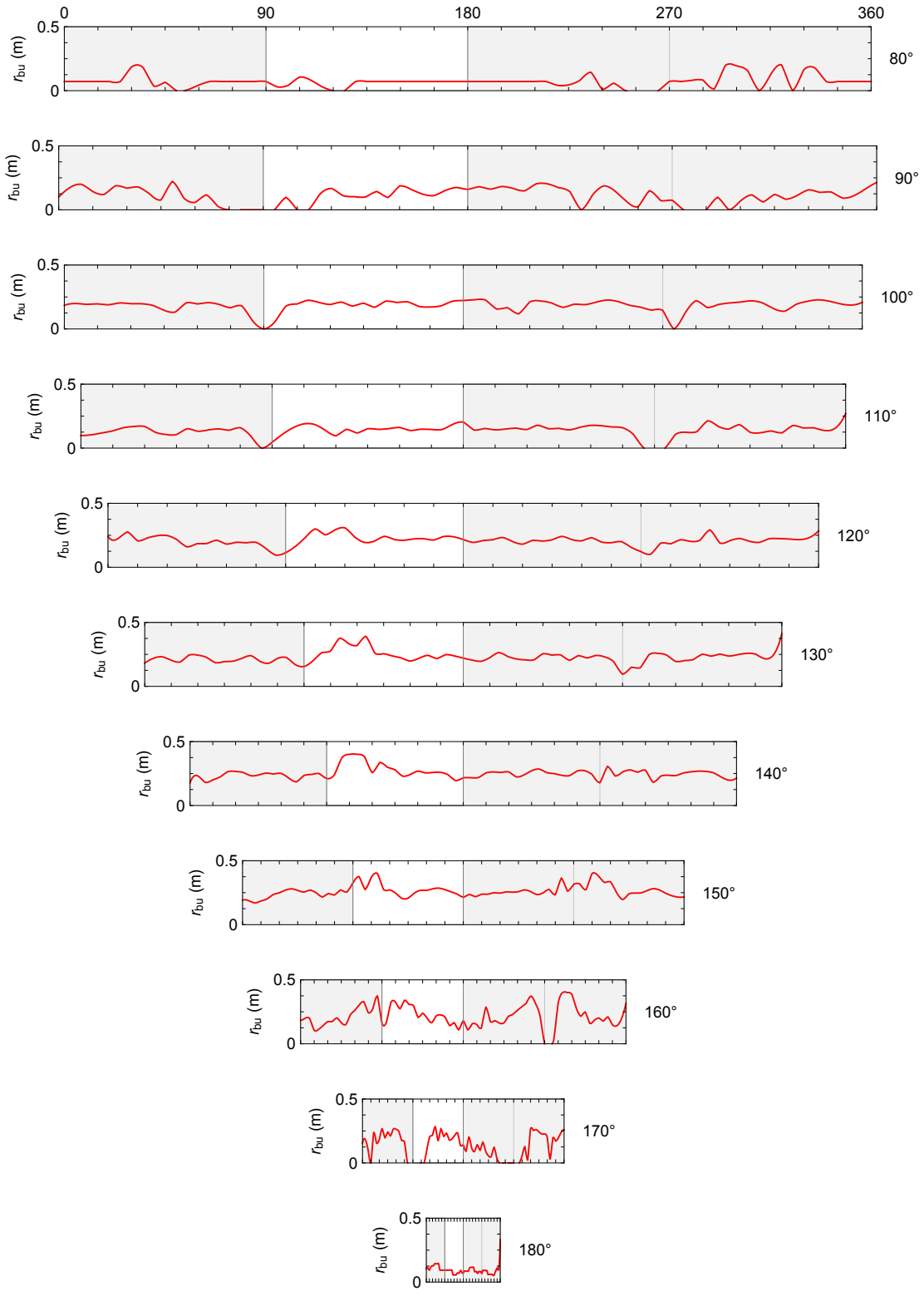

Figure A.20: Break-up radius, r_{bu}, measurements for Sprinkler #4 (m).

Appendix B: SAF Design Details

Additional details about the considerations of drop velocity and spray momentum not provided in Ch. 3 are presented in the following sections of this Appendix chapter.

B.1 Velocity Considerations

Based on the terminal velocity criterion for drop penetration, it was desired that the SAF be able to provide test conditions where the ratio between the drop terminal velocity and the plume velocity were either above or below the critical ratio, $v_{term}/u_{plume} \approx 1$. In consideration of the drop velocity, the range of possible velocities can be estimated to fall between a maximum at injection and a minimum at drop terminal velocity. Drops will interact and penetrate the plume between these velocity extremes, with the terminal velocity being the limiting case. Figure B.1 shows how several important velocity scales correspond to a given sprinkler k-factor. The results of various characteristic velocity calculations were used to guide the final sprinkler k-factor selection.

The injection velocity can be estimated by the Bernoulli velocity as $\sqrt{2\Delta P/\rho_w}$,

where ΔP is the operating pressure and ρ_w is the density of water. The black lines in Fig. B.1 show the limits imposed on the injection velocity due to operating pressure constraints. The minimum pressure is limited by a pressure of 0.5 bar, while the maximum pressure is limited by total flow rate capability, capped at 56 LPM per sprinkler. Note that beyond a k-factor 80 LPM/bar$^{1/2}$, it is not possible to satisfy both constraints.

The terminal velocity is also an important velocity scale, and can be calculated as a function of the drop size. In Fig. B.1, characteristic drop terminal velocities are indicated by the blue shaded region. As drop terminal velocity is dependent on drop size, the characteristic drop size was estimated via correlation prior to the facility design. The volume median drop size, d_{v50}, has been successfully predicted previously using a scaling of the orifice Weber number, $d_{v50}/D_o = CWe_o^{-1/3}$, where the orifice Weber number is defined as $We_o = \rho_w U^2 D_o/\sigma$. Variable ρ_w is water density, U is the injection velocity (governed by operating pressure), D_o is the orifice diameter, and σ is the surface tension of water. The coefficient C is a sprinkler dependent parameter, where a value $C = 3.24$ was previously found to be accurate for the Tyco D3 nozzle at a range of orifice diameters [21]. The upper blue boundary represents the terminal velocity of the d_{v50} at the lowest operating pressure, while the lower bound is determined from the highest allowable pressure determined by flow rate restrictions.

The velocity range of the forced air plume is indicated by the green shaded region, below 4 m/s. For reference, a characteristic velocity of a 300 kW fire is also

shown in Fig. B.1 with a nominal velocity of 6 m/s at the flame height. Experiments aim to be conducted to evaluate the proposed critical condition of drop terminal velocity to plume velocity ratio, $v_{term}/u_{plume} \approx 1$, to evaluate penetration.

The current operating condition is identified by the red point at a k-factor of 33.1 LPM/bar$^{1/2}$ and injection pressure of 1.38 bar, corresponding to an estimated d_{v50} of 0.72 mm and corresponding terminal velocity of 2.9 m/s. Based on an estimated drop size distribution, following the Rosin-Rammler function, the range of velocities from the d_{v10} to d_{v90} drop sizes show the possible range of drop velocities within the spray. The injection velocity is much larger (e.g. 17 m/s at 1.38 bar). The selection of the k-factor 33.1 LPM/bar$^{1/2}$ allowed for smaller drop sizes to be achieved using a lower pressure while still using 75% of the flow rate capability, making it suitable for the lab capabilities and desired test conditions.

The plot shows that with the given range of drop velocities in the current condition, there are plume velocities that the current plume generator can create to sufficiently test this condition.

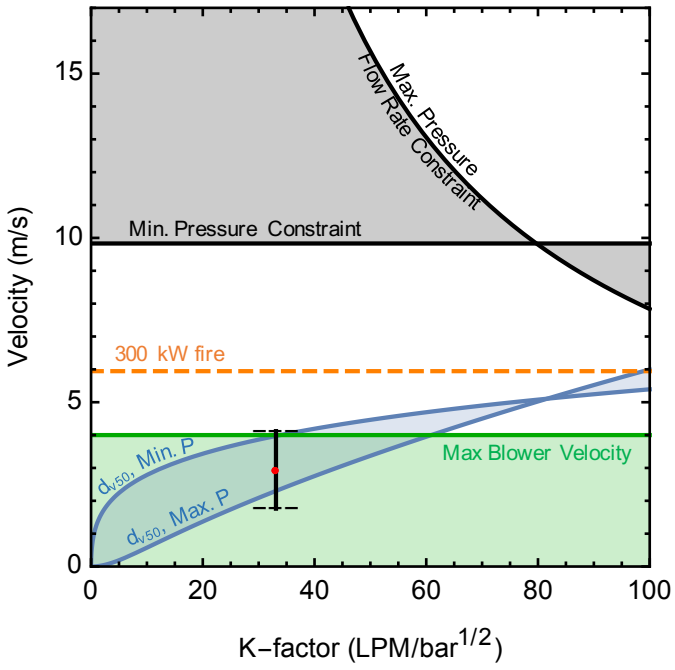

Figure B.1: Plot of relevant spray and plume velocities considered for the design of the sprinkler array facility. The black region indicates possible injection velocities. The blue region indicates the range of possible drop terminal velocities depending on operating pressure. The red point and error bars indicate the operating condition and the range of drop size velocities within the given drop size distribution. The green region indicates the range of plume velocities possible from the current blower. The orange dashed line indicates the estimated plume centerline velocity of a 300 kW fire.

B.2 Momentum Considerations

For the current Tyco D3 nozzle, the spray momentum was estimated through a basic trajectory calculation based on initial spray volume flux measurements from the 4S and an estimated characteristic drop size. The resulting spray distribution is shown in Fig. B.2. Note that the area directly beneath the sprinkler shows the most

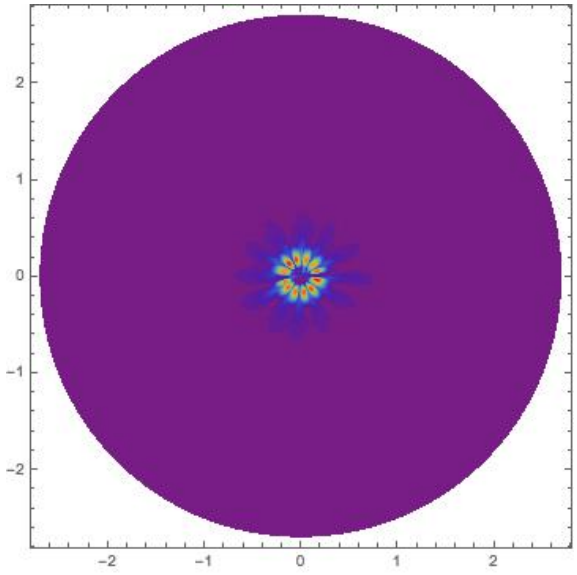

Figure B.2: The spray momentum was estimated using a trajectory calculation to map the volume flux from the sprinkler to the horizontal plane. Using the drop velocity, the momentum is estimated.

significant downward momentum, as expected due to the increased drop velocity and volume flux in this area.

Integration of the locally estimated momentum flux based on the spatially resolved 4S measured volume flux and the drop velocity from a simple trajectory analysis yields a total spray momentum of 4.4 N. This momentum is evaluated based on the area that it is acting over. Several calculations are considered in Table B.1 with different areas of influence are considered. If the entire spray area is considered, this is not necessarily the best characteristic value because of the localized interaction of the plume. Smaller areas were also considered, and an integration was performed to find the highest momentum in these local areas. The table suggests that while the plume velocity of a characteristic fire, at 6 m/s, is a little higher than

the possible jet velocity from the current design, the velocity range of the plume will still permit the momentum of the air jet to be similar to that of the fire plume due to the density difference between the fire and the ambient temperature air jet.

Table B.1: Momentum ratio calculation results for various spray area considerations.

	M_s (N)	A_s (m^2)	M''_s (N/m^2)	u_p m/s	$M''_{p,low}$ (N/m^2)	u_p (m/s)	$M''_{p,high}$ (N/m^2)	u_p (m/s)
Spray core[1]	4.4	5.7	0.77	0.8	0.385	0.56	3.85	1.8
Local spray[2]	0.11	0.126	0.873	0.85	0.437	0.60	4.36	1.9
Local spray[3]	0.05	0.031	1.6	1.15	0.8	0.82	8.0	2.6
300 kW fire estimate	–	–	–	–	10	5	14	6
Current jet	–	–	–	–	–	–	16.4	3.7

[1] total spray momentum, integrated over 1.3 m diameter circle
[2] momentum from high momentum point spot with diameter 0.4 m
[3] momentum from high momentum point spot with diameter 0.2 m

Appendix C: Shadowgraphy Noise Reduction

Raw velocity measurements from the shadowgraphy images yielded very noisy data with clear underlying trends. While the drop size identification worked well from the single processing step, identification of drop pairs between images was poor. Visual inspection of the processing output overlay images (e.g. Fig. 5.4b) identified a significant number of inaccurate particle matches resulting in erroneous velocity vectors. The solution was to divide the image analysis into three steps, each optimized for a specific drop size range. The DaVis software allows the user to specify the minimum and maximum (x, y) dimension of the particle to search for. Particles that do not meet the size criteria on either axis are ignored. Because the drops are not perfectly spherical, drops near the edge of the search range are largely ignored. Therefore, three overlapping ranges were selected for processing, $d < 0.4\,\text{mm}$, $d > 0.4\,\text{mm}$ and an intermediate range $0.25 < d < 0.55\,\text{mm}$. Because the larger drops move at a much larger velocity, a change to the search window size was also implemented to ensure the same drops were identified in both images of the pair. Figure C.1 shows representative results of the noise reduction. The gray data points show original drop velocity measurements from the quiescent close spacing configuration at $z = 0.74\,\text{m}$ on the plume centerline. After implementing

the multiple processing steps for three drop size groups, the scatter was largely removed, shown by the black data points.

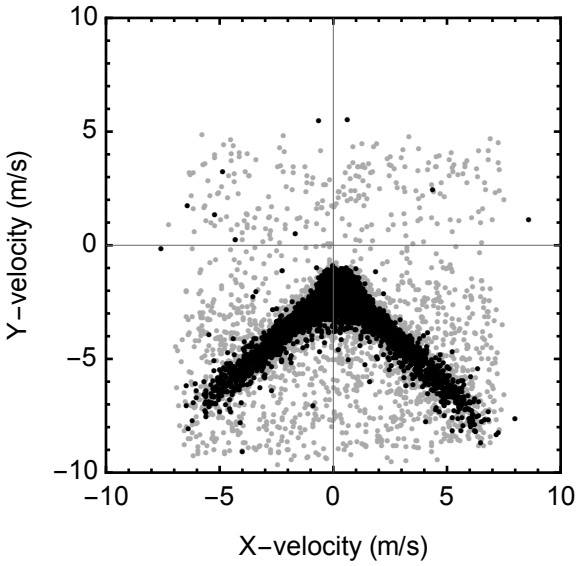

Figure C.1: Measurements of drop velocity with and without the optimized shadowgraphy processing. Black points are the optimized measurements and gray points are with a single processing step.

Appendix D: Spray Work Calculation

Calculation of the spray work through the plume region requires the development of elevation profiles of various spray properties. These include vertical drop velocity, drop size, and drop number density. These profiles are determined based on the shadowgraphy measurements at 5 elevations within the plume, presented in Ch. 5. Because drag force depends on the size of the drop, the spray is divided into discrete drop size groups to account for the different drag force contributions. Ten discrete drop size classes were determined from the local drop size distribution, with each group containing equal volume fractions of the spray. The drop size distribution of the plume centerline is shown in Fig. D.1, where ten equal drop size groups are identified based on the CVF function.

The local volumetric drag force is determined for each drop size class as a function of elevation by

$$F_d'''(z) = n_d(z) \left[\frac{1}{2} C_D(d, v(z)) \, \rho_a \, A_d \, (v_d(z))^2 \right] \tag{D.1}$$

where A_d is determined by the class median volume diameter and $v_d(z)$ is the mean velocity of the drop sizes within the class at the given elevation. The local C_D is also determined as a function of the drop size class and the local drop velocity.

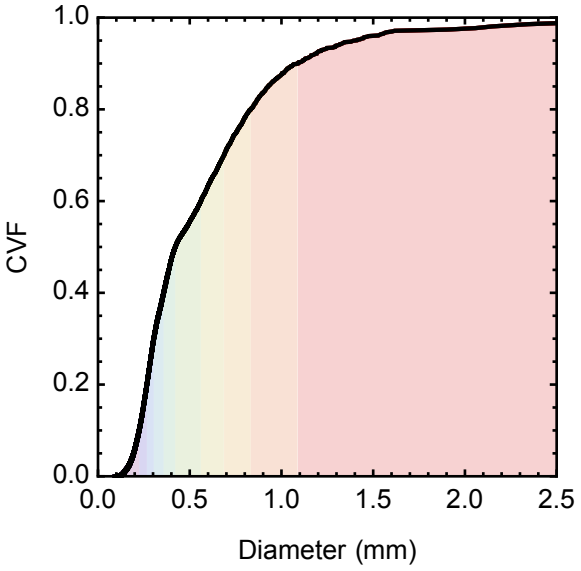

Figure D.1: The cumulative volume fraction drop size distribution for the quiescent close spacing configuration identifies the drop size groups for the spray drag summation.

The drag force is weighted by the local drop number density, determined by $n(z) = \dot{V}_d''(z)/(V_d v(z))$, where $\dot{V}_d''$ is the contribution of the total volume flux by the given drop size class, $\dot{V}_d''(z) = 0.1\dot{V}''(z)$ and V_d is the drop size volume. Figure D.2 shows the elevation profiles of the measured downward velocity, calculated number density (based on measured velocity and volume flux), and the calculated volumetric drag for each of the ten drop size groups.

Summation of the drag force from all drop size classes provides the total local drag force of the spray and is shown in Fig. D.3. This function is integrated over the interaction length scale to determine the value of spray work. In the near spacing case, the length is from $z = 0$ to $z = 0.5$.

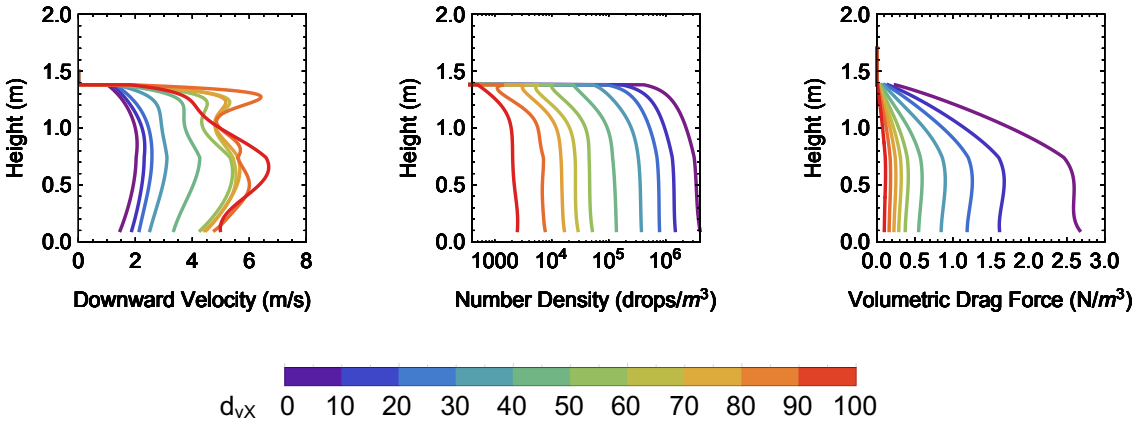

Figure D.2: Resulting elevation profiles from the near spacing spray condition of vertical velocity, drop number density, and volumetric drag force for 10 drop size groups.

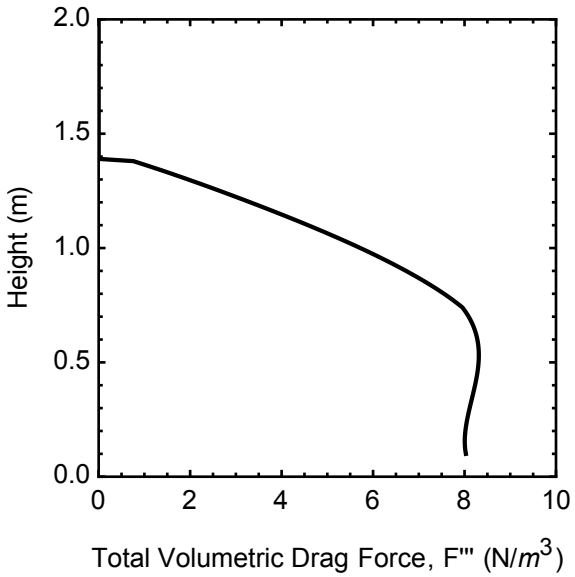

Figure D.3: Summation of the drag forces from each drop size group yields the total drag profile.

Bibliography

[1] D.J. Rasbash. The Extinction of Fire with Plain Water: A Review. *Fire Safety Science–Proceedings of the First International Symposium*, 1:1145–1163, 1986.

[2] G. Grant, J. Brenton, and D. Drysdale. Fire suppression by water sprays. *Progress in Energy and Combustion Science*, 26:79–130, 2000.

[3] NFPA 13: Standard for the Installation of Sprinkler Systems, 2013.

[4] H. J.G. Haynes. Fire Loss in the United States During 2014. Technical report, National Fire Protection Association, 2015.

[5] J.R. Hall Jr. U.S. Experience With Sprinklers. Technical report, National Fire Protection Association, 2013.

[6] C. Yao. Overview of Sprinkler Technology Research. In *Fire Safety Science–Proceedings of the Tenth International Symposium*, pages 93–110, 1997.

[7] *UL 199: Standard for Safety for Automatic Sprinklers for Fire-Protection Service*. Underwriters Laboratories, 2013.

[8] *UL 1626: Standard for Safety for Residential Sprinklers for Fire-Protection Service*. Underwriters Laboratories, 2012.

[9] *Approval Standard for Automatic Control Sprinklers for Fire Protection; Class Number 2000*. FM Approvals, 2006.

[10] C.L. Beyler. Effect of Selected Variables on the Distribution of Water from Automatic Sprinklers. Technical Report GCR-77-105, National Bureau of Standards, 1977.

[11] C. Yao. Applications of Sprinkler Technology–Early Suppression of High-Challenge Fires with Fast-Response Sprinkler. *Fire Safety: Science and Engineering, ASTM STP 882*, pages 354–376, 1985.

[12] C. Yao. Development of the ESFR Sprinkler System. *Fire Safety Journal*, 14:65–73, 1988.

[13] J.M. Prahl and B. Wendt. Discharge Distribution Performance for an Axisymmetric Model of a Fire Sprinkler Head. *Fire Safety Journal*, 14:101–111, 1988.

[14] W.K. Chow and W.M.K Wong. Water Penetration Ratio of A Sprinkler Water Spray. In *First Asia-Oceania Symposium of Fire Science and Technology*, pages 467–474, 1992.

[15] M.D. Dukes and C. Perry. Uniformity testing of variable-rate center pivot irrigation control systems. *Precision Agriculture*, 7:205–218, 2006.

[16] C. Yao and A.S. Kalelkar. Effect of drop size on sprinkler performance. *Fire Technology*, 6:254–268, 1970.

[17] H.-Z. Yu. Investigation of Spray Patterns of Selected Sprinklers with the FMRC Drop Size Measuring System. *Fire Safety Science–Proceedings of the First International Symposium*, 1:1165–1176, 1986.

[18] T.-S. Chan. Measurements of water density and drop size distributions of selected ESFR sprinklers. *Journal of Fire Protection Engineering*, 6:79–87, 1994.

[19] D.T. Sheppard. Spray Characteristics of Fire Sprinklers. Technical Report GCR-02-838, National Institute of Standards and Technology, 2002.

[20] N. Ren, H.R. Baum, and A.W. Marshall. A comprehensive methodology for characterizing sprinkler sprays. *Proceedings of the Combustion Institute*, 33(2):2547–2554, 2011.

[21] A. Marshall. Unraveling Fire Suppression Sprays. *Fire Safety Science–Proceedings of the Tenth International Symposium*, 10:61–75, 2011.

[22] X. Zhou and H.Z. Yu. Spray characterization measurements of a pendent fire sprinkler. *Fire Safety Journal*, 46:140–150, 2011.

[23] X. Zhou, S.P. D'Aniello, and H.Z. Yu. Experimental investigation of spray formation as affected by sprinkler geometry. *Fire Safety Journal*, 54:36–48, 2012.

[24] X. Zhou. Characterization of interactions between plumes and water sprays for sprinkler protection. *Proceedings of the Combustion Institute*, 35:2723–2729, 2015.

[25] S. Jordan, N.L. Ryder, J. Repcik, and A. Marshall. Spatially-Resolved Spray Measurements and their Implications. In *Fire Safety Science–Proceedings of the Twelfth International Symposium*, 2017.

[26] T.M. Myers and A.W. Marshall. A description of the initial fire sprinkler spray. *Fire Safety Journal*, 84:1–7, 2016.

[27] T.-S. Chan, H.-C. Kung, H.-Z. Yu, and W.R. Brown. Experimental Study of Actual Delivered Density for Rack-Storage Fires. *Fire Safety Science–Proceedings of the Fourth International Symposium*, 4:913–924, 1994.

[28] T.-S. Chan and H.-C. Kung. Comparison of Actual Delivered Density and Fire Suppression Effectiveness of Standard and Conventional Sprinklers in Rack-Storage Fires. In *Fire Safety Science–Proceedings of the Seventh International Symposium*, pages 445–456, 2003.

[29] J.A. Schwille and R.M. Lueptow. Effect of a Fire Plume on Suppression Spray Droplet Motion. *Atomization and Sprays*, 16:563–577, 2006.

[30] J.A. Schwille and R.M. Lueptow. The reaction of a fire plume to a droplet spray. *Fire Safety Journal*, 41:390–398, 2006.

[31] J.A. Schwille and R.M. Lueptow. A Simplified Model of the Effect of a Fire Sprinkler Spray on a Buoyant Fire Plume. *Journal of Fire Protection Engineering*, 16:131–153, 2006.

[32] R.L. Alpert. Numerical modeling of the interaction between automatic sprinkler sprays and fire plumes. *Fire Safety Journal*, 9:157–163, 1985.

[33] S. Nam. Development of a computational model simulating the interaction between a fire plume and a sprinkler spray. *Fire Safety Journal*, 26:1–33, 1996.

[34] S. Nam. Numerical simulation of the penetration capability of sprinkler sprays. *Fire Safety Journal*, 32:307–329, 1999.

[35] K.V. Meredith, P. Chatterjee, X. Zhou, Y. Wang, and H.-Z. Yu. Validation of Spray Water Distribution Patterns for the K11.2 Sprinkler in the Presence of a Rack Storage Fire Plume Generator. In *13th International Conference and Exhibition on Fire Science and Engineering*, page 307, 2013.

[36] Y. Wang andK. Meredith andX. Zhou andP. Chatterjee andY. Xin andM. Chaos andN. RenandS. Dorofeev. Numerical Simulation of Sprinkler Suppression of Rack Storage Fires. In *Fire Safety Science–Proceedings of the Eleventh International Symposium*, pages 1170–1183, 2014.

[37] T.M. Myers. A potential flow model of a fire sprinkler head. Master's thesis, University of Maryland, College Park, MD, 2014.

[38] Kevin McGrattan, Simo Hostikka, Randall McDermott, Jason Floyd, Craig Weinschenk, and Kristopher Overholt. Fire Dynamics Simulator Technical Reference Guide Volume 1: Mathematical Model. Technical Report Special Publication 1018, National Institute of Standards and Technology, 2016.

[39] K.V. Meredith, P. Chatterjee, Y. Gopala, S. Sienkiewicz, X. Zhou, H.-Z. Yu, and Y. Wang. A Sprinkler Injection Model for Fire Suppression Simulations. In *Fire Safety Science–Proceedings of the Twelfth International Symposium*, page submitted, 2017.

[40] N. Ren, A.F. Blum, Y.-H. Zheng, C. Do, and A.W. Marshall. Quantifying the Initial Spray from Fire Sprinklers. *Fire Safety Science–Proceedings of the Ninth International Symposium*, 9:503–514, 2008.

[41] P.E. Santangelo, B.C. Jacobs, N. Ren, J.A. Sheffel, M.L. Corn, and A.W. Marshall. Suppression effectiveness of water-mist sprays on accelerated wood-crib fires. *Fire Safety Journal*, 70:98–111, 2014.

[42] G. Heskestad. Fire Plumes, Flame Height, and Air Entrainment. In *SFPE Handbook of Fire Protection Engineering*. NFPA, 3rd edition, 2002.

[43] A.F. Blum. Discharge Characteristics of Canonical Sprinkler Sprays. Master's thesis, University of Maryland, College Park, MD, 2007.

[44] N. Ren. *Advances in characterizing fire sprinkler sprays*. PhD thesis, University of Maryland, College Park, MD, 2010.

[45] E.D. Link, S.J. Jordan, T.M. Myers, P.B. Sunderland, and A.W. Marshall. Spray Dispersion Measurements of a Sprinkler Array. *Proceedings of the Combustion Institute*, 36:3305–3311, 2017.

[46] J.A. Schwille, H.-C. Kung, M. Hjohlman, G.E. Laverick, and G.W. Gardell. Actual Delivered Density Fire Test Apparatus for Sprinklers Protecting High Commodity Storage. In *Fire Safety Science–Proceedings of the Eighth International Symposium*, pages 823–833, 2005.

[47] T. Kékesi, G. Amberg, and L. Prahl Wittberg. Drop deformation and breakup. *International Journal of Multiphase Flow*, 66:1–10, 2014.

[48] BETE Fog Nozzle, Inc. P Nozzle Data Sheet. Online, www.bete.com.

[49] F.P. Incropera, D.P. Dewitt, T.L. Bergman, and A.S. Lavine. *Fundamentals of Heat and Mass Transfer*. John Wiley & Sons, Hoboken, NJ, 6th edition, 2007.